

A satellite is shown in orbit above Earth, with its solar panels and various instruments visible. A bright green laser beam is emitted from a circular array on the satellite, directed towards the illuminated city lights of a coastal region on Earth. The Earth's horizon and atmosphere are visible in the background.

Design and Optimization of a Retroreflector Array for Satellite Laser Ranging

Integration with TU Delft New Satellite and Ground Station

Giacomo Sofi

Design and Optimization of a Retroreflector Array for Satellite Laser Ranging

Integration with TU Delft New Satellite and
Ground Station

by

Giacomo Sofi

to obtain the degree of Master of Science
at Delft University of Technology,
to be defended publicly on 15th of November 2024.

Student number:	5049261	
Project duration:	March, 2024 - November, 2024	
Thesis committee:	Dr. Stefano Speretta	TU Delft, 1 st Supervisor
	Rashika Jain, PhD	TU Delft, 2 nd Supervisor
	Dr. Stéphanie Cazaux	TU Delft, Chair
	I. Uriol Balbin	TU Delft, Examiner

Cover: Generated by OpenAI GPT-4
Style: TU Delft Report Style

An electronic version of this thesis is available at <http://repository.tudelft.nl/>.

Preface

This thesis serves as the final deliverable to obtain the Master of Science degree in Aerospace Engineering with a specialization in Space Engineering at Delft University of Technology. It marks the culmination of five years of study in Delft, beginning with the Bachelor in Aerospace Engineering, complemented by a minor at La Sapienza in Rome, and the Master in Space Engineering, coupled with an internship in Hamburg, Germany.

Looking back on this journey, through highs and lows, including a global pandemic, I leave with not only a wealth of academic and technical knowledge but also amazing memories with friends and family.

I would like to express my deepest gratitude to everyone I encountered during my time in Delft. Whether you were there from the beginning or joined along the way, you have all left a lasting impression on me. Special thanks go to my close friends, Silvio and Antonio, with whom I shared a home for two years, Giorgio and Marco for all the moments we spent together, and Sergio, whose friendship began in English and now continues in Italian, strengthened by our trips around southern Italy. I am also grateful to Alfonso, who has been a friend since high school and, despite ending up in Enschede, reconnected with me in Delft during these last two years.

To the "Rinascita di Delft," whom I met later in the journey: your presence became a strong and positive influence, giving me the strength to push through difficult study moments and creating unforgettable memories. A heartfelt thank you to "Sapori di Casa" for making me feel at home every day at the fellowship.

Lastly, I would like to thank my supervisors, Stefano Speretta and Rashika Jain, for their invaluable feedback and guidance throughout the thesis process. Thank you for your time, support, and for giving me this opportunity.

*Giacomo Sofì
Delft, October 2024*

Summary

Satellite Laser Ranging (SLR) is a technique used to determine the distance of an object or satellite in orbit from ground stations. This technique involves emitting short laser pulses from a ground-based station towards an object in orbit or a satellite equipped with retroreflectors, which reflect the incident light back towards its source with minimal deviation, regardless of the angle of incidence. By measuring the time interval between the emission and reception of the laser pulse, the SLR system can determine the distance between the ground station and the satellite. Multiple measurements can be taken per orbital pass, allowing for the reconstruction of the satellite attitude. SLR achieves millimeter-level accuracy in distance measurements and typically uses a passive space system, making it an ideal candidate for attitude determination backup, as well as a calibration tool for Global Navigation Satellite System (GNSS) receivers.

Delfi-PQ, a satellite launched by TU Delft in 2022, was equipped with four retroreflectors intended for SLR measurements to validate GNSS data and serve as a demonstration. However, ground stations were unable to retrieve SLR data from Delfi-PQ due to suboptimal retroreflector selection and array design. Despite this, TU Delft is currently developing two new platforms: Delfi-Twin, the successor of Delfi-PQ, and the Da Vinci satellite, which will participate in the European Space Agency (ESA) program "Fly Your Satellite." Both platforms require the implementation of SLR capabilities, leading to the following need:

With the development of TU Delft new platforms, there is a need for an optimized design of the retroreflector array to successfully perform SLR measurements.

This thesis aims to document the research conducted to address the need for designing an effective and optimized retroreflector array for TU Delft new platforms, while also considering the potential ground stations that could be used for the measurements. TU Delft is currently constructing a laser communication terminal on top of the Aerospace Faculty building, with plans to use it for these measurements. Nevertheless, the International Laser Ranging Service (ILRS) remains the state-of-the-art network for SLR measurements. Based on this need, the following research objectives and related questions were formulated:

- **RO-1:** Design a retroreflector array to be mounted on the new TU Delft platforms to obtain Time of Flight (ToF) measurements utilizing a laser ranging terminal from the ILRS network.
 - **RQ-1:** Is it technically feasible to obtain SLR measurements using a retroreflector array mounted on the new TU Delft platforms and a laser ranging terminal from the ILRS network?
- **RO-2:** Design a retroreflector array to be mounted on the new TU Delft platforms to obtain ToF measurements utilizing the laser communication terminal at Delft University.
 - **RQ-2:** Is it technically feasible to obtain SLR measurements using a retroreflector array mounted on the new TU Delft platforms and the laser communication terminal at Delft university?

To address the research questions outlined, a structured approach was taken. First, a literature review was conducted to gain insights into the state-of-the-art of SLR systems and to gather knowledge for retroreflector array design. Based on the literature, three main building blocks were defined:

- **Block One:** This block involves a Probability of Visibility (PoV) simulation, which provides the PoV of the implemented array configuration per elevation angle during a pass within the Field of View (FoV) of the ground station. Different satellite attitudes and array configurations can be tested. The goal of this simulation is to identify the most suitable array configuration for the satellite intended attitude, including the optimal number and placement of retroreflectors.

- **Block Two:** This block comprises a link budget analysis, which calculates the mean number of returning photons received by the ground station detector based on the Optical Cross Section of the implemented retroreflectors. The goal of this block is to define the required size of the retroreflectors in the array to enable successful SLR measurements with the selected ground stations.
- **Block Three:** This block covers the preliminary inspection and integration of the selected array configuration. The retroreflectors must undergo inspection and testing to be deemed ready for flight. Additionally, the array configuration must be integrated onto the satellite to confirm it meets the satellite physical constraints and adheres to the protrusion limits imposed by the launch case.

Five configurations and three attitudes were tested during the PoV simulation. The configurations were developed based on the limit of a maximum of 8 retroreflectors in the array. The tested configurations included the following: one retroreflector placed on the bottom face of the satellite (1 Face); three retroreflectors positioned on the bottom face, similar to the Astrocstp1 satellite (Astrocast); four retroreflectors placed around the rolling axis, with one on each lateral face (4 Faces); eight retroreflectors around the rolling axis, with two on each lateral face oriented at a 15° angle from the centerline of the face (8 Faces); and eight retroreflectors similarly placed but alternately shifted by $\pm 15^\circ$ around the pitching axis (8 Faces Alt). The tested attitudes were as follows: a fixed attitude with the bottom face constantly pointing nadir, as expected for the Da Vinci satellite, a fixed attitude in the pitching and yawing axes with a rolling rate between 5 deg/s and 10 deg/s, and an attitude with a rolling rate between 5 deg/s and 10 deg/s along with $\pm 20^\circ$ oscillations in the pitching and yawing axes at a 5 deg/s rate, as expected for Delfi-Twin.

For each attitude, the best array configuration was selected based on the highest achievable coverage across all elevation angles. For attitude 1, where the satellite bottom face consistently points nadir, the Astrocast configuration was selected as the most suitable, providing an average PoV of 84.97% across all elevation angles and achieving 100% coverage at angles greater than 35° . As this attitude represents the Da Vinci satellite, the research recommends implementing the Astrocast configuration to aid in the calibration of its GNSS receiver. For attitude 2, where the satellite rolls at a rate between 5 deg/s and 10 deg/s, the 8 faces alt configuration provided the most coverage, with an average PoV of 84.69%, achieving 100% coverage at elevation angles higher than 68° . Lastly, for attitude 3, which involves rolling at a rate between 5 deg/s and 10 deg/s with pitching and yawing oscillations of $\pm 20^\circ$ at a 5 deg/s rate, the 8 faces configuration was deemed the most suitable, offering an average PoV of 81.55% and achieving 100% coverage at elevation angles greater than 65° . Since this attitude corresponds to Delfi-Twin, this research recommends the implementation of the 8 faces configuration to successfully achieve SLR measurements for this platform.

The link budget analysis was conducted for the four selected ground stations: Delft laser communication station, Mini-SLR, Potsdam, and Matera. However, the link budget could not be closed for the Delft laser communication station or the Mini-SLR station, making SLR measurements unfeasible with these stations and the new TU Delft platforms. Nevertheless, a retroreflector radius of 12.7 mm was selected for the array, as it provided convergence for both the Matera and Potsdam stations and falls within the available sizes of fused silica Cube Corner Retroreflector (CCR) offered by Edmund Optics. For the Matera station, the link budget is closed from an elevation angle of 20° onwards, considering Angles of Incidence (AOI) on the array between 0° and 42° during both daytime and nighttime, fully utilizing the coverage of the selected configurations. For the Potsdam station, however, the selected retroreflector radius only closes the link budget at nighttime, from an elevation angle of 40° onwards, with an AOI range between 10° and 40° . This limits the array configuration coverage to an average PoV of 76% for Delfi-Twin, which is still deemed acceptable for SLR measurements.

During the development of the thesis, 30 retroreflectors of the selected diameter were acquired by the Department of Space Engineering (DSE) from Edmund Optics. This acquisition enabled an inspection, which was conducted in the clean room facility at the Aerospace Faculty. Four out of the 30 retroreflectors, specifically RT-08, RT-18, RT-21, and RT-25, were cataloged as damaged. To finalize the assessment and determine if the retroreflectors that passed the inspection are suitable for integration into the satellite arrays, additional tests on their optical performance must be conducted. These tests will evaluate the reflectivity and AOI leakage of the retroreflectors. If these parameters fall within the constraints assumed in this research, the retroreflector arrays can be integrated into the new

platforms. Furthermore, a preliminary design of the retroreflector array holder for Delfi-Twin was developed, incorporating four bolometers from Melexis into the array. This led to the creation of a new array configuration that differs from the original 8 faces configuration, with the angle of the retroreflectors relative to nadir increased to 30° . This change did not significantly affect the performance of the array. The retroreflector holder design confirmed that the array fits within Delfi-Twin physical constraints as imposed by the launch case. A render of the array integrated onto the satellite is shown in Figure 1.

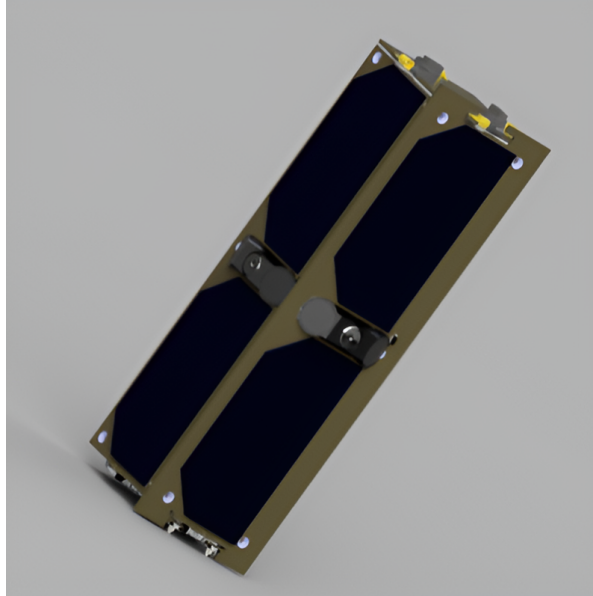


Figure 1: Render of the retroreflector array integrated on Delfi-Twin.

With the collected results, the research objective of designing an effective and optimized retroreflector array for the new TU Delft platforms was successfully achieved. Furthermore, the research questions were addressed, concluding that SLR is unfeasible between the Delft laser communication station and the new TU Delft platforms.

Several recommendations for future work have been identified. Firstly, for the Da Vinci satellite, the retroreflector array was selected from configurations initially designed for Delfi-Twin. This opens the possibility of rerunning the PoV simulation, placing retroreflectors on the front and back faces of the satellite to further enhance coverage. Secondly, the planned tests on the acquired retroreflectors must be completed to ensure they meet the necessary qualifications for integration into the satellite. In terms of simulation, the interference between multiple retroreflectors within the array was not considered in this study. As a result, conducting a Far-Field Diffraction Pattern (FFDP) characterization of the array to be integrated on the satellite would be valuable for understanding potential interactions and optimizing performance. Lastly, acquiring a more powerful laser could enable the Delft laser communication station to support SLR measurements independently, eliminating the need to rely on the ILRS network for satellite ranging operations.

Contents

Preface	i
Summary	ii
List of Figures	ix
List of Tables	xi
Nomenclature	xii
1 Introduction	1
2 Literature Review	3
2.1 Satellite Laser Ranging	3
2.1.1 History of Satellite Laser Ranging	3
2.1.2 Radio vs Laser	4
2.1.3 Type of Applications	5
2.1.4 Basic Principles	5
2.1.5 SLR System	6
2.2 Range Model	7
2.2.1 Range Data Point	7
2.2.2 Correction Factors	8
2.2.3 Normal Point Algorithm	13
2.2.4 Precision of Normal Points	14
2.3 Retroreflectors Design	15
2.3.1 The Link Budget Equation	15
2.3.2 Required Mean Number of Returning Photo-electrons	17
2.3.3 Optical Cross Section	20
2.3.4 Velocity Aberration	21
2.3.5 Retroreflector Types	22
2.3.6 Radiation Effect	23
2.4 Ground Station	25
2.5 TU Delft Satellite Platforms	26
3 Methodology	28
3.1 Requirements	28
3.2 Approach	30
3.2.1 Probability of Visibility Simulation	30
3.2.2 Link Budget Analysis	32
3.2.3 Retroreflector Testing & Integration	34
4 Probability of Visibility	35
4.1 Scenarios	35
4.1.1 Array configuration	35
4.1.2 Satellite Attitude	37
4.2 Validation	37
4.3 Results	39
5 Link Budget Analysis	42
5.1 Ground Station Comparison	42
5.2 Verification & Validation	43
5.2.1 OCS response verification	43
5.2.2 Astrocass case validation	44

5.2.3	V&V Conclusion	46
5.3	Background Noise Rate	46
5.4	Retroreflector radius	49
5.4.1	Case scenario	49
5.4.2	Radius range convergence	50
5.4.3	Radius range convergence with modified AOI	51
5.4.4	Radius range convergence with modified minimum elevation angle	52
5.4.5	Radius range convergence with combined modifications	52
5.4.6	Radius selection	53
5.5	Sensitivity Analysis	54
5.5.1	Reflectivity	55
5.6	Delft Lasercomm Station Recommendations	57
6	Testing & Integration	58
6.1	Retroreflector Inspection	58
6.2	Retroreflector Testing	60
6.3	Retroreflector holder	61
7	Conclusion	64
	References	68
A	PoV Graphs	71
A.1	Configuration 1	71
A.2	Configuration 2	72
A.3	Configuration 3	73
A.4	Configuration 4	74
A.5	Configuration 5	75

List of Figures

1	Render of the retroreflector array integrated on Delfi-Twin.	iv
2.1	Schematic representation of the SLR measurement principle [12].	6
2.2	The Mini-SLR prototype of the DLR institute in Stuttgart [13].	6
2.3	Solid corner cube retroreflector [14]	7
2.4	Laser retroreflectors array for InSight and an International Mars Geophysical Network (MGN) [15].	7
2.5	Increase in range due to atmospheric delay as a function of elevation for a 7-day arc of 11 SLR stations with 15° as cut-off elevation [17].	9
2.6	Broadening signature effect of a spherical satellite with a CCRs array on the reflected laser pulse [22].	11
2.7	Sketch of typical geodetic satellite such as LAGEOS, defining parameters required to discuss satellite impulse response [17]	12
2.8	Flow diagram of the Herstmonceux algorithm	13
2.9	One-way attenuation factor against laser wavelength at sea level and clear visibility $V = 60 \text{ km}$ at $\theta_{zen} = 0^\circ, 50^\circ, 70^\circ$ [28].	16
2.10	Plot of Direct Normal Spectral Irradiance, and Hemispherical Spectral Irradiance [31].	18
2.11	Atmospheric transmittance per wavelength [32].	18
2.12	Sky brightness measurements during the night of the 17 th of May 2023 [33].	19
2.13	Schematic of velocity aberration [37].	21
2.14	Spectral output of the deuterium-halogen lamp when transmitted via unirradiated, 5 kGy, 25 kGy and 50 kGy irradiated BK7 glass collection optics [41].	24
2.15	Spectral output of the deuterium-halogen lamp when transmitted via unirradiated, 5 kGy, 25 kGy and 50 kGy irradiated UV-grade fused silica (UVFS) glass collection optics. [41].	24
2.16	Delfi-C3.	26
2.17	Delfi-n3Xt.	26
2.18	Delfi-PQ.	26
2.19	3P PocketQube case baseline configuration [46].	27
2.20	PocketQube protrusions envelope allowance [46].	27
3.1	Orbital pass at zenith with one retroreflector constantly pointing nadir.	31
3.2	Multiple orbital passes at different inclinations with one retroreflector constantly pointing nadir.	31
3.3	Angle of incidence map from the Delft station for 1 retroreflector always pointing nadir.	31
3.4	Map of visibility satellite positions for 1 retroreflector always pointing nadir.	31
3.5	Average probability of visibility with max-min variation with 4 retroreflectors, one on each face for rolling rates 5-10 deg/s and starting offsets 0-80 deg.	32
3.6	OCS w.r.t. off-axis angle for different AOI with radius 0.014 m using Potsdam and $n_{pe} = 10$	33
4.1	Field of view of the retroreflector array on the Astrocast satellite [49].	36
4.2	Sketch of the top view of CONF-1, 1 face.	36
4.3	Sketch of the bottom view of CONF-2, Astrocast.	36
4.4	Sketch of the top view of CONF-3, 4 faces.	36
4.5	Sketch of the top view of CONF-4, 8 faces.	36
4.6	Sketch of the top view of CONF-5, 8 faces alt.	36
4.7	Roll, yaw and pitch.	37
4.8	Visibility map of Astrocastp1 pass of 2020-07-22.	38
4.9	Visibility map of Astrocastp1 pass of 2020-07-14.	38
4.10	Visibility map of Astrocastp1 pass of 2020-06-12.	39

4.11	Visibility map of Astrocstp1 pass of 2020-06-11.	39
4.12	Combined graph of average PoV per elevation angles of all tested configuration for attitude 1.	40
4.13	Combined graph of average PoV per elevation angles of all tested configuration for attitude 2.	40
4.14	Combined graph of average PoV per elevation angles of all tested configuration for attitude 3.	41
5.1	Required optical cross section for on-axis reflection w.r.t. AOI of laser beam to reach $n_{pe} = 10$	43
5.2	Required retroreflector radius for on-axis reflection w.r.t. AOI of laser beam to reach $n_{pe} = 10$	43
5.3	OCS w.r.t. off-axis angle for different AOI comparison with Meyer case.	44
5.4	Normalized OCS difference w.r.t. off-axis angle for different AOI comparison with Meyer case.	44
5.5	OCS w.r.t. off-axis angle for different AOI with Astrocst scenario settings at 39.06° of elevation.	45
5.6	OCS w.r.t. off-axis angle for different AOI with Astrocst scenario settings at 16.77° of elevation.	45
5.7	Visibility of Astrocstp1 pass of 2020-07-22 at an elevation of 39.06° for an AOI range between 30° - 40°.	45
5.8	Visibility of Astrocstp1 pass of 2020-06-11 at an elevation of 16.77° for an AOI range between 30° - 42°.	45
5.9	Probability of false alarm as a function of detection threshold.	47
5.10	Probability of detection as a function of the receiving mean signal photo-electron.	47
5.11	OCS w.r.t. off-axis angle for different AOI with radius 6.1 mm at 40° elevation using Matera during daylight.	50
5.12	OCS w.r.t. off-axis angle for different AOI with radius 12 mm at 40° elevation using Matera during daylight.	50
5.13	PoV curve per elevation angle with decreasing AOI range for attitude 3 with the 8 retroreflector array configuration	51
5.14	PoV curve per elevation angle with AOI range between 10° and 40° for attitude 3 with the 8 retroreflector array configuration	54
5.15	OCS w.r.t. off-axis angle for different AOI with diameter 12.7 mm at 20° elevation using Matera during nighttime.	54
5.16	OCS w.r.t. off-axis angle for different AOI with diameter 12.7 mm at 40° elevation using Potsdam during nighttime.	54
5.17	Aluminum coated typical reflectance performance over wavelength [40].	56
6.1	RT-08.	59
6.2	RT-18.	59
6.3	RT-21.	60
6.4	RT-25.	60
6.5	RT-08 sealed in a plastic zip-lock with its identifier.	60
6.6	Original box from Edmund Optics.	60
6.7	Sketch of the retroreflector holder.	61
6.8	Render of the retroreflector holder.	61
6.9	Integration of the retroreflector holder with protrusion allowances.	62
6.10	PoV curve per elevation angle for attitude 3 with the modified 8 retroreflector array configuration	62
A.1	Zenith pass of configuration 1 with attitude 1.	71
A.2	Zenith pass of configuration 1 with attitude 2.	71
A.3	Zenith pass of configuration 1 with attitude 3.	71
A.4	Visibility map of configuration 1 with attitude 1.	72
A.5	Visibility map of configuration 1 with attitude 2.	72
A.6	Visibility map of configuration 1 with attitude 3.	72

A.7 Average PoV per elevation angle of configuration 1 with attitude 1.	72
A.8 Average PoV per elevation angle of configuration 1 with attitude 2.	72
A.9 Average PoV per elevation angle of configuration 1 with attitude 3.	72
A.10 Zenith pass of configuration 2 with attitude 1.	72
A.11 Zenith pass of configuration 2 with attitude 2.	72
A.12 Zenith pass of configuration 2 with attitude 3.	72
A.13 Visibility map of configuration 2 with attitude 1.	73
A.14 Visibility map of configuration 2 with attitude 2.	73
A.15 Visibility map of configuration 2 with attitude 3.	73
A.16 Average PoV per elevation angle of configuration 2 with attitude 1.	73
A.17 Average PoV per elevation angle of configuration 2 with attitude 2.	73
A.18 Average PoV per elevation angle of configuration 2 with attitude 3.	73
A.19 Zenith pass of configuration 3 with attitude 1.	73
A.20 Zenith pass of configuration 3 with attitude 2.	73
A.21 Zenith pass of configuration 3 with attitude 3.	73
A.22 Visibility map of configuration 3 with attitude 1.	74
A.23 Visibility map of configuration 3 with attitude 2.	74
A.24 Visibility map of configuration 3 with attitude 3.	74
A.25 Average PoV per elevation angle of configuration 3 with attitude 1.	74
A.26 Average PoV per elevation angle of configuration 3 with attitude 2.	74
A.27 Average PoV per elevation angle of configuration 3 with attitude 3.	74
A.28 Zenith pass of configuration 4 with attitude 1.	74
A.29 Zenith pass of configuration 4 with attitude 2.	74
A.30 Zenith pass of configuration 4 with attitude 3.	74
A.31 Visibility map of configuration 4 with attitude 1.	75
A.32 Visibility map of configuration 4 with attitude 2.	75
A.33 Visibility map of configuration 4 with attitude 3.	75
A.34 Average PoV per elevation angle of configuration 4 with attitude 1.	75
A.35 Average PoV per elevation angle of configuration 4 with attitude 2.	75
A.36 Average PoV per elevation angle of configuration 4 with attitude 3.	75
A.37 Zenith pass of configuration 5 with attitude 1.	75
A.38 Zenith pass of configuration 5 with attitude 2.	75
A.39 Zenith pass of configuration 5 with attitude 3.	75

List of Tables

2.1	Main range corrections' values and uncertainties	8
2.2	Improved mapping function sub-coefficients of the FCULa model [19].	10
2.3	Average, 10% percentile, 50% percentile, and the maximum value of sky brightness collected in Delft since May 2023 [33].	19
2.4	Characteristics of three different type of CCRs [37]	23
2.5	Main specifications of the specular retroreflector prisms with backside gold coating from Thorlabs [14].	23
2.6	Main specifications of the aluminum coated fused silica corner cubes from Edmund Optics [40].	23
2.7	Main specifications of the Mini-SLR optical system.	25
2.8	Main specifications of TU Delft lasercom station.	25
2.9	Main specifications of station 14473 in Potsdam of the ILRS network [43].	25
2.10	Main specifications of station 7941 in Matera of the ILRS network [44].	25
4.1	Position parameters of Astrocstp1 during first and last measurement of the orbital pass above Graz of 2020-07-22.	38
4.2	Position parameters of Astrocstp1 during first and last measurement of the orbital pass above Graz of 2020-07-14.	38
4.3	Position parameters of Astrocstp1 during first and last measurement of the orbital pass above Graz of 2020-06-12.	39
4.4	Position parameters of Astrocstp1 during first and last measurement of the orbital pass above Graz of 2020-06-11.	39
4.5	Average, standard deviation and limit value for each configuration for attitude 1.	40
4.6	Average, standard deviation and limit value for each configuration for attitude 2.	40
4.7	Average, standard deviation and limit value for each configuration for attitude 3.	41
5.1	Meyer case scenario settings [38].	44
5.2	Main specifications of station 7839 in Graz of the ILRS network [54].	45
5.3	Astrocast satellite scenario settings [49].	45
5.4	Background photo-electron rate during daytime and its components for each considered station.	47
5.5	Background photo-electron rate during nighttime and its components for each considered station.	47
5.6	Required mean number of returning photo-electrons during daytime and its components for each considered station.	48
5.7	Required mean number of returning photo-electrons during nighttime and its components for each considered station.	48
5.8	Case scenario settings	49
5.9	Converging retroreflector radius range per station during daylight.	50
5.10	Converging retroreflector radius range per station during nighttime.	50
5.11	PoV values at different AOI ranges for attitude 3 with the 8 retroreflector array configuration	51
5.12	Converging retroreflector radius range per station during daylight with limited AOI.	51
5.13	Converging retroreflector radius range per station during nighttime with limited AOI.	52
5.14	Converging retroreflector radius range per station during daylight with limited minimum elevation angle.	52
5.15	Converging retroreflector radius range per station during nighttime with limited AOI and minimum elevation angle.	52
5.16	Converging retroreflector radius range per station during daylight with limited minimum elevation angle.	53

5.17	Converging retroreflector radius range per station during nighttime with limited AOI and minimum elevation angle.	53
5.18	Converging retroreflector radius range increase for Potsdam station during daytime and nighttime.	53
5.19	Elevation and angle of incidence variations in returning photon count for Potsdam.	54
5.20	Atmospheric conditions variations in returning photon count for Potsdam.	55
5.21	Variations in returning photon count for Potsdam with satellite altitude set to 600 km.	55
5.22	Reflectivity variations in returning photon count for Potsdam.	56
5.23	Converging retroreflector radius range per station during nighttime with limited AOI and minimum elevation angle and reflectivity of 57%.	56
5.24	Converging retroreflector radius range for Delft laser communication station during daytime and nighttime for an increased laser power.	57
6.1	Retroreflector catalog.	59
6.2	PoV values comparison for attitude 3 with the modified 8 retroreflector array configuration	62
7.1	Compliance matrix for requirements.	65
7.2	Compliance matrix for research questions.	66

Nomenclature

Abbreviations

AOI	Angle of Incidence
APU	Auxiliary Propulsion Unit
CCR	Cube Corner Retroreflector
CoM	Center of Mass
COTS	Commercial Off-The-Shelf
CPF	Consolidated Prediction Format
CRD	Consolidated Range Data
DSE	Department of Space Engineering
DLR	Deutsches Zentrum für Luft-und Raumfahrt
ESA	European Space Agency
FFDP	Far-Field Diffraction Pattern
FoV	Field of View
GNSS	Global Navigation Satellite System
GSFC	Goddard Space Flight Center
IAG	International Association of Geodesy
ILR	Interplanetary Laser Ranging
ILRS	International Laser Ranging Service
ITRF	International Terrestrial Reference Frame
LLR	Lunar Laser Ranging
LRO	Lunar Reconnaissance Orbiter
MF	Mapping Function
MGN	Mars Geophysical Network
OCS	Optical Cross Section
OOK	On-Off Keying
PoV	Probability of Visibility
RMS	Root Mean Square
SLR	Satellite Laser Ranging
SLRF	Laser Ranging Reference Frame
TLE	Two-line elements
ToF	Time of Flight

1

Introduction

The first launch of Ariane 6 took place on July 9, 2024, marking a significant milestone in Europe's space transportation capabilities. From lift-off through the deployment of its eight satellite payload into a 580 km orbit, the launch was considered a success [1]. However, during the final phase, when the Vinci engine was expected to ignite for the third time to place the upper stage into a re-entry orbit for safe burn-up in Earth's atmosphere, the mission encountered an unexpected software malfunction. A sensor registered an excessively high temperature, causing the flight software to shut down the Auxiliary Propulsion Unit (APU) of the upper stage, preventing the third ignition of the Vinci engine [2]. As a result, the deorbit burn was not performed, and the upper stage passivated itself by cutting power to all onboard systems to mitigate the risk of explosions and avoid the generation of space debris. The shutdown of the attitude determination and control system left the upper stage in an unknown attitude. If the upper stage had been equipped with retroreflector arrays, Satellite Laser Ranging (SLR) could have provided an immediate and accurate solution to determine its position and attitude. Fortunately, the upper stage is a large object, and with the help of other systems like cameras, it was later determined to be stable in a low orbit. The Ariane 6 software malfunction is just one instance where SLR could have improved space management by enhancing satellite safety and supporting operational decision-making, thanks to its passive space segment.

Delfi-PQ, a satellite launched by TU Delft in 2022, was equipped with four retroreflectors intended for SLR measurements to validate Global Navigation Satellite System (GNSS) data and serve as a demonstration. However, ground stations were unable to retrieve SLR data from Delfi-PQ due to sub-optimal retroreflector selection and array design. Despite this, TU Delft is currently developing two new platforms: Delfi-Twin, the successor of Delfi-PQ, and the Da Vinci satellite, which will participate in the European Space Agency (ESA) program "Fly Your Satellite." Both platforms require the implementation of SLR capabilities, leading to the following need:

With the development of TU Delft new platforms, there is a need for an optimized design of the retroreflector array to successfully perform SLR measurements.

This thesis aims to document the research conducted to address the need for designing an effective and optimized retroreflector array for TU Delft new platforms, while also considering the potential ground stations that could be used for the measurements. TU Delft is currently constructing a laser communication terminal on top of the Aerospace Faculty building, with plans to use it for these measurements. Nevertheless, the International Laser Ranging Service (ILRS) remains the state-of-the-art network for SLR measurements. Based on this need, the following research objectives and related questions were formulated:

- **RO-1:** Design a retroreflector array to be mounted on the new TU Delft platforms to obtain Time of Flight (ToF) measurements utilizing a laser ranging terminal from the ILRS network.
 - **RQ-1:** Is it technically feasible to obtain SLR measurements using a retroreflector array mounted on the new TU Delft platforms and a laser ranging terminal from the ILRS network?

- **RO-2:** Design a retroreflector array to be mounted on the new TU Delft platforms to obtain ToF measurements utilizing the laser communication terminal at Delft University.
 - **RQ-2:** Is it technically feasible to obtain SLR measurements using a retroreflector array mounted on the new TU Delft platforms and the laser communication terminal at Delft university?

From these research questions, four sub-questions were generated, aimed at exploring specific technical aspects of the proposed designs:

- **RSQ-1:** What is the optimal shape and design of the retroreflector array to maximize coverage while facilitating integration with the new TU Delft platforms?
- **RSQ-2:** What is the optimal retroreflector radius, and thus the required Optical Cross Section (OCS), to effectively facilitate SLR operations for both the laser communication terminal and the ILRS terminal?
- **RSQ-3:** What are the requirements for the laser communication terminal at Delft University of Technology to establish reliable SLR measurements?
- **RSQ-4:** How do the Angle of Incidence (AOI) of laser beams and environmental radiation affect the strength and reliability of the reflected signals in SLR operations?

The thesis is divided into seven chapters. In chapter 2, a comprehensive literature review is conducted to gather insights on the state-of-the-art technologies related to SLR and the theoretical principles behind designing an SLR system. Additionally, post-processing methods used to accurately determine the distances between ground stations and satellites are discussed. Chapter 3 establishes the framework that integrates the rationale behind the simulations with the underlying requirements related to the research questions and objectives. This chapter provides a high-level overview of the thesis structure, key components, and the methods employed. In chapter 4, the Probability of Visibility (PoV) simulation is performed to identify the array configuration that maximizes coverage at all elevation angles, based on the satellite attitude. The configuration of the array is finalized in this chapter. Chapter 5 discusses the outcomes of the link budget analysis, which aims to select the optimal retroreflector size for the new TU Delft platforms, considering the configurations of various ground stations. Recommendations are also provided for the Delft laser communication station to ensure successful laser ranging with the selected array. Chapter 6 presents the inspection and potential testing of the ordered retroreflectors, which is crucial for qualifying them for integration into the satellite array. Additionally, the preliminary design of the array holder is carried out. Finally, chapter 7 gathers the outcomes of the research, answers the research questions, and provides recommendations for future work. Supporting graphs generated during the PoV simulation for each satellite attitude and array configuration are compiled in Appendix A.

2

Literature Review

This chapter presents a literature review survey conducted to gain insights into the state-of-the-art technologies of SLR, as well as to understand the process behind the design of an SLR system and the post-processing methods used to determine the accurate distances between the ground stations and the satellites.

Section 2.1 provides an overview of the history of SLR and the current state-of-the-art systems, describing the basic principles behind SLR measurements. Section 2.2 explains the algorithm used for post-processing SLR data. Furthermore, section 2.3 presents formulations for designing satellite retroreflectors based on the required strength of the returning signal. Section 2.4 gives an overview of the parameters of the considered ground stations. Finally, section 2.5 elaborates on TU Delft satellite legacy, introducing the parameters of interest for the new TU Delft platforms, Delfi-Twin and the Da Vinci satellite.

The literature review followed a structured approach guided by the following research questions:

- Q1) What is SLR, and what are the state-of-the-art techniques?
- Q2) What are the basic principles of SLR?
- Q3) What are the different types of applications of SLR?
- Q4) How is the position of the satellite determined from ToF measurements?
- Q5) What are the requirements for the space segment to achieve ranging measurements?
- Q6) What is the design process of a retroreflector array?
- Q7) What are the common parameters of typical SLR ground stations?
- Q8) What are the specifications of the new TU Delft platforms?

2.1. Satellite Laser Ranging

In this section, the history and state-of-the-art technologies of SLR are discussed, alongside an exploration of the basic principles behind SLR measurements. Additionally, a thorough comparison between the implementation of radio ranging measurements and laser ones is undertaken. Finally, several applications of SLR systems in scientific missions are listed.

2.1.1. History of Satellite Laser Ranging

In 1964, the first laser range measurements took place at NASA's Goddard Space Flight Center (GSFC) to Beacon-B, an artificial satellite equipped with optical retroreflectors [3]. These measurements achieved a ten-meter accuracy, marking a significant advancement in technology. However, these initial systems relied on cameras, which provided bias-free angular position measurements but were affected by photographic limitations of 1-2 arcsec and vulnerability to weather conditions [4]. Over time, these photographic constraints were overcome, and advancements in laser technology, coupled with increases

in computational power of modern computers and refinement of atmospheric propagation models, propelled SLR measurements to millimeter-level accuracy.

Today, a global network of stationary and mobile satellite laser ranging ground stations, the ILRS, covers most of the globe and serves as a crucial interface for SLR measurements to geodetic satellites, GNSS, and commercial satellites [5]. The high level of accuracy of SLR compared to radar ranging measurements has made it an essential tool for geodetic science missions, refining models of Earth's gravitational field and internal mass redistribution. Additionally, sets of retroreflector arrays were placed on the moon, enabling Lunar Laser Ranging (LLR) measurements. LLR provided insights into Earth-lunar dynamics, including the motion of the center of mass (lunar ephemeris), rotations about the center of mass (librations), internal mass distribution (moments of inertia), and lunar tides [6].

Moreover, Interplanetary Laser Ranging (ILR) measurements have been tested, differing from classical SLR retroreflectors passive systems for the implementation of transponders on the satellites due to the large distances the laser beam has to travel [7]. These measurements aim to complement radar Doppler data to exploit the advantages of both technologies. To date, the only operational implementation of ILR has been on the Lunar Reconnaissance Orbiter (LRO), using the laser altimeter system. However, no mission with dedicated hardware has been created, thus the accuracy has not yet been pushed to the limit.

SLR has become an essential technology for satellite ranging and science missions. Increasingly, satellites implement retroreflectors, even if ranging accuracy is not their primary objective, as the implementation of passive SLR systems serves as a practical backup for determining satellite positions in cases of satellite control loss or failure of other orbit determination systems.

2.1.2. Radio vs Laser

The choice between radio and laser technologies for satellite ranging is pivotal in determining the precision, reliability, and versatility of ranging measurements. Here, we delve into a comprehensive comparison of the two:

- **Laser:** Laser ranging represents a pinnacle of precision, offering unparalleled accuracy for range calculations down to the millimeter level. This precision has made it indispensable for a wide array of scientific and geodetic applications. Moreover, the passive nature of laser payloads makes them highly attractive for Earth orbiting satellites, minimizing the need for additional power and resources.

However, laser measurements are not without their challenges. Weather conditions, such as fog or clouds, can obstruct or distort laser signals, impacting the reliability of ranging measurements. Furthermore, the absence of Doppler measurements in laser ranging systems precludes the determination of relative velocity between satellites or other celestial bodies, limiting its utility in certain scenarios where velocity data is crucial.

- **Radar:** Radar systems, on the other hand, excel in providing Doppler measurements, enabling precise determination of relative velocity. This capability is particularly valuable in applications such as space debris tracking, where understanding relative motion is essential for collision avoidance maneuvers. Moreover, radar systems boast impressive accuracy for relative velocity calculations, achieving precision at the level of millimeters per second.

However, the accuracy of radar for range calculations is generally limited to the meter level [8]. This limitation may be acceptable for some applications but can pose challenges in scenarios requiring higher precision. Additionally, radar systems face difficulties in distinguishing between multiple objects, especially in crowded orbital environments, due to their large bandwidth.

In conclusion, while laser and radar technologies each offer unique strengths and limitations, their combination can result in a synergistic effect that enhances the capabilities of satellite ranging missions. By leveraging the precision of laser ranging for accurate distance measurements and the Doppler capabilities of radar for relative velocity determination, missions can achieve comprehensive and robust tracking solutions. Understanding the complementary nature of these technologies and integrating them effectively is key to maximizing the success of satellite missions in diverse operational contexts.

2.1.3. Type of Applications

Satellite laser ranging serves a multitude of purposes beyond merely determining the position of satellites. Its millimeter level accuracy lends itself to various geodetic applications:

- **Maintaining the International Terrestrial Reference Frame (ITRF):** SLR contributes to the development of a Laser Ranging Reference Frame (SLRF), ensuring the precision and consistency of the global reference frame used in geodesy, the ITRF [9].
- **Precise calibration of radar altimeters:** SLR aids in the calibration of radar altimeters and helps separate long-term instrumentation drift from secular changes in ocean topography, ensuring accurate measurements of sea level and oceanic processes [10].
- **Reference for post-glacial rebound, sea level, and ice volume change:** SLR provides a reference system for studying post-glacial rebound, sea level variations, and changes in ice volume, facilitating research into climate change and its impacts on Earth's surface [10].
- **Determining temporal mass redistribution:** By monitoring temporal mass redistribution within the solid Earth, oceans, and atmosphere, SLR contributes to understanding dynamic processes such as tectonic movements and changes in Earth's gravitational field [10].
- **Monitoring atmospheric response to seasonal variations:** SLR data helps monitor the response of the atmosphere to seasonal variations in solar heating, aiding in the study of atmospheric dynamics and climate patterns [10].
- **Testing the theory of general relativity:** SLR provides a basis for special tests of the theory of general relativity, contributing to our understanding of fundamental physics and gravitational interactions [10].
- **Modeling convection in Earth's mantle:** SLR data provides constraints on processes as mantle convection, helping to model the dynamics of Earth's interior and geological processes [10].
- **Modeling gravitational fields:** SLR contributes to the modeling of the gravitational fields of Earth and other planets, providing valuable insights into planetary dynamics and structure [10].
- **Space debris orbit determination:** SLR could be implemented in the precise determination of the orbits of space debris, crucial for debris mitigation efforts and ensuring the safety of space missions [11].

In essence, SLR serves as a versatile tool for geodetic research, providing precise measurements that contribute to our understanding of Earth's dynamics, climate, and fundamental physical processes.

2.1.4. Basic Principles

Satellite laser ranging involves the emission of short laser pulses from a ground-based station towards an object into orbit or a satellite with mounted retroreflectors. The retroreflectors, typically consisting of an array of corner cube prisms, are designed to reflect incident light back towards its source regardless of the angle of incidence ensuring that the laser pulses return to the ground station with minimum deviation. By measuring the time between the emission of the laser pulse and its reception, also called as ToF, SLR system can determine the distance, d , between the ground station and the satellite. A schematic of the SLR principle is shown in Figure 2.1.

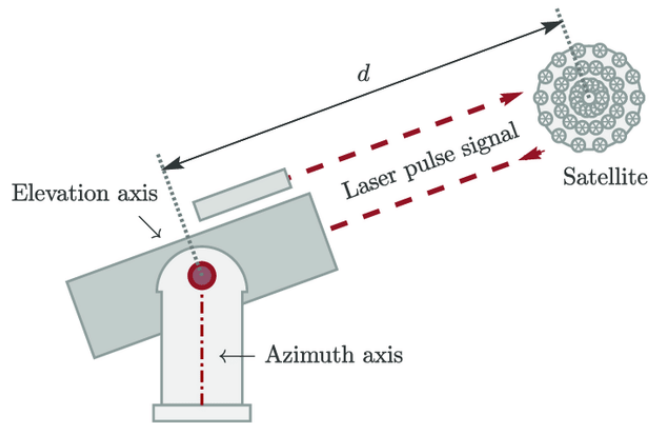


Figure 2.1: Schematic representation of the SLR measurement principle [12].

The distance calculation principle is straightforward as the laser pulses travel at the speed of light, c . Therefore, the distance can be calculated with Equation 2.1.

$$d \approx \frac{ToF \cdot c}{2} \quad (2.1)$$

However, while Equation 2.1 encapsulates the ranging calculation principle, it only provides a rough approximation of the distance. In fact, corrections due to laser propagation through the atmosphere, discrepancies in clock timing and station biases, along with other induced delays, need to be taken into account as they can severely affect range measurements. The induced time delays depend on a multitude of factors, including atmospheric conditions at the time of the emission of the laser pulse.

2.1.5. SLR System

A ground segment and a space segment are identified in an SLR system. An example of a ground segment is the Mini-SLR ground station at Deutsches Zentrum für Luft-und Raumfahrt (DLR) in Stuttgart. An overview is shown in Figure 2.2.



Figure 2.2: The Mini-SLR prototype of the DLR institute in Stuttgart [13].

The following components of the ground segment can be identified:

- **Laser source:** Generates a train of laser pulses.
- **Telescope:** Collects the returning signal.
- **Tracking gimbal and control system:** Points the laser towards the satellite.

- **Detector:** Detects the returning photons. The detector can be either single-mode or multi-mode. The difference lies in when a returning signal is considered such – either after a single photon hits the detector or when multiple photons do.
- **Optical components:** Used to achieve defined beam size and beam divergence.
- **Time of Flight receiver:** Records the time of departure and reception of the laser pulses.
- **Meteorological station:** Records surface temperature, pressure, and humidity for time of flight corrections.
- **Data storage unit:** Used to store the collected measurements.

An SLR ground station can be either mono-static or bi-static. In the former, the transmitting and receiving beams follow the same optical path. In these cases, polarized beam splitters need to be implemented to distinguish between the transmitting and receiving beams. The latter setup consists of a configuration in which the transmitting and receiving beams follow two different optical paths.

The space segment of an SLR system can be either passive or active. As introduced earlier, most of the satellites that support SLR measurements have implemented a passive system consisting of single Cube Corner Retroreflector (CCR) or an Array of CCRs, depending on the required OCS to achieve the desired return signal strength. In Figure 2.3 and Figure 2.4, a Single CCR and an array of CCRs are shown respectively.



Figure 2.3: Solid corner cube retroreflector [14]



Figure 2.4: Laser retroreflectors array for InSight and an International MGN [15].

When the distances the beam has to travel are too long, as in the case of ILR, an active space segment needs to be implemented. This usually consists of a transponder which generates a returning train of laser pulses.

2.2. Range Model

After collecting ToF data from a satellite passing through the Field of View (FoV) of an SLR station, post-processing is required to correct for induced time delays and to aggregate multiple data points, generating an accurate estimate of the range between the station and the satellite. In this section, the range correction models and algorithms implemented as standard by the ILRS network are discussed.

2.2.1. Range Data Point

An SLR station typically operates at frequencies ranging from 5 to 10 Hz, while newer systems can reach repetition rates of 100 Hz to kHz [16]. Consequently, during a single satellite pass, thousands of data points are collected. The ILRS network collects the full rate of data points in the Consolidated Range Data (CRD) format [5], including ToF information, satellite parameters, and weather conditions such as pressure, temperature, and humidity at each epoch of the data point. The time of flight data point, DP, at a given epoch is considered as the point of departure. This DP can be easily converted

to a range data point, DPR, in meters using Equation 2.2.

$$DPR_i = \frac{1}{2} \cdot \left(\frac{DP_{ToF_i}}{1 \cdot 10^{12}} \cdot c \right) \quad (2.2)$$

Where DP_{ToF_i} represents the time of flight of a laser pulse emitted at epoch i in picoseconds, and c is the speed of light. The range found needs to be corrected by taking into account the effects of the atmosphere, Δ_a , the offset with the satellite center-of-mass, Δ_{CoM} , SLR station range biases, Δ_{bias} , relativistic correction, Δ_{rel} , and random errors, Δ_ϵ [17]. Factoring in all the correction factors leads to Equation 2.3.

$$DPR_i = \frac{1}{2} \cdot \left(\frac{DP_{ToF_i}}{1 \cdot 10^{12}} \cdot c \right) - \Delta_a + \Delta_{CoM} - \Delta_{bias} - \Delta_{rel} - \Delta_\epsilon \quad (2.3)$$

These correction factors can be expressed in time or range values. To convert between units, it is sufficient to multiply by the speed of light. The main correction values and their uncertainties are summarized in Table 2.1. These values are indicative, as the corrections depend on the specific station and satellite.

Table 2.1: Main range corrections' values and uncertainties

Correction	Range Value	Time Value	Uncertainty
Atmospheric Propagation	2-8.5 m	6.67-28.35 ns	1-16 mm
Center of Mass	~250 mm	~0.83 ns	1-5 mm
Station Biases	0.001-300 m	0.1-1000 ns	few mm
Relativistic	0.1-1 mm	few ps	few mm

The result of Equation 2.3 is considered as the observed range, and it is used together with predicted range values in the algorithm to calculate the residuals as part of the SLR data analysis process.

2.2.2. Correction Factors

The correction factors to be taken into account when retrieving the observed range from the ToF of the laser pulses are discussed in this subsection.

Atmospheric Delay

When passing through the atmosphere, the train of laser pulses emitted by an SLR ground station is affected by atmospheric propagation delay. The main two effects that cause this delay are both associated to the change in the index of refraction, n , within each atmospheric layer. The first effect is the velocity change due to refractive index variation. The speed of light in a medium is determined by the refractive index, n , of that medium. As light passes through different layers of the atmosphere with varying refractive indices, its velocity changes according to Equation 2.4, where v is the velocity of the light in the medium.

$$v = \frac{c}{n} \quad (2.4)$$

The other effect is the curvature of light path. In fact, the laser pulses passing through the atmosphere are curved due to the refraction and do not follow a straight path. The atmospheric delay is the largest correction factor of the range model, it can reach several meters as shown in Figure 2.5.

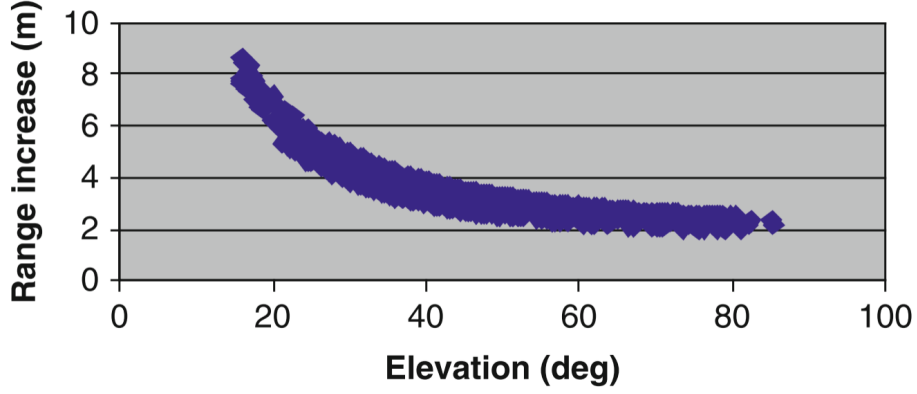


Figure 2.5: Increase in range due to atmospheric delay as a function of elevation for a 7-day arc of 11 SLR stations with 15° as cut-off elevation [17].

Therefore, there is a need of very accurate atmospheric models to correct for the propagation delay, mainly at low elevation angles. An often used atmospheric correction is the Marini-Murray model developed in 1972 [18] and further improved by Mendes et al. with the implementation of newly derived mapping functions for optical wavelengths [19]. A high accuracy zenith delay prediction at optical wavelengths currently implemented by the ILRS analysis group defines the atmospheric propagation delay experienced by a laser signal in the zenith direction with Equation 2.5 [20].

$$d_{atm}^z = d_h^z + d_{nh}^z = 10^{-6} \cdot \int_{r_s}^{r_a} N_h \cdot dz + \int_{r_s}^{r_a} N_{nh} \cdot dz \quad (2.5)$$

In this equation, the atmospheric propagation delay, d_{atm}^z , is divided into a hydrostatic, d_h^z , and a non-hydrostatic, d_{nh}^z , component. The former is also defined as the dry component due to the fact that its refractivity is the results of the dry gases in the troposphere, although it contains the non-dipole component of water vapour refractivity. While, the latter is defined as the wet component. The total group refractivity of moist air is denoted by $N = (n - 1) \cdot 10^6$, where n is the total refractive index of moist air. Furthermore, r_s and r_a are the geocentric radius of the laser station and the geocentric radius of the top of the neutral atmosphere respectively.

Direct equation to calculate the hydrostatic and non-hydrostatic components in the zenith direction are provided in Mendes and Pavlis model analysis [20]. The hydrostatic component, d_h^z , is given by Equation 2.6.

$$d_h^z = 0.002416579 \cdot \frac{f_h(\lambda)}{f_s(\phi, H)} \cdot P_s \quad (2.6)$$

Where P_s is the surface barometric pressure and $f_h(\lambda)$ is the modified group refractivity index of the dry air component, also defined as the dispersion equation, and can be calculated with Equation 2.7.

$$f_h(\lambda) = 10^{-2} \cdot \left[k_1^* \cdot \frac{(k_0 + \sigma^2)}{(k_0 - \sigma^2)^2} + k_3^* \cdot \frac{(k_2 + \sigma^2)}{(k_2 - \sigma^2)^2} \right] \cdot C_{CO_2} \quad (2.7)$$

Where $k_0 = 238.0185 \mu m^{-2}$, $k_1^* = 19990.975 \mu m^{-2}$, $k_2 = 57.362 \mu m^{-2}$ and $k_3^* = 579.55174 \mu m^{-2}$. $\sigma = \lambda^{-1}$ is the wave number with λ in micrometers, and $C_{CO_2} = 1 + 0.534 \cdot 10^{-6} \cdot (x_c - 450)$. Where x_c is the carbon dioxide content in parts per million (ppm), following International Association of Geodesy (IAG) recommendations $x_c = 375 ppm$. Leading to $C_{CO_2} = 0.99995995$. The denominator function in Equation 2.6, $f(\phi, H)$, is given by Equation 2.8.

$$f(\phi, H) = 1 - 0.00266 \cdot \cos(2\phi) - 0.00028 \cdot H \quad (2.8)$$

Where ϕ is the geodetic latitude of the SLR station, and H is the geodetic height in kilometers. The non-hydrostatic component, d_{nh}^z , can be computed with Equation 2.9.

$$d_{nh}^z = 10^{-4} \cdot (5.316 \cdot f_{nh}(\lambda) - 3.759 \cdot f_h(\lambda)) \cdot \frac{e_s}{f_s(\phi, H)} \quad (2.9)$$

Where e_s is the water vapour pressure at the surface which can be calculated with Equation 2.10.

$$e_s = \frac{\left[6.1078 \cdot \left(\frac{7.5 \cdot T}{273.3 + T} \right)^{10} \right] \cdot RH}{100} \quad (2.10)$$

RH represents the relative humidity as a percentage and T is the temperature in degree Celsius. Furthermore, the dispersion formula for the non-hydrostatic component is given by Equation 2.11.

$$f_{nh}(\lambda) = 0.0031101 \cdot (\omega_0 + 3 \cdot \omega_1 \cdot \sigma^2 + 5 \cdot \omega_2 \cdot \sigma^4 + 7 \cdot \omega_3 \cdot \sigma^6) \quad (2.11)$$

Where $\omega_0 = 295.235$, $\omega_1 = 2.6422 \mu m^2$, $\omega_2 = -0.032380 \mu m^4$, $\omega_3 = 0.004028 \mu m^6$.

With the aforementioned equations it is possible to compute the atmospheric propagation delay in the zenith direction, d_{atm}^z . However, in order to compute the delay in the direction of ranging, d_{atm} , a Mapping Function (MF) needs to be implemented to map the delay to the elevation angle, e , at which the laser beam is being fired. Due to the fact that the refraction of water vapour at visible wavelengths is small compared to the total refractivity, a single MF can be applied to the atmospheric propagation delay in the zenith direction as shown in Equation 2.12. However, if the wavelength of the laser is not in the visible range, different MFs need to be developed and applied to the hydrostatic and non-hydrostatic components.

$$d_{atm} = d_{atm}^z \cdot m(e) \quad (2.12)$$

The MF developed by Mendes is based on a truncated form of the Marini continued fraction in terms of $1/\sin(e)$, normalised to unity. The MF can be calculated with Equation 2.13.

$$m(e) = \frac{1 + \frac{a_1 \frac{a_2}{1 + \frac{a_2}{1 + a_3}}}{\sin(e) + \frac{a_1 \frac{a_2}{\sin(e) + \frac{a_2}{\sin(e) + a_3}}}}{\sin(e) + \frac{a_1 \frac{a_2}{\sin(e) + \frac{a_2}{\sin(e) + a_3}}} \quad (2.13)$$

The coefficients, a_i , can be found using the formulation in Equation 2.14 suggested by Mendes in its improved mapping function model called FCULa [19]. The values of the sub-coefficients can be found in Table 2.2.

$$a_i = a_{i0} + a_{i1} \cdot T_s + a_{i2} \cdot \cos(\phi) + a_{i3} \cdot H \quad (2.14)$$

Where T_s is the temperature at the station in degree Celsius, ϕ is the altitude of the station, and H is the height of the station in meters.

Table 2.2: Improved mapping function sub-coefficients of the FCULa model [19].

a_{ij}	Value
a_{10}	$1.21008 \cdot 10^{-3}$
a_{11}	$1.7295 \cdot 10^{-6}$
a_{12}	$3.191 \cdot 10^{-5}$
a_{13}	$-1.8478 \cdot 10^{-8}$
a_{20}	$3.04965 \cdot 10^{-3}$
a_{21}	$2.346 \cdot 10^{-6}$
a_{22}	$-1.035 \cdot 10^{-4}$
a_{23}	$-1.856 \cdot 10^{-8}$
a_{30}	$6.8777 \cdot 10^{-2}$
a_{31}	$1.972 \cdot 10^{-5}$
a_{32}	$-3.458 \cdot 10^{-3}$
a_{33}	$1.06 \cdot 10^{-7}$

The atmosphere propagation model described in this section can be utilized to derive the atmospheric range correction to be applied to SLR ToF measurements. This model tends to degrade from low to high latitudes of the stations due to higher seasonal variations of surface temperature. However, it achieves high accuracy up to low elevation angles, with a standard deviation of 1 mm, 4 mm, and 16 mm for 15°, 10°, and 6° elevation angles, respectively. Nonetheless, if the laser wavelength lies outside

the visible range, the mapping function developed in this section needs to be revised to individually map the hydrostatic and non-hydrostatic components of the propagation delay. This may require the introduction of more complex models, such as the Vienna Mapping Function for optical wavelengths (VMF30) [21]. However, if the elevation angles at which the measurements are performed do not go below 20° , the impact of the mapping function might not be significant, relieving the necessity of developing new mapping functions.

Center of Mass Correction

Another effect that induces a time delay, which needs to be corrected in the range model, is the offset between the front face of the CCR that is hit by the laser beam wavefront and the actual Center of Mass (CoM) of the satellite. The center of mass correction is unique per satellite due to different shapes and configurations of CCR arrays. To retrieve the CoM signature of a satellite, its response function needs to be analyzed. As a consequence of having multiple CCRs within the array, the response signal is broadened. This characteristic is shown schematically in Figure 2.6. In fact, the CCR which is perpendicular to the approaching laser beam will reflect the signal before the CCRs which have an offset in incidence angle, resulting in a time delay in the reflected signal.

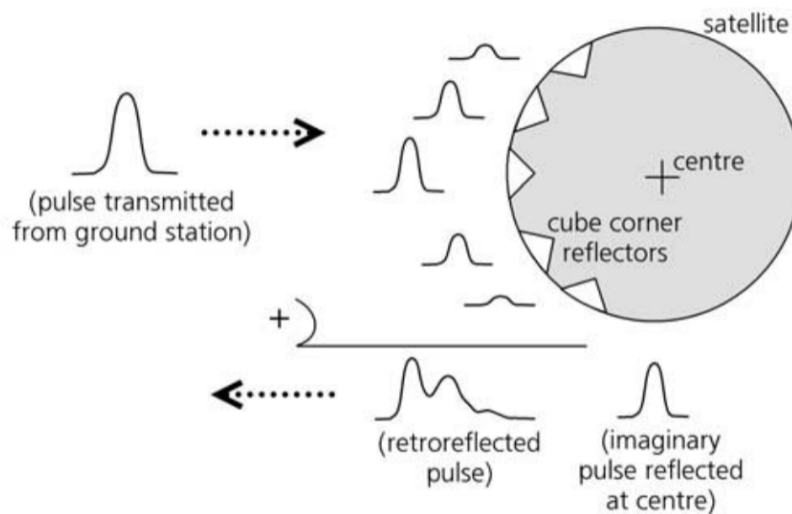


Figure 2.6: Broadening signature effect of a spherical satellite with a CCRs array on the reflected laser pulse [22].

Moreover, a phase delay can also be observed due to the same principle, and if individual reflector responses overlap, destructive interference could be witnessed. To compute the time delay per CCR, the sketch shown in Figure 2.7 is used to geometrically explain the parameters involved in the CoM characterization.

laser pulse, it is impossible to specify which photon in the pulse it was, leading to time uncertainty. Moreover, having a high repetition rate will result in multiple pulses flying simultaneously towards the target satellite, making it unfeasible to match the returning pulse to a specific emitted pulse. These biases typically range within a few millimeters and are specifically characterized for each SLR station.

Relativistic Correction

When light propagates within a reference frame containing multiple masses, space and time are warped, deviating the light path and introducing relativistic time delays. Equation 2.17 encapsulates the effect of gravitational masses on the travel time of the laser [24].

$$t_2 - t_1 = \frac{|\vec{x}_2(t_2) - \vec{x}_1(t_1)|}{c} + \sum_J \frac{2 \cdot G \cdot M_J}{c^3} \cdot \ln \left(\frac{r_{j1} + r_{j2} + \rho}{r_{j1} + r_{j2} - \rho} \right) \quad (2.17)$$

The sum of all bodies, J , with mass M_j centered at x_j is considered. While, $r_{j1} = |\vec{x}_1 - \vec{x}_j|$, $r_{j2} = |\vec{x}_2 - \vec{x}_j|$, and $\rho = |\vec{x}_2 - \vec{x}_1|$. In practice, ρ is the range between ground station and satellite before the relativistic correction is applied. For near-Earth satellites, analyses are done in the geocentric frame of reference, and the only body to be considered in the relativistic correction model is the Earth.

2.2.3. Normal Point Algorithm

After collecting the full-rate ToF data from an SLR station, data centers utilize the Herstmonceux algorithm to post-process the data and generate normal points [25]. This procedure aims to reduce the size of the data package for further analyses. With the normal point algorithm, the size of the data package can be decreased from thousands of data points to hundreds of normal points. For example, the full-rate data of LAGEOS-1 from station 8834 in September 2019 consisted of 140,718 points, and after implementing the algorithm, only 311 normal points were obtained [26]. The Herstmonceux algorithm requires as input the full-rate data of the SLR station and the orbit predictions of the observed satellite. Data of orbit predictions can be found per satellite on the ILRS website in the Consolidated Prediction Format (CPF). Predictions are obtained using orbit propagation models, which predict the future satellite position and velocity based on its current state.

The Herstmonceux algorithm consists of two stages. The first stage involves screening the full-rate data with respect to predicted ranges to remove outliers. The second stage involves forming normal points using the accepted data points from stage one. The steps to be taken within these stages are displayed in the flow diagram shown in Figure 2.8. Furthermore, each step implemented in the algorithm is described below [25].

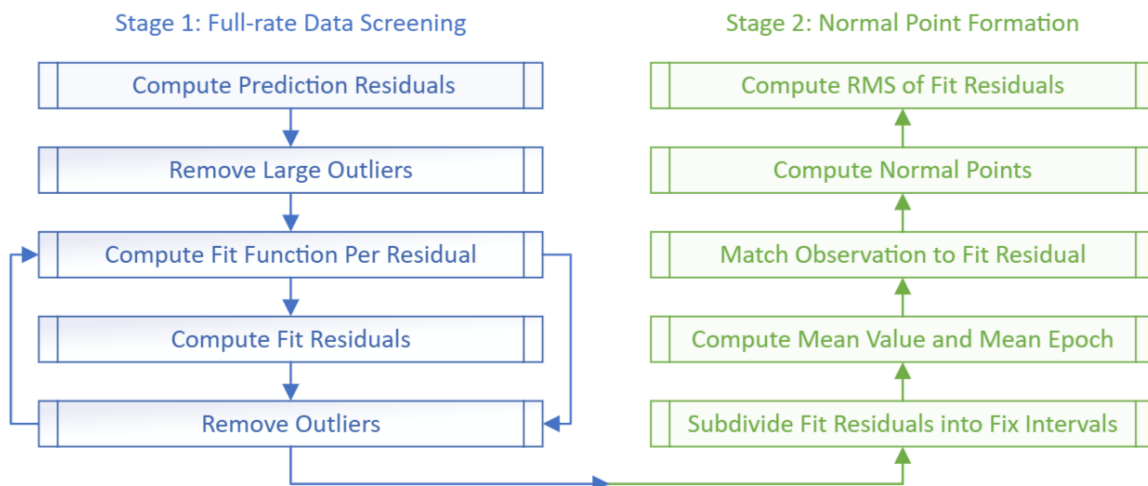


Figure 2.8: Flow diagram of the Herstmonceux algorithm

Stage 1: Full-rate Data Screening

1. Use high precision predictions to generate prediction residuals $PR = \text{observation} - \text{prediction}$. Both observation and prediction need to include all the correction factors of the range model;
2. Identify large outliers defining a suitable range window and remove them;
3. Solve for a set of parameters (preferably orbital) to remove the systematic trends of the prediction residuals. The resulting fitted function is the trend function f , with value $f(PR)$ at the epoch of the residual PR ;
4. Compute fit residuals $FR = PR - f(PR)$;
5. Remove outliers by computing the Root Mean Square (RMS) of the fit residuals and utilizing a rejection level of $n \times \text{RMS}$. The value of n is recommended to be taken as $n=2.5$ for systems using single photon detection and $n=3$ for systems using multi-photon detection.

Now iterate step 3, 4 and 5 until reaching convergence. The outliers removed in step 5 should not be considered in step 3 of next iteration. However, for step 4 and 5 of each iteration all data points should be utilized even the one removed in previous iterations.

Stage 2: Normal Point Formation

1. Take the accepted fit residuals, FR , and subdivide them into fixed intervals. These intervals are called bins and their size is specifically defined per satellite through recommendations provided by the ILRS;
2. Compute the mean value \overline{FR}_i and the mean epoch of the accepted fit residuals within each bin i ;
3. Match the particular observation O_i with its fit residual FR_i , whose observation epoch t_i is nearest to the mean epoch of the accepted fit residuals in bin i ;
4. Compute the normal point for each bin as: $NP_i = O_i - FR_i + \overline{FR}_i$;
5. Compute the RMS of the accepted fit residuals in each bin i from their mean value with $RMS_i = \sqrt{\frac{1}{n_i} \cdot \sum_i (FR_j - \overline{FR}_i)^2}$. Where n_i is the number of accepted fit residuals within bin i .

Further analysis of the data distribution can be performed by calculating the skewness and kurtosis parameters. These parameters are useful for describing some of the features of the data distribution. When computing these parameters, only the fit residuals that have been retained within the $n \times \text{RMS}$ screening in steps 3, 4, and 5 are considered.

If the data have insignificant skewness, then the mean value of the retained fit residuals will be located at the peak of the distribution of the data. Conversely, if the data are significantly skewed, then the mean will be offset from the peak, in the direction of the skewness. The difference of the mean from the peak is another useful indicator of the distribution of the data to characterize satellite signatures.

2.2.4. Precision of Normal Points

The precision of ToF measurements of an SLR station is given by the total variance of the system which is computed summing up the individual variances of the involved SLR segments, as shown in Equation 2.18.

$$\sigma_{Tot}^2 = \sigma_{Laser}^2 + \sigma_{Detector}^2 + \sigma_{Timer}^2 + \dots + \sigma_{Space}^2 \quad (2.18)$$

Therefore, to maximize precision of ToF measurements the total variance needs to be minimize. Following the aforementioned algorithm for the generation of normal points from full-rate data, an improved range precision can be achieved per normal point, ΔR_{NP} , as shown by Equation 2.19.

$$\Delta R_{NP} = \frac{\sigma_{Tot}}{\sqrt{n}} \quad (2.19)$$

Where n is the number of data points used to generate each normal point. This number could vary per normal point, nevertheless increasing the laser pulse frequency generating more data points leads to a faster desired normal point precision. Furthermore, the resulting normal point will represent a shorter orbital arc length obtaining a higher resolution orbit [27].

2.3. Retroreflectors Design

In this section, the design of the space segment is described with a focus on defining the required OCS of the retroreflector array to generate a strong enough returning pulse. Furthermore, various types of retroreflectors are investigated, along with the effect of radiation on their reflectivity.

2.3.1. The Link Budget Equation

To assess if the returning signal has enough strength to be collected by the ground station detector the mean signal flux in the receiver needs to be computed. The radar link equation is used to compute the mean number of photo-electrons, n_{pe} , reaching the ranging detector, as shown in Equation 2.20 [28].

$$n_{pe} = N_t \cdot G_T \cdot \sigma \cdot \left(\frac{1}{4 \cdot \pi \cdot R^2} \right)^2 \cdot A_r \cdot \eta_t \cdot \eta_r \cdot \eta_d \cdot T_a^2 \cdot T_c^2 \quad (2.20)$$

From this equation, it can be seen how the strength of the returning signal decreases by a factor of R^4 . Each of the variables in the radar link equation are individually investigated below.

- **Emitted photons of laser, N_t :** The number of emitted photons within the laser pulse is given by Equation 2.21.

$$N_t = \frac{E_p \cdot \lambda}{h \cdot c} \quad (2.21)$$

Where E_p is the pulse energy which is the average power divided by pulse length, λ is the laser wavelength, h is the Planck's constant, and c is the speed of light in vacuum.

- **Slant range, R :** The slant range to the target is the distance between the SLR ground segment and the target object in space. R is calculated utilizing the geometric coherence, as shown in Equation 2.22.

$$R = -(R_E + h_s) \cdot \cos\left(\frac{\pi}{2} - \alpha_e\right) + \sqrt{\left[(R_E + h_s) \cdot \cos\left(\frac{\pi}{2} - \alpha_e\right)\right]^2 + 2 \cdot R_E \cdot (h_{sat} - h_s) + h_{sat}^2 - h_s^2} \quad (2.22)$$

Where R_E is the Earth radius, h_s is the station altitude above sea level, h_{sat} is the satellite altitude above sea level, and α_e is the elevation angle.

- **Transmitter gain, G_T :** The transmitter gain, G_T , describes how well the laser energy is converted in a specific direction. Modern SLR systems produce a quasi-gaussian spatial and temporal laser profiles. Therefore, the formulation in Equation 2.23, applicable to Gaussian beams, can be used to calculate the transmitter gain.

$$G_T = \left(\frac{8}{\theta_d^2} \right) \cdot e^{-2 \cdot \left(\frac{\Delta\theta_p}{\theta_d} \right)^2} \quad (2.23)$$

Where θ_d represents the far-field beam divergence half-angle between the beam center and the $1/e^2$ intensity point. The exponential term denotes the static beam pointing loss, where $\Delta\theta_p$ represents the resulting beam pointing error from the center of the beam. However, it is essential to note that this expression does not account for the radial truncation of the beam Gaussian profile due to a limiting aperture, nor does it consider the central obscuration of the beam, possibly resulting from a secondary mirror in a Cassegrain telescope. These effects lead to a transfer of energy from the central lobe to the outer rings of the profile.

- **Telescope receive area, A_r :** To compute the effective receiver area, the radiation lost due to blockage of a secondary mirror, if any, and the spillover at the spatial filter, if any, and at the detector need to be taken into account. Equation 2.24 computes the receiver area including the aforementioned losses.

$$A_r = A_p \cdot (1 - \gamma^2) \cdot \eta_d \cdot \left(\gamma \cdot \frac{k \cdot R_d}{2 \cdot F} \right) \quad (2.24)$$

Where $A_p = \pi \cdot r_p^2$ is the area of the primary receiver, γ is the receiver obscuration ratio and $(1 - \gamma^2)$ is the fraction lost due to blockage of the secondary receiver. The term $\eta_d \cdot \left(\gamma \cdot \frac{k \cdot R_d}{2 \cdot F} \right)$ is

the fraction of light intercepted by a detector of radius R_d . Alternately, R_d could be the radius of a spatial filter in the focal plane of the receiver. F is the F-number of the receiving telescope and $k = 2\pi/\lambda$.

- **Satellite optical cross-section, σ :** The optical cross section of the satellite is the only variable related to the space segment which has an impact on the returning signal. Therefore, this term will be the driving factor for the design of the retroreflector array. An in depth analysis of σ is performed in the next section.
- **Transmitter optical throughput efficiency & receiver optical throughput efficiency, η_t, η_r :** The parameters η_t and η_r represent the total transmission efficiency of the transmitter and receiver optics, respectively. The total throughput optical efficiency, $\eta_{t,r}$, is the product of the transmission efficiencies of all elements η_i in the beam path, as shown in Equation 2.25.

$$\eta_{t,r} = \prod_i^n \eta_i \quad (2.25)$$

- **Quantum efficiency of detector, η_d :** The quantum efficiency refers to the effectiveness of a detector in converting an incident photon into an electron. This measure is expressed in probabilistic terms and depends on the type of detector implemented.
- **Two-way atmospheric attenuation factor, T_a^2 :** The attenuation of light in the visible and the infrared wavelength range occurs due to absorption and scattering caused by air molecules, solid, and liquid particles. The one-way atmospheric attenuation factor, $T_a(\lambda, V, h_r, \theta_{zen})$, is dependent on the laser wavelength, λ , the visibility, V , the relative height of the SLR ground station above sea level, h_r , and the zenith angle, θ_{zen} . The zenith angle is the complement of the elevation angle, α_e . The two-way attenuation factor is computed as the square of the one-way attenuation factor. The attenuation factor can be computed assuming the laser path to be a straight line ignoring the refractive bending. Figure 2.9 shows a plot displaying the one-way attenuation factor against laser wavelength at sea level and clear visibility $V = 60 \text{ km}$, at different zenith angles.

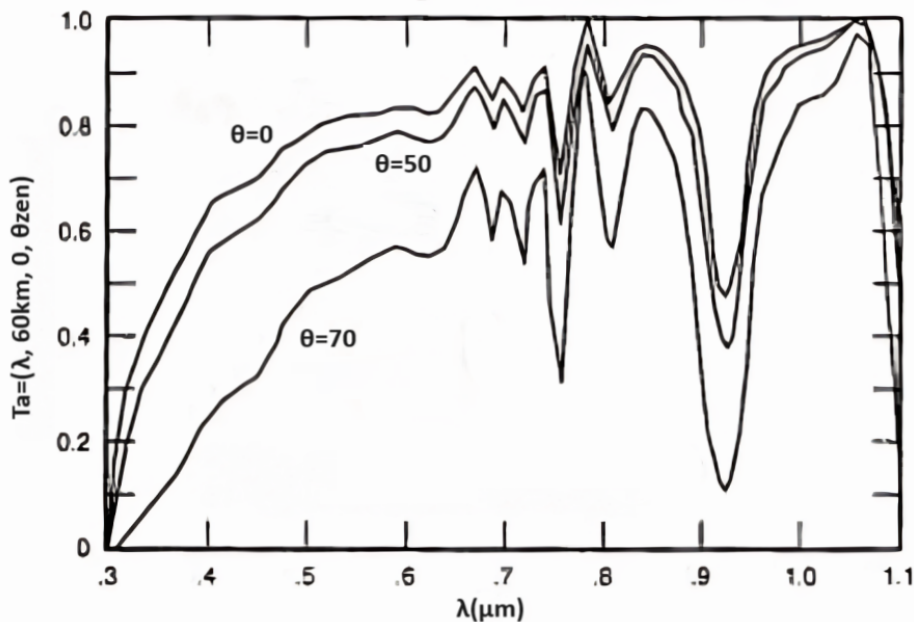


Figure 2.9: One-way attenuation factor against laser wavelength at sea level and clear visibility $V = 60 \text{ km}$ at $\theta_{zen} = 0^\circ, 50^\circ, 70^\circ$ [28].

- **Two-way cirrus cloud attenuation factor, T_c^2 :** Atmospheric losses arise from the presence of cirrus clouds, which are sub-visible clouds that are overhead 50% of the time in most locations, thereby attenuating the signal strength. For wavelengths between 0.3 and 12 μm , no significant

dependence has been found on the cirrus cloud attenuation factor. From experiments, it has been determined that the one-way cirrus cloud attenuation factor, T_c , can be computed using Equation 2.26.

$$T_c = e^{-0.14 \cdot (t \cdot \sec(\theta_{zen}))^2} \quad (2.26)$$

Where t is the cirrus cloud thickness. From a global study on cirrus clouds thickness, it has been found that the average cirrus clouds thickness is 1.341 km [29].

With the aforementioned variables, it is possible to solve the radar link equation to obtain the mean number of photo-electrons reaching the SLR detector. This number significantly varies with respect to weather conditions. For instance, considering the worst and best case scenarios for laser ranging of LAGEOS using MOBILAS-6, the maximum number of received photo-electrons could vary between 612 and 0.05 per pulse due to variations in weather conditions, as well as changes in orbital and hardware settings [28]. Therefore, unless there are other compelling reasons, an SLR station with minimal cloud cover and high atmospheric transparency will result in more detected data and higher accuracy than any other station.

2.3.2. Required Mean Number of Returning Photo-electrons

The required mean number of returning photo-electrons, n_{pe} , to achieve ranging measurements is determined by the detector settings, specifically by defining the threshold for the minimum number of photo-electrons, n_t , needed for signal detection. This threshold helps decrease the probability of detecting a signal when no signal is present, also known as the probability of false alarm. False alarms are a consequence of background noise entering the detector FoV. Therefore, it is important to set a threshold high enough to minimize their occurrence. Furthermore, n_{pe} is also related to the probability of detection, which is the detector capability to convert an arriving photon into an electric impulse.

To retrieve the required n_{pe} , it is essential to first define the background photo-electron rate, Λ , as described by Equation 2.27 [27].

$$\Lambda = \frac{\eta_d}{h \cdot v} \cdot N_l \cdot \Omega_r \cdot A_r \cdot \eta_r \quad (2.27)$$

Where N_l is the background spectral radiance, Ω_r is the receiver FoV in steradians, and v is the laser frequency. The background spectral radiance, N_l , is computed for both daylight and nighttime, depending on when ranging measurements are performed. Usually, due to the high background photo-electron rate during daylight, ranging measurements are performed at night.

During daylight, the solar spectral irradiance, I_λ , can be retrieved from Figure 2.10 for specific wavelength ranges passing through the narrow band-pass filter. It is appropriate to consider the wavelength of the emitted laser pulse. The most important parameter that determines the solar irradiance under clear sky conditions is the distance that sunlight has to travel through the atmosphere. This distance is shortest when the sun is at the zenith. The ratio of the actual path length of sunlight to this minimal distance is known as the optical air mass (AM). The value retrieved from the graph is for an optical air mass of 1.5, which corresponds to an angle of 48.2 degrees between the Sun position and the zenith, and it is currently considered the standard spectral distribution [30].

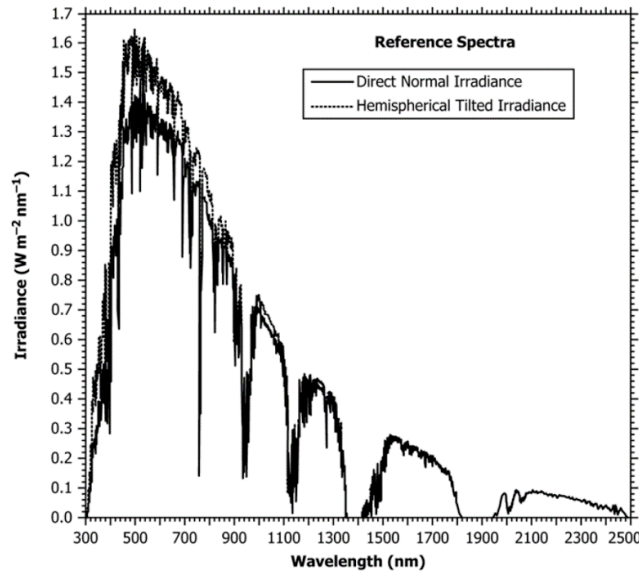


Figure 2.10: Plot of Direct Normal Spectral Irradiance, and Hemispherical Spectral Irradiance [31].

Once the solar spectral irradiance is retrieved, it needs to be translated to ground-level where the receiver is placed. Therefore, the atmospheric transmission, T_λ , of the selected wavelength needs to be considered. The atmospheric transmittance at different wavelengths can be retrieved from Figure 2.11.

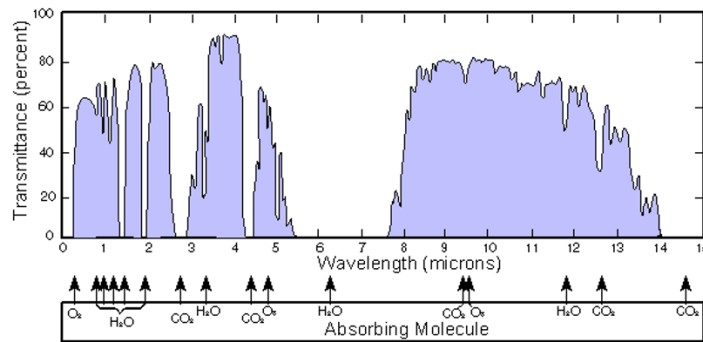


Figure 2.11: Atmospheric transmittance per wavelength [32].

Consequently, the ground-level spectral irradiance can be converted into background daylight spectral radiance by considering a half-sphere portion of the sky, from which the detector sees only a portion. The transformation from spectral solar irradiance to background spectral radiance is summarized in Equation 2.28.

$$N_l = \frac{I_\lambda \cdot T_\lambda}{2 \cdot \pi} \tag{2.28}$$

During nighttime, the major sources of background noise are the scattering of sunlight reflected by the Moon through the atmosphere and light pollution from nearby city centers or rural areas with a high number of greenhouses. In the Netherlands, multiple sensors have been placed throughout the country to collect data on sky brightness, B , at night [33]. Specifically, in Delft, a sensor was placed on top of the Aerospace faculty building next to the newly built laser communication station. It is important to acknowledge that Delft is surrounded by numerous greenhouses, which makes it one of the most light-polluted regions in the Netherlands [34]. Figure 2.12 shows the data of sky brightness collected by Delft sensor during its first night of operation.

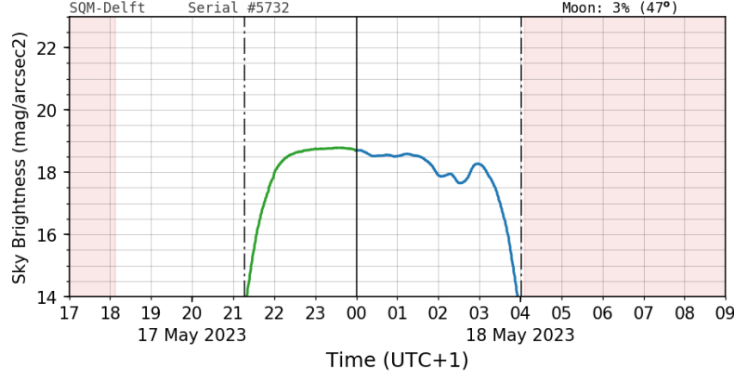


Figure 2.12: Sky brightness measurements during the night of the 17th of May 2023 [33].

Furthermore, Table 2.3 displays the average, 10% percentile, 50% percentile, and the maximum values of sky brightness collected in Delft since the first day of operation.

Table 2.3: Average, 10% percentile, 50% percentile, and the maximum value of sky brightness collected in Delft since May 2023 [33].

Average	10% Percentile	50% Percentile	Maximum
18.0626 mag/arcsec ²	18.028 mag/arcsec ²	15.480 mag/arcsec ²	18.116 mag/arcsec ²

Taking the average as a reference value, the sky brightness scale needs to be converted into background spectral irradiance. The first step is to transform $mag/arcsec^2$ into cd/m^2 [35], and then transform it into spectral irradiance as shown in Equation 2.29 [36].

$$B_{cd/m^2} = 10.8 \cdot 10^4 \cdot 10^{-0.4 \cdot B} \quad (2.29)$$

$$N_l = B_{cd/m^2} \cdot 1.464 \cdot 10^{-7} \text{ at } 555 \text{ nm}$$

With the background spectral irradiance, N_l , it is possible to compute the background photo-electron rate, Λ , as described before in Equation 2.27. Consequently, the number of background photons entering the detector needs to be determined. The detector has two different time settings to collect the returning signal. The range gate time window, τ_{rg} , represents the period during which the detector is actively collecting photons. To define a proper range gate, the initial and ending times need to be set based on the accuracy of the orbit prediction model. This ensures that the detector is sensitive only when the returning signal is expected. As reference, $1 \mu s$ is considered as range gate, which requires an orbit prediction model accuracy of ± 150 m. Using Equation 2.30, the photon count entering the detector within the range gate window can be computed.

$$N_{b_{rg}} = \Lambda \cdot \tau_{rg} \quad (2.30)$$

The second time setting is the integration time, τ_i , which represents the period during which the detector sums up the received photons. To collect the entire returning signal, the integration time should be set equal to the length of the returning pulse. Using Equation 2.31, the photon count entering the detector within the integration window can be computed.

$$N_{b_i} = \Lambda \cdot \tau_i \quad (2.31)$$

With these two photon counts, the probability of false alarm, P_{fa} , can be computed using Equation 2.32. Defining a limit value for the probability of false alarm allows the computation of the minimum number of photo-electrons threshold, n_t .

$$P_{fa} = 1 - \exp \left(\frac{-N_{b_{rg}} \cdot N_{b_i}^{n_t-1}}{(n_t-1)!} \right) \quad (2.32)$$

$$P_{fa} = 1 - \exp \left(\frac{\sum_{m=0}^{n_t-1} \frac{N_{b_i}^m}{m!}}{N_{b_i}^{n_t-1}} \right)$$

Considering the receiving signal as the sum of the mean number of returning photo-electrons and the background noise photons, as given by Equation 2.33, the probability of detection, P_d , can be computed approximating it with a Poisson distribution, as shown in Equation 2.34 [28].

$$N = n_{pe} + n_{br} \quad (2.33)$$

$$P_d = 1 - e^{-N} \cdot \sum_{m=0}^{n_t-1} \frac{N^m}{m!} \quad (2.34)$$

By setting a lower limit for P_d , the required mean number of returning photo-electrons, n_{pe} , can be determined.

2.3.3. Optical Cross Section

The OCS of a retroreflector, denoted as σ , when oriented normal to the incident light and in the far-field limit ($r_{cc}/R \rightarrow 0$), can be computed using Equation 2.35 [27]. In this case, the Far-Field Diffraction Pattern (FFDP) of the reflected wave is the Airy function.

$$\sigma = \rho \cdot \frac{4 \cdot \pi \cdot A_{cc}^2}{\lambda^2} \cdot \left[\frac{2 \cdot J_1(k \cdot r_{cc} \cdot \sin(\theta_r))}{k \cdot r_{cc} \cdot \sin(\theta_r)} \right]^2 \quad (2.35)$$

In this equation, θ_r represents the returning signal orientation error, ρ is the retroreflector reflectivity, k is the propagation number ($2\pi/\lambda$), and $A_{cc} = \pi r_{cc}^2$ denotes the area of the retroreflector circular aperture with radius r_{cc} . The function J_1 is a Bessel function of the first kind. Bessel functions are part of the set of solutions for Bessel's differential equation and can be expressed generally as shown in Equation 2.36.

$$J_n(x) = \sum_{k=0}^{\infty} \frac{(-1)^k}{k! \cdot \Gamma(n+k+1)} \cdot \left(\frac{x}{2}\right)^{n+2k} \quad (2.36)$$

Where $\Gamma(n) = (n-1)!$, and n represents the order of the Bessel function.

For normally incident light, the peak on-axis OCS of an unspoiled, $\theta_r = 0$, retroreflector is given by Equation 2.37.

$$\sigma_{\theta_r=0} = \rho \cdot A_{cc} \cdot \frac{4 \cdot \pi}{\Omega} = \rho \cdot \frac{4 \cdot \pi \cdot A_{cc}^2}{\lambda^2} = \frac{\pi^3 \cdot \rho \cdot D_{cc}^4}{4 \cdot \lambda^2} \quad (2.37)$$

Where, $4\pi/\Omega$ is the on-axis gain and Ω is the effective solid angle occupied by the FFDP of the retroreflector. However, when the retroreflector is not oriented normal to the incident light, an incident angle is created, θ_i , which decreases the actual area of the circular aperture of the retroreflector, A_{cc} . The decreasing factor, η , is given by Equation 2.38.

$$\eta(\theta_i) = \frac{2}{\pi} \cdot \left[\sin^{-1}(\mu) - \left(\frac{l}{r_{cc}}\right) \cdot \mu \cdot \tan(\theta_{ref}) \right] \cdot \cos(\theta_i) \quad (2.38)$$

Where θ_i is the incidence angle and l/r_{cc} is the corner-cube ratio which is set to its limit value of $\sqrt{2}$. θ_{ref} is the internal refracted angle as determined in Equation 2.39 by Snell's Law.

$$\theta_{ref} = \sin^{-1} \left(\frac{\sin(\theta_i)}{n} \right) \quad (2.39)$$

Here n is the cube index of refraction.

The quantity μ in the decreasing factor equation can be computed with Equation 2.40.

$$\mu = \sqrt{1 - \left(\frac{l}{r_{cc}}\right)^2 \cdot \tan^2(\theta_{ref})} \quad (2.40)$$

Thus, the peak OCS of a single retroreflector not oriented normal to the incident light falls off as described in Equation 2.41.

$$\sigma_{eff} = \eta^2 \cdot \sigma \quad (2.41)$$

And, if the single reflector is unspoiled, its effective peak OCS can be calculated with Equation 2.42

$$\sigma_{eff_{\theta_r=0}} = \rho \cdot \frac{4 \cdot \pi \cdot [A_{cc} \cdot \eta]^2}{\lambda^2} \quad (2.42)$$

While, if velocity aberration is considered, inducing an off-axis reflection, its effective OCS can be calculated with Equation 2.43.

$$\sigma_{eff} = \rho \cdot \frac{4 \cdot \pi \cdot (A_{cc} \cdot \eta)^2}{\lambda^2} \cdot \left[\frac{2 \cdot J_1(k \cdot r_{cc} \cdot \eta \cdot \sin(\theta_r))}{k \cdot r_{cc} \cdot \eta \cdot \sin(\theta_r)} \right]^2 \quad (2.43)$$

2.3.4. Velocity Aberration

The retroreflectors are built following the principle of reflecting light in the same direction as the incoming beam, provided no spoiling is applied. Therefore, the beam reflected by a satellite should ideally reach the ground station with no deviation. However, in reality, this is not the case due to the relative velocity, v , between the satellite and the ground station. As a consequence, the direction of the reflected beam is angularly shifted towards the relative velocity vector by an amount α [37]. This effect is known as velocity aberration and can result in significant losses in the signal. Figure 2.13 illustrates a schematic of the principle of velocity aberration.

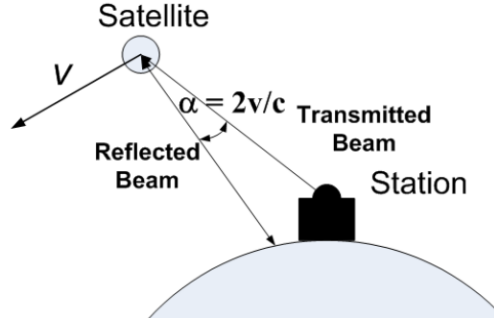


Figure 2.13: Schematic of velocity aberration [37].

To calculate the magnitude of the angular displacement in the FFDP, α , due to velocity aberration, Equation 2.44 can be used.

$$\alpha = \alpha_{max} \cdot \sqrt{\cos^2(\omega) + \Gamma^2 \cdot \sin^2(\omega)} \quad (2.44)$$

Where Γ is given by Equation 2.45 and ω by Equation 2.46.

$$\Gamma = \sqrt{1 - \left(\frac{R_e \cdot \sin(\theta_{zen})}{R_e + h_s} \right)^2} \quad (2.45)$$

$$\omega = \cos^{-1}[(\hat{r} \times \hat{p}) \cdot \hat{v}] \quad (2.46)$$

Here, \hat{r} is the unit vector to the satellite from the geocenter, \hat{p} is the unit vector from the station to the satellite, and \hat{v} is the unit vector in the direction of satellite velocity.

The maximum value of the angular shift, α_{max} , can be computed with Equation 2.47.

$$\alpha_{max} = \frac{2 \cdot v_s}{c} = \frac{2}{c} \cdot \sqrt{\frac{g \cdot R_e^2}{R_e + h_s}} \quad (2.47)$$

While, the minimum value of the angular shift, α_{min} , can be calculated using Equation 2.48, and it depends on the maximum zenith angle for tracking, $\theta_{zen_{max}}$.

$$\alpha_{min} = \alpha_{max} \cdot \Gamma(h_s, \theta_{zen_{max}}) \quad (2.48)$$

The latter equations ignore the small contribution of station motion due to Earth rotation, $\sim 0.46 \text{ km/s}$, to the relative velocity which typically reduces α by 4 or 5 μrad for LLR but is negligible for LEO to GEO satellites [37].

To compensate for velocity aberration, several techniques are available, with the most common being the spoiling of retroreflectors. This technique involves inducing an angular shift, γ , in the reflected signal, θ_r , which is equal in magnitude but opposite in direction to the angular shift caused by velocity aberration, α . Achieving this compensation requires aligning the attitude of the reflector with the direction of motion. To achieve spoiling, the faces within the retroreflector are connected at slightly perturbed angles instead of the usual right-angle configuration. The angle perturbation is known as the dihedral angle, δ , and can be applied to one or all faces, $n_\delta = 1 \text{ or } 3$.

The induced shift in the reflected signal can be computed with Equation 2.49 [38].

$$\gamma = \begin{cases} \frac{4}{3} \cdot \sqrt{6} \cdot \delta & \text{for } n_\delta = 3 \\ \frac{2}{3} \cdot \sqrt{6} \cdot \delta & \text{for } n_\delta = 1 \end{cases} \quad (2.49)$$

This results in a shifted velocity aberration, α_s , as shown in Equation 2.50, which is used in Equation 2.43 as the returning signal orientation error, θ_r .

$$\alpha_s = \alpha - \gamma \quad (2.50)$$

Nevertheless, spoiling the retroreflector reduces the on-axis peak OCS, $\sigma_{\theta_r=0}$, as described by Equation 2.51.

$$\sigma_{eff} = \frac{\sigma_{\theta_r=0}}{(2 \cdot n_\delta)^2} \quad (2.51)$$

Another technique involves decreasing the diameter, D , hence, the retroreflector aperture. This action results in an increase in the FFDP angle, θ , leading to a broadening of the diffraction pattern, as illustrated by Equation 2.52.

$$\theta = \frac{3.8 \cdot \lambda}{\pi \cdot D} \quad (2.52)$$

However, while this adjustment places the OCS above the threshold level within the velocity aberration range if $\alpha < \theta$. It decreases it in other regions, thereby limiting the range of acceptable tilt angles and imposing higher constraints on the attitude control of the satellite [39].

Another way of compensating for velocity aberration consists in broadening the diffraction pattern by tilting the retroreflector away from the station in the direction of the relative velocity vector to achieve a narrower effective aperture in the direction of the velocity aberration. In fact, tilting the retroreflector, will lead to an effective decrease of the retroreflector aperture, D , by η , the factor introduced in Equation 2.38. Consequently broadening the diffraction pattern as described in Equation 2.52, with the drawback of decreasing the overall OCS response.

2.3.5. Retroreflector Types

Generally, there are three type of retroreflectors: corner retroreflectors, cat eye reflectors, and non-linear retroreflectors. The retroreflector that is most commonly implemented in space is the corner retroreflector in the form of corner cube prisms, where reflections occur on three mutually orthogonal mirror surfaces. The corner cube retroreflectors can either be solid back-coated, solid uncoated, or hollow. Each configuration has its own advantages and disadvantages which are displayed in Table 2.4.

Table 2.4: Characteristics of three different type of CCRs [37]

	Solid Back-Coated	Solid Uncoated	Hollow
Reflectivity	0.78	0.93	0.99
Polarization Sensitive	No	Yes	No with metal coatings. Yes with dielectric coatings
Far Field Pattern	Wide	Wide	Narrow
Weight	Heavy	Heavy	Light
Issue	Metal coatings absorb sunlight creating thermal gradients. Not well shielded, susceptible to radiation effects.	Leak of signal at incident angle higher than 17° . Polarization effect can decrease optical cross section by a factor of 4.	Thermal heating and gradient effects on joints

For the design of the array to be placed on top of the new TU Delft platforms, the solid back-coated retroreflector type will be utilized. This decision is influenced by the fact that the uncoated type exhibits leakage starting from 17° of incident angle, thereby limiting the array configuration and imposing stringent requirements on the attitude control of the satellite. Furthermore, back-coated types are the most commonly used within the space industry, offering high accessibility of Commercial Off-The-Shelf (COTS) components. While, the hollow retroreflectors have never been implemented for visible wavelengths.

For the array of the new TU Delft platforms, the specular retroreflector prisms with backside gold coating from Thorlabs [14], and the aluminum coated fused silica corner cubes from Edmund Optics are considered [40]. The Thorlabs retroreflectors are made of N-BK7, and are available in different diameters, namely 12.7 mm, 25.4 mm, and 50 mm. While the Edmund retroreflectors are made of fused silica and are available with diameters of 7.16 mm, 12.7 mm, 25.4 mm, and 50.8 mm. The diameter of the retroreflector will be a design consideration during the design of the array. In Table 2.5 and Table 2.6, the available specifications of the two type of retroreflectors are displayed.

Table 2.5: Main specifications of the specular retroreflector prisms with backside gold coating from Thorlabs [14].

Parameter	Value
Prism material	N-BK7
Wavelength range	800 – 2000 nm
Reflective coating	Gold with black over-paint
Diameter tolerance	± 0.1 mm
Surface quality	40 – 20 Scratch-dig
Beam deviation	$< 3''$
Damage threshold	1.25 J/cm ²
Index of refraction	1.517 at 587.6 nm

Table 2.6: Main specifications of the aluminum coated fused silica corner cubes from Edmund Optics [40].

Parameter	Value
Prism material	Fused Silica
Wavelength range	400 – 2000 nm
Reflective coating	Aluminum
Diameter tolerance	± 0.1 mm
Surface quality	20 – 10 Scratch-dig
Beam deviation	$< 5''$
Damage threshold	0.3 J/cm ²
Index of refraction	1.45 at 587.6 nm

2.3.6. Radiation Effect

When orbiting in space, satellites and all their components are subject to radiation. Particularly noteworthy is the impact of radiation, such as gamma rays, on the optical components of a satellite, which can result in a decrease in performances or, in some cases, in mission failure. For instance, in the context of the retroreflector of Thorlabs introduced in the previous section, N-BK7, the material of which the prism is made, is susceptible to radiation, leading to a reduction in its reflectivity and consequently

diminishing the intensity of the reflected beam. A study conducted by T.L. Griffiths et al. [41] examined how the intensity of a laser beam passing through different lenses made of BK7, as well as coated and uncoated fused silica, changed due to gamma ray radiation. Figure 2.14 and Figure 2.15 illustrate the variation in intensity at various levels of radiation exposure across different wavelengths for BK7 glass and uncoated UV-grade fused silica (UVFS) respectively.

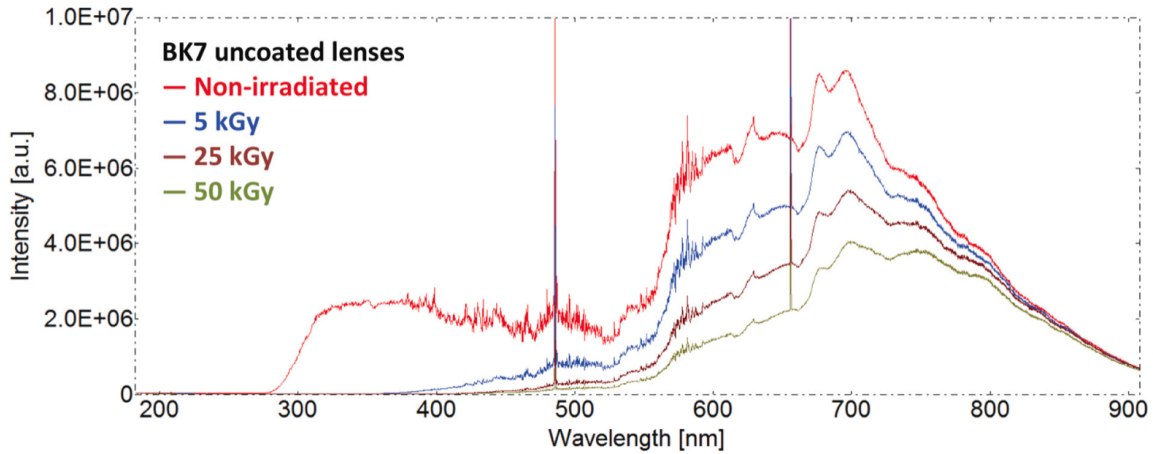


Figure 2.14: Spectral output of the deuterium-halogen lamp when transmitted via unirradiated, 5 kGy, 25 kGy and 50 kGy irradiated BK7 glass collection optics [41].

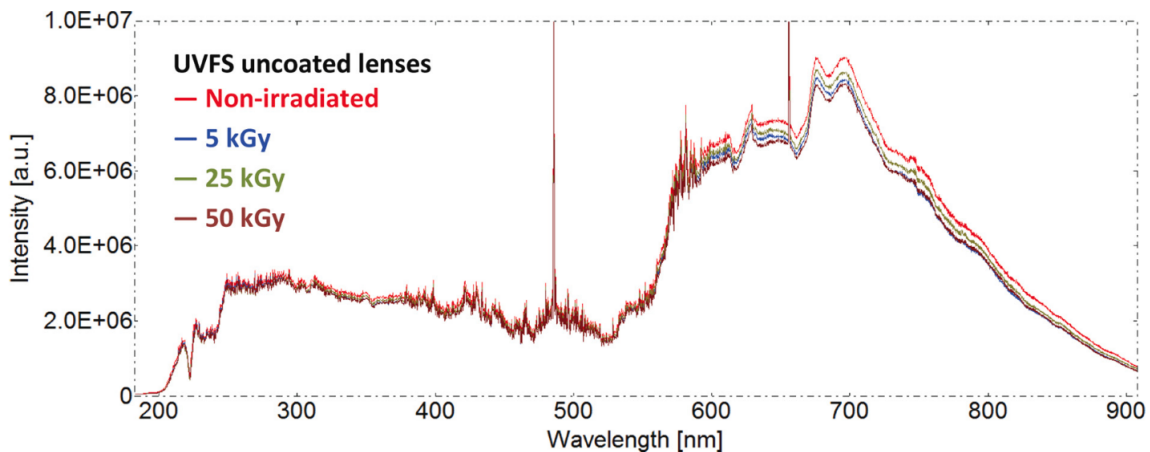


Figure 2.15: Spectral output of the deuterium-halogen lamp when transmitted via unirradiated, 5 kGy, 25 kGy and 50 kGy irradiated UV-grade fused silica (UVFS) glass collection optics. [41].

From the BK7 graph, it can be observed that the visible range of wavelengths is severely affected already at the first level of radiation. However, for higher laser wavelengths, the effect on the laser intensity is negligible. Therefore, implementing a 1064 nm laser is preferable over a classic laser in the visible range when implementing retroreflector prisms made of N-BK7. However, most of the ILRS stations do not implement a 1064 nm laser therefore limiting the number of stations with which ranging measurements can be gathered. Regarding fused silica lenses, the effect of gamma ray radiation is much less significant as observed in Figure 2.15. Furthermore, to put this into perspective, the ionizing radiation expected on the retroreflector of Delfi-Twin is estimated using Spenvis, ESA's Space Environment Information System [42]. The orbital parameters are input into the tool, and the ionizing dose for simple geometries is simulated with the SHIELDDOSE-2 model, assuming SiO₂ as the target material. With the absorber thickness set to the smallest simulated value, a total mission dose of $1.396 \cdot 10^6$ rad, equivalent to 13.96 kGy, is obtained. Consequently, implementing N-BK7 as the material

would lead to a significant reduction in performance over the mission duration. This would suggest a preference for implementing retroreflectors with a fused silica prism like the one from Edmund Optics. However, fused silica components are extremely expensive and scarce on the market. Manufacturers typically produce limited batches over the span of years. Nevertheless, for the implementation on the new TU Delft platforms it would be preferable to implement the retroreflectors from Edmund Optics rather than the one from Thorlabs.

2.4. Ground Station

This section presents the main specifications of four possible SLR stations with which the retroreflector array will be designed to operate. The first station is the Mini-SLR optical system developed by DLR in Stuttgart, the second and third one are station 7941 in Matera, and station 14473 in Potsdam, which are part of the ILRS network. Lastly, the new TU Delft laser satellite communication station is included. Although this station is primarily intended for laser communication, it could also be utilized for ranging measurements. Table 2.7, Table 2.8, Table 2.9, and Table 2.10 respectively list the main specifications of the Mini-SLR, the new TU Delft laser communication station, Potsdam station, and Matera station.

Table 2.7: Main specifications of the Mini-SLR optical system.

Parameter	Symbol	Value
Transmit aperture	D_t	7.5 cm
Beam diameter	D_{beam}	5 cm
Receiver aperture	D_r	20 cm
Obscuration	γ	25%
Laser pulse energy	E_p	85 μJ
Laser repetition rate	f_{laser}	50 kHz
Laser pulse width	t_s	4 ns
Operating wavelength	λ	1064 nm
Half-angle beam div.	θ_d	50 μrad
Beam stability	$\Delta\theta_p$	25 μrad
Transmitter efficiency	η_t	0.6
Receiver efficiency	η_r	0.1
Efficiency of detector	η_d	30%

Table 2.8: Main specifications of TU Delft lasercom station.

Parameter	Symbol	Value
Transmit aperture	D_t	40.5 cm
Beam diameter	D_{beam}	10 cm
Receiver aperture	D_r	40.5 cm
Obscuration	γ	44%
Laser Power	P_{laser}	0.5 W
Laser repetition rate	f_{laser}	N/A
Laser pulse width	t_s	TBD
Operating wavelength	λ	1560 nm
Half-angle beam div.	θ_d	9.93 μrad
Beam stability	$\Delta\theta_p$	10 μrad
Transmitter efficiency	η_t	0.7*
Receiver efficiency	η_r	0.7*
Efficiency of detector	η_d	80%*

*Variables with assumed values.

Table 2.9: Main specifications of station 14473 in Potsdam of the ILRS network [43].

Parameter	Symbol	Value
Transmit aperture	D_t	15 cm
Beam diameter	D_{beam}	15 cm
Receiver aperture	D_r	44 cm
Obscuration	γ	0.34
Laser pulse energy	E_p	10 mJ
Laser repetition rate	f_{laser}	10 Hz
Laser pulse width	t_s	50 ps
Operating wavelength	λ	532 nm
Full-width beam div.	θ_d	25 μrad
Beam stability	$\Delta\theta_p$	0.41 μrad
Transmitter efficiency	η_t	0.8
Receiver efficiency	η_r	0.4
Efficiency of detector	η_d	8%

Table 2.10: Main specifications of station 7941 in Matera of the ILRS network [44].

Parameter	Symbol	Value
Transmit aperture	D_t	1.5 m
Beam diameter	D_{beam}	0.01 m
Receiver aperture	D_r	1.5 m
Obscuration	γ	N/A
Laser pulse energy	E_p	200 mJ
Laser repetition rate	f_{laser}	10 Hz
Laser pulse width	t_s	50 ps
Operating wavelength	λ	1064 nm
Full-width beam div.	θ_d	218 μrad
Beam stability	$\Delta\theta_p$	0.41 μrad
Transmitter efficiency	η_t	0.75
Receiver efficiency	η_r	0.87
Efficiency of detector	η_d	13%

Since the new TU Delft laser communication station is still in development phase, some parameters are currently unknown. Therefore, assumptions are made: the transmitter and receiver efficiencies are taken to be 0.7 [45], and the implemented detector is assumed to be an InGaAs photoreceiver with

80% quantum efficiency. The laser power of the available Exail laser is 0.5 W . Furthermore, since this ground station is primarily built for laser communication, the laser is continuous. However, if On-Off Keying (OOK) modulation is assumed to be implemented a duration of each pulse in the OOK modulation can be retrieved leading to a repetition rate. Knowing the repetition rate makes it possible to compute the energy per pulse dividing the laser power by the laser length.

2.5. TU Delft Satellite Platforms

Under the Delfi program started in 2004, the Technical University of Delft entered the field of CubeSats and became one of the first to demonstrate their benefits within the professional space sector with the launch of Delfi-C3 in 2008. In the following years, the number of universities and other institutes developing CubeSats increased rapidly, and TU Delft launched a second CubeSat, Delfi-n3XT, in 2013. With these satellites, TU Delft aims to provide a real-life platform for students to understand the dynamics behind a space project, as well as to perform demonstrations of small innovative space technology, thus boosting small satellite bus development. In fact, in recent years, TU Delft has been refocusing on miniaturization of satellites, launching Delfi-PQ, a triple-unit PocketQube, in 2022. The mini-satellite was fully produced by the Delfi team, from circuit boards to micro-propulsion systems, as COTS components were too large to fit in the small bus of the satellite. Figure 2.16, Figure 2.17, Figure 2.18 display the entire TU Delft satellite legacy starting with Delfi-C3, then Delfi-n3xt, and Delfi-PQ.



Figure 2.16: Delfi-C3.



Figure 2.17: Delfi-n3XT.



Figure 2.18: Delfi-PQ.

The next satellite platform of TU Delft, Delfi-Twin, will be built on top of the Delfi-PQ design, maintaining its same size $5 \times 5 \times 18\text{ cm}$ and its orbit altitude of 525 km implementing new state-of-the-art PocketQube technologies. TU Delft aims to utilize this new platform to perform laser ranging measurements by implementing an array of retroreflectors on top of the satellite, coupled with a laser communication station under construction on top of the Aerospace faculty building. In order to design the retroreflector array, it is important to understand how the attitude determination and control system of the satellite will be designed. The plan is to implement a completely passive control system consisting of two extendable flaps positioned at one end of the satellite, which will provide stability utilizing the principle implemented on a shuttlecock. Nevertheless, this system will constrain the yawing and pitching rotation axes, it will not stop the satellite from rolling. This insight is of primary concern for the design of the retroreflector array, as a smart design will need to be implemented to achieve full coverage even if the satellite is rolling.

Another platform is currently being developed at TU Delft by the Da Vinci Satellite project, an initiative led by a non-profit student team from Delft University of Technology. This team is participating in the ESA program "Fly Your Satellite." In this case, the satellite follows a CubeSat format, with its attitude designed to remain fixed, ensuring that the bottom face consistently points towards Nadir.

Another important limitation factor for the design of the retroreflector array is the launch case which will be utilized during the launch of the satellite. The casing for Delfi-Twin is a standardized case suggested by ESA, which consists of a 3P casing where the satellite is locked inside through rails present at all four corners of the cube. Thus, this case limits the amount of space the array could take on the outside of the main body of the satellite. Figure 2.19 shows the 3P casing configuration and its dimensions in

mm, while Figure 2.20 displays the protrusion allowances on each side of the PocketQube within the case. From the drawings, the following ESA requirements are set [46]:

- **SYS-PHY-06:** Components and parts may be installed on the +X, -X, +Y, +Z, -Z surfaces of the baseline PocketQube configuration, provided that they do not protrude more than 7 mm from the main body baseline envelope, and are separated more than 3.4 mm from the +Y surface of the sliding plate.
- **SYS-PHY-07:** Components and parts may be installed on the -Y surface of the baseline PocketQube configuration, provided that they do not protrude more than 7 mm from the baseline envelope, and are separated more than 3 mm from the +X, -X, +Z, -Z edges of the sliding plate.

The case to be implemented by the Da Vinci satellite is also recommended by ESA. From the documentation of the "Fly Your Satellite" program, the following requirement is retrieved [47]:

- **CDS-2.2.5:** Rails shall have a minimum width of 8.5mm measured from the edge of the rail to the first protrusion on each face.

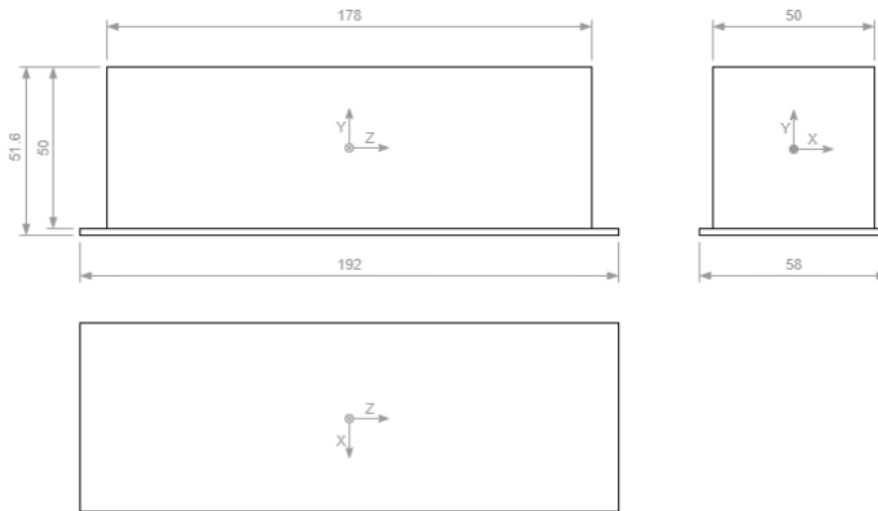


Figure 2.19: 3P PocketQube case baseline configuration [46].

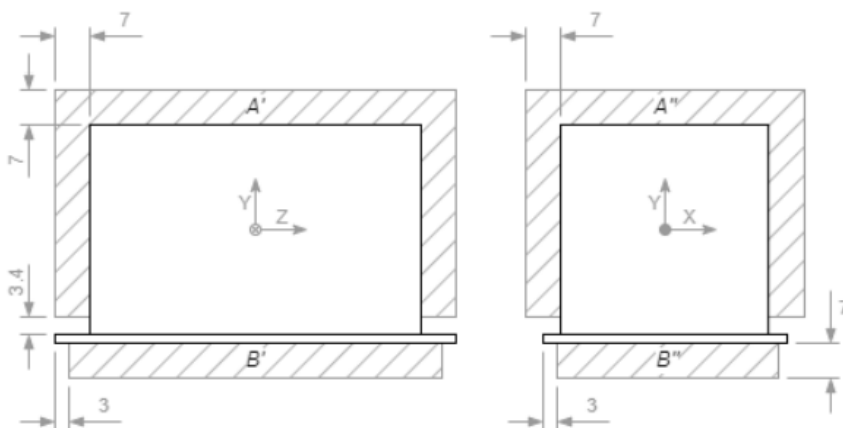


Figure 2.20: PocketQube protrusions envelope allowance [46].

3

Methodology

This chapter outlines the methodology used to conduct the simulations and tests throughout this thesis. It provides the framework that integrates the rationale behind the simulations with the underlying requirements in relation to the research questions and objectives. The high-level overview of the thesis, its building blocks, key steps, and methods employed are discussed.

Firstly, in section 3.1 the top-level requirements set for the design of the system are listed and a rationale behind each requirement is provided. Secondly, in section 3.2, the methodical approach implemented in the thesis to answer the research objectives is discussed describing the main steps.

3.1. Requirements

In this section, the top-level requirements of the analyzed system are listed. These serve as a baseline for the simulations performed during the thesis.

- **REQ-SYS-1:** The retroreflector array shall fit on the new TU Delft platforms.
Rationale: The thesis aims to design a retroreflector array to be integrated on the new TU Delft platforms, as defined by RO-1 and RO-2.
Verification: Inspection, analysis.
 - **REQ-SYS-1.1:** The retroreflector array shall fit on Delfi-Twin.
Rationale: The new satellite being developed by the Department of Space Engineering (DSE) requires the implementation of an array of retroreflectors to achieve ranging measurements.
Verification: Inspection, analysis.
 - * **REQ-SYS-1.1.1:** The retroreflector array shall consist of a maximum of 8 retroreflectors.
Rationale: Due to budget and size constraints, the DSE set a limit on the maximum number of retroreflectors within the array.
Verification: Inspection, analysis.
 - * **REQ-SYS-1.1.2:** Components and parts may be installed on the +X, -X, +Y, +Z, -Z surfaces of the baseline PocketQube configuration, provided that they do not protrude more than 7 mm from the main body baseline envelope, and are separated more than 3.4 mm from the +Y surface of the sliding plate.
Rationale: This requirement comes from the ESA PocketCube recommendations for the use of the PocketCube launch case, as shown in Figure 2.20.
Verification: Inspection, analysis.
 - * **REQ-SYS-1.1.3:** Components and parts may be installed on the -Y surface of the baseline PocketQube configuration, provided that they do not protrude more than 7 mm from the baseline envelope, and are separated more than 3 mm from the +X, -X, +Z, -Z edges of the sliding plate.
Rationale: This requirement comes from the ESA PocketCube recommendations for the

use of the PocketCube launch case, as shown in Figure 2.20.

Verification: Inspection, analysis.

- * **REQ-SYS-1.1.4:** The retroreflector array shall accommodate a satellite rolling rate not higher than 10 deg/s.
Rationale: Delfi-PQ had an attitude control system that allowed the satellite to freely roll. The maximum recorded rolling rate of Delfi-PQ was 10 deg/s, and the same is expected for Delfi-Twin. Therefore, the retroreflector array is sized using an upper boundary for the rolling rate of 10 deg/s.
 Verification: Test, analysis.
- * **REQ-SYS-1.1.5:** The retroreflector array shall accommodate a satellite rolling rate not lower than 5 deg/s.
Rationale: Delfi-PQ had an attitude control system that allowed the satellite to freely roll. The minimum recorded rolling rate of Delfi-PQ was 5 deg/s, and the same is expected for Delfi-Twin. Therefore, the retroreflector array is sized using a lower boundary for the rolling rate of 5 deg/s.
 Verification: Test, analysis.
- * **REQ-SYS-1.1.6:** The retroreflector array shall accommodate a satellite yawing oscillation of $\pm 20^\circ$.
Rationale: Even though Delfi-PQ was designed to constrain the yawing axis, small perturbations were still present due to atmospheric drag. The actual attitude exhibited a yawing oscillation behavior limited to $\pm 20^\circ$ due to the constant correction induced by the passive attitude control.
 Verification: Test, analysis.
- * **REQ-SYS-1.1.7:** The retroreflector array shall accommodate a satellite pitching oscillation of $\pm 20^\circ$.
Rationale: Even though Delfi-PQ was designed to constrain the pitching axis, small perturbations were still present due to atmospheric drag. The actual attitude exhibited a pitching oscillation behavior limited to $\pm 20^\circ$ due to the constant correction induced by the passive attitude control.
 Verification: Test, analysis.
- **REQ-SYS-1.2:** The retroreflector array shall fit on the Da Vinci satellite.
Rationale: The new satellite being developed by the Da Vinci project requires the implementation of an array of retroreflectors to calibrate its GNSS receiver.
 Verification: Inspection, analysis.
 - * **REQ-SYS-1.2.1:** Rails shall have a minimum width of 8.5 mm measured from the edge of the rail to the first protrusion on each face.
Rationale: This requirement comes from the ESA CubeSat recommendations for the use of the CubeSat launch case [47]. From the width of the satellite the protrusion allowed can be computed subtracting the minimum width of the rail.
 Verification: Inspection, analysis.
- **REQ-SYS-2:** The retroreflector array shall achieve an AOI on the retroreflectors lower than 42° .
Rationale: Since the options of retroreflectors to be integrated on the new TU Delft platform are back-coated corner cube retroreflectors, their OCS response at an AOI greater than 42° tends to zero. Limiting the AOI will avoid signal leakage and ensure a strong enough returning beam.
 Verification: Analysis.
- **REQ-SYS-3:** The probability of false alarm of the ranging detector shall be lower than 2%.
Rationale: The probability of false alarm of the ranging detector should be kept as low as possible. However, in order to determine a threshold of returning photo-electrons a limit of 2% for the probability of false alarm was set as also implemented by Degnan in his analysis for MOBILAS station [28].
 Verification: Analysis.
- **REQ-SYS-4:** The probability of detection of the ranging detector shall be higher than 99%.
Rationale: The probability of detection of the ranging detector should be kept as high as possible.

However, in order to determine a threshold of returning photo-electrons a limit of 99% for the probability of detection was set as also implemented by Degnan in his analysis for MOBLAS station [28].

Verification: Analysis.

- **REQ-SYS-5:** The accuracy of the distance measurements obtained with ranging shall be better than kilometer-level.

Rationale: Distance measurements with radar in LEO for small satellites typically achieve meter-level accuracy. However, due to the limited number of measurements per orbital pass, the resulting orbital models exhibit errors on the order of kilometers. To justify the integration of the retroreflector array, the accuracy of the distance measurements obtained through ranging must surpass that of radar-based models. This requirement plays a crucial role in defining certain parameters for the Delft laser communication station, which are still under development.

Verification: Analysis.

3.2. Approach

This section outlines the overarching steps taken during the development of this thesis to address the research objectives and questions presented in chapter 1. The rationale behind the simulations performed is discussed, along with their outputs and how they correlate to the research questions. The actual implementation and results are elaborated upon in the subsequent chapters.

Based on the literature review documented in chapter 2, the work of this thesis is divided into three main blocks. First, the design and optimization of the array configuration to be integrated on the new Delft platforms is conducted. This is achieved through a probability of visibility simulation, the steps of which are detailed in subsection 3.2.1. Next, the OCS required to achieve a strong enough signal for ranging measurements, considering both ILRS and the Delft laser communication station, is determined. This is done by performing a link budget analysis based on the radar link equation, along with station settings and atmospheric conditions. The steps involved are outlined in subsection 3.2.2. Finally, the batch of retroreflectors acquired by the DSE is tested to verify if their performance matches the manufacturer specifications. Any discrepancies and performance losses could compromise the retroreflector array functionality. Therefore, based on the test outcomes, iterations on the OCS and array design are performed. The test procedures are described in subsection 3.2.3.

3.2.1. Probability of Visibility Simulation

In this subsection, the methodology used in the probability of visibility simulation is discussed. However, the details of the actual implementation and the outcomes from the simulation are thoroughly examined in chapter 4.

To assess the PoV of the satellite, requirement REQ-SYS-2 is used as the main driving factor. The maximum angle of incidence for which the retroreflector can produce a strong enough signal for ranging measurement is used as the threshold to define the visibility of the satellite. Therefore, if, at a specific location in the sky with respect to the ground station and specific orientation of the satellite, any retroreflector within the array integrated on the satellite has an angle of incidence with the laser beam lower than 42° , the satellite is considered visible. Conversely, if the angle of incidence is higher than 42° , the satellite is considered not visible. Based on this overarching principle, the probability of visibility of a specific array configuration coupled with the satellite attitude can be computed.

The simulation is based on a geometrical representation of all possible orbital passes within the FoV of the ground station, defined from the horizon up to the zenith and 360° azimuth. Furthermore, the orbit of the satellite is assumed to be circular, and the satellite is simulated as a point mass. The simulation calculates the satellite position over time for each arc spanning the spherical FoV of the station in a single pass trajectory, from West to East, due to its symmetric properties. Figure 3.1 displays an orbital pass over the station of a satellite with a circular orbit of 525 km and one retroreflector placed on the bottom face of the satellite, which is always pointing nadir. Figure 3.2 shows how the inclination of the orbital arc within the station FoV is updated.

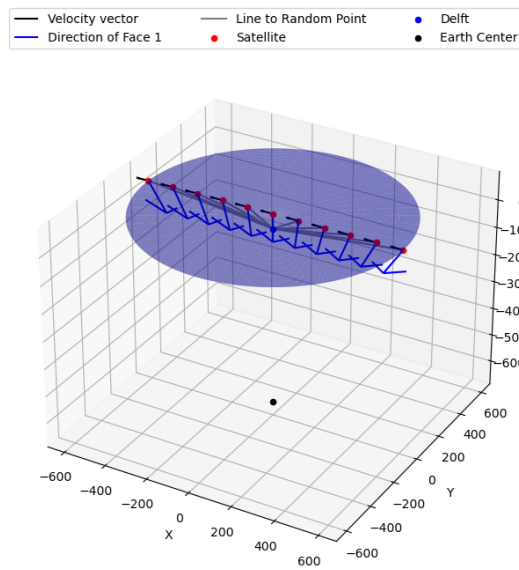


Figure 3.1: Orbital pass at zenith with one retroreflector constantly pointing nadir.

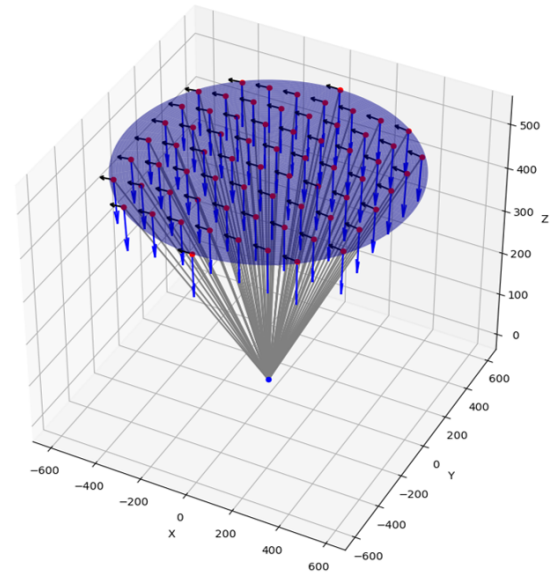


Figure 3.2: Multiple orbital passes at different inclinations with one retroreflector constantly pointing nadir.

The angle of incidence of the retroreflector is computed by checking the angle between the normal to the retroreflector reflecting surface and a line traced from the satellite to the ground station spanning the slant range. Figure 3.3 shows the angle of incidence of the aforementioned case at each satellite location within the station FoV. Furthermore, Figure 3.4 presents a color-coded map. Areas where the satellite is visible are highlighted in green, indicating that at least one of the retroreflectors in the array has an AOI less than 42° . In contrast, areas shown in red represent regions where the satellite is not visible, meaning all retroreflectors in the array have an AOI greater than 42° .

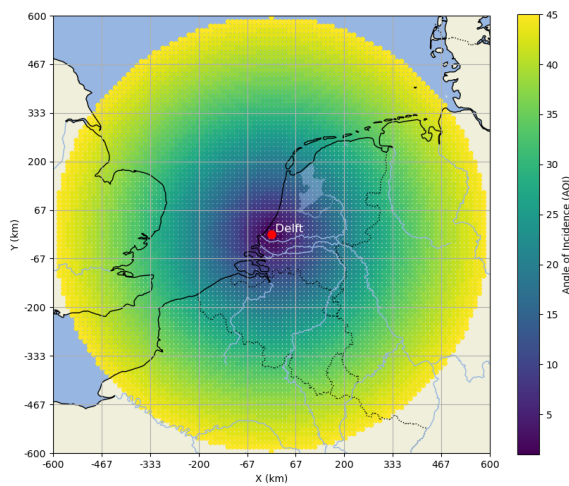


Figure 3.3: Angle of incidence map from the Delft station for 1 retroreflector always pointing nadir.

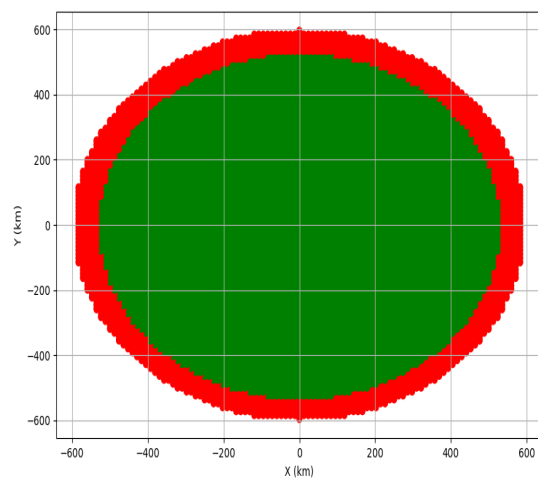


Figure 3.4: Map of visibility satellite positions for 1 retroreflector always pointing nadir.

However, the satellite attitude considered in this case is not the attitude that represents Delfi-Twin, as discussed in section 2.5. Therefore, the simulation includes rolling of the satellite and an oscillating behavior in its pitching and yawing axes. With a rolling rate between 5 deg/s and 10 deg/s and various possible orientations of the satellite at the start of each simulation arc, a probabilistic approach is adopted. The number of times the satellite is visible at a specific elevation with respect to the station is used to compute the PoV at that elevation angle. This process is repeated for the rolling rate range, using a step size of 1 deg/s, and for the offset starting positions range, with a step size of 10° , generating

a plot as shown in Figure 3.5. This graph was generated for an array configuration of four retroreflectors, one placed on each face around the rolling axis of the satellite, with a rolling rate between 5 deg/s and 10 deg/s and no oscillation in pitching and yawing at an altitude of 525 km.

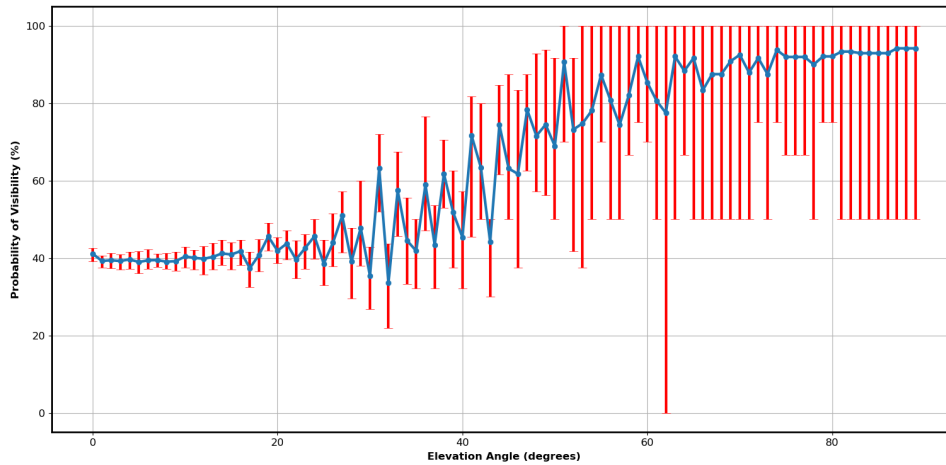


Figure 3.5: Average probability of visibility with max-min variation with 4 retroreflectors, one on each face for rolling rates 5-10 deg/s and starting offsets 0-80 deg.

In summary, considering various configurations within the constraints posed by REQ-SYS-1.1.1, REQ-SYS-1.1.2, REQ-SYS-1.1.3, and REQ-SYS-1.2.1 the objective of the probability of visibility is to retrieve, based on the attitude of the satellite, an optimized configuration that maximizes the probability of visibility at all elevation angles therefore aiming to answer research sub-question RSQ-1. The ideal scenario would be to design a configuration that achieves 100% probability of visibility at all elevation angles. However, this scenario is deemed unrealistic due to the satellite unstable attitude. The simulation described in this subsection takes as inputs and generates the outputs listed below.

Inputs:

- Satellite attitude,
- Satellite orbital parameters,
- Retroreflector array configuration.

Outputs:

- Probability of visibility for each elevation angle,
- Visibility windows.

3.2.2. Link Budget Analysis

In this subsection, the methodology used in the link budget analysis is discussed. However, the details of the actual implementation and the outcomes from the analysis are thoroughly examined in chapter 5.

After optimizing the design of the array configuration, a link budget analysis is performed to assess the required OCS to achieve a strong enough returning signal. The link budget is based on the radar link equation presented in chapter 2, along with the modeling of the OCS response at different angles of incidence and off-axis angles. The link budget analysis aims to answer the research sub-questions RSQ-2, RSQ-3, and RSQ-4.

As discussed in chapter 2, the retroreflector array needs to be designed for a set of ILRS stations and the Delft laser communication terminal. The different parameters of the stations are crucial in determining the required OCS. Consequently, different ranges of working retroreflector radii are expected based on the station implemented. Another factor to consider is the background noise rate, which varies between daylight and nighttime, thereby affecting the required mean number of returning photo-electrons and consequently the OCS. Additionally, the type of retroreflector implemented impacts the link budget.

The link budget is computed at the minimum elevation angle considered since this represents the worst-case scenario. If the link budget is closed at the minimum considered elevation, for all other elevations within the station FoV the link budget will also close.

In addition, the off-axis angle effect is implemented together with the range of velocity aberrations expected to angularly shift the returning beam within the station FoV. This leads to Figure 3.6, a graph

showing the change in OCS response due to different angles of incidence and off-axis angles. The dotted red line is the OCS threshold, indicating that if the OCS is higher than the threshold, the number of returning photons is sufficient to achieve ranging measurements. This threshold is computed from the background noise rate which defines the minimum required mean number of returning photo-electrons to achieve ranging. The grey highlighted region of off-axis angles represents the range of velocity aberrations within the station FoV. At this point, the simulation checks if the OCS values within the velocity aberration range are all above the threshold value. If this condition is true, the implemented radius of the retroreflector is sufficient to perform ranging measurements with the selected station. This approach ensures that if the link budget is closed at the lowest considered elevation angle, it will also close at higher elevation angles. However, this method may lead to a pessimistic scenario, as increasing the elevation angle raises the lower bound of the velocity aberration range, meaning it may not be necessary for the link to close across the entire velocity aberration range at the lowest elevation angle. Additionally, the dips in the OCS response may be sharp and brief, resulting in the link budget not closing for a relatively short range of velocity aberration, which could be negligible. However, it was considered non-trivial to define when these dips can be disregarded and when they cannot.

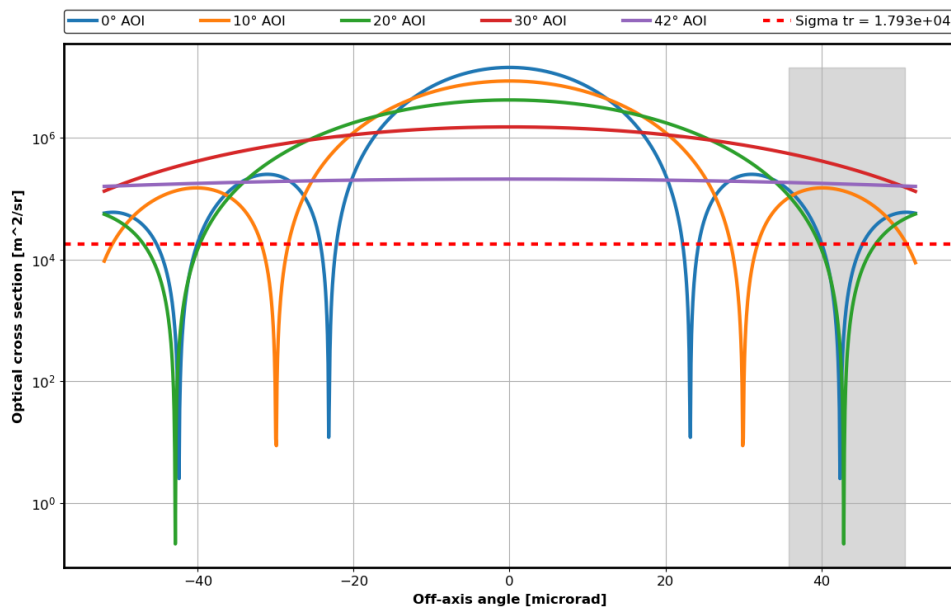


Figure 3.6: OCS w.r.t. off-axis angle for different AOI with radius 0.014 m using Potsdam and $n_{pe} = 10$.

A series of radius values is assessed to define the range and the optimum value per implemented station. After selecting a retroreflector radius that can be implemented on the new TU Delft platforms to achieve laser ranging measurements, a sensitivity analysis on the number of returning photons is performed to check how the hardware settings, orbital parameters, and atmospheric conditions affect the array performance. Furthermore, following the sensitivity analysis and the selection of the retroreflector dimensions, recommendations for the settings of the Delft laser communication terminal are gathered. Lastly, a margin analysis on the reflectivity is performed by keeping the radius constant while varying the reflectivity of the retroreflector to obtain the range of reflectivity required to close the link budget. In summary, the objective of the link budget analysis is to define the retroreflector dimensions to be implemented on Delfi-Twin and the Da Vinci satellite. The simulation takes as inputs and generates the outputs listed below.

Inputs:

- Station parameters,
- Retroreflector properties,
- Minimum elevation angle,
- Background noise photo-electron rate,
- Satellite altitude.

Outputs:

- Range of working retroreflector radii,
- OCS threshold,
- Sensitivity analysis on returning photon count,
- Reflectivity margin range.

3.2.3. Retroreflector Testing & Integration

The batch of retroreflectors acquired by the DSE will be inspected and tested to verify if the performance of each retroreflector meets the manufacturer specifications. This step is crucial since the batch size is smaller than what the manufacturer typically supplies, suggesting that the retroreflectors were likely sourced from backup stock. As a result, a performance decrease of up to 30% might be identified.

The inspection will take place in the cleanroom facility at the Aerospace Faculty. However, TU Delft currently lacks the necessary facilities to accurately assess the optical performance of the retroreflectors. Therefore, the tests could be conducted at an external testing facility, such as the Frascati INFN laboratory [48]. Each retroreflector in the batch should be evaluated for its reflectivity and its maximum angle of incidence for effective reflection.

Based on the test results, an iteration on the required OCS and the array configuration may be necessary. Additionally, if performance outliers are identified, meaning their reflectivity does not fall within the margin set by the link budget analysis, those retroreflectors will be discarded and not implemented in the satellite array. The results of the inspection and further details on the tests are discussed in chapter 6.

4

Probability of Visibility

In this chapter, the outcomes of the PoV simulation are discussed. As mentioned in subsection 3.2.1, the goal of this simulation is to identify which array configuration maximizes the PoV at all elevation angles, given the implemented satellite attitude. Therefore, for each attitude, a configuration will be selected.

In section 4.1, the analyzed scenarios are discussed. In section 4.2, the PoV simulation is validated by comparing a real-life scenario with its outcome to assess the trustworthiness of the results. Section 4.3 details the selection of the most suitable configuration for each attitude. Additionally, the intermediate graphs from the simulation, which illustrate how the attitude has been simulated, the regions of visibility and non-visibility within the station FoV, and the average PoV per elevation angle for each scenario, are compiled in Appendix A.

4.1. Scenarios

In this section, the scenarios analyzed using the PoV simulation are discussed. These scenarios are generated based on the requirements listed in section 3.1 and involve various combinations of array configurations and satellite attitudes.

4.1.1. Array configuration

The main limitations on the array configuration are set by the dimensions of the satellite and the limited number of available retroreflectors. These constraints are defined by REQ-SYS-1.1.1, REQ-SYS-1.1.2, REQ-SYS-1.1.3, and REQ-SYS-1.2.1, where the maximum number of retroreflectors is limited to 8, and the protrusion allowances are set by the launch case, restricting the inclination at which the retroreflectors can be installed with respect to the satellite faces. Furthermore, not all faces of the satellite can accommodate retroreflectors due to space constraints imposed by other components. For Delfi-Twin, the front and back faces are unavailable for retroreflector placement: the front face contains multiple instruments, while the back face hosts passive attitude control flaps that obstruct the retroreflector FoV. Consequently, retroreflectors can only be installed on the four remaining faces. Five possible array configurations have been identified, and their details are described below.

- **CONF-1:** The **1 face** configuration where 1 CCR is placed at the center of the bottom face of the satellite,
- **CONF-2:** The **Astrocast** configuration where 3 CCRs are placed at the center of the bottom face of the satellite forming a triangular shape,
- **CONF-3:** The **4 faces** configuration where 4 CCRs are implemented, 1 placed at the center of each available face,
- **CONF-4:** The **8 faces** configuration where 8 CCRs are implemented, 2 placed on each available face around the rolling axis with an outward 15° inclination w.r.t the face,

- **CONF-5:** The **8 faces alt** configuration where 8 CCRs are implemented, 2 placed on each available face around the rolling axis with an outward 15° inclination w.r.t the face and an alternated shift of $\pm 15^\circ$ around the pitching axis.

To provide a clearer understanding of the considered array configurations, sketches of each configuration are shown in Figure 4.2, Figure 4.3, Figure 4.4, Figure 4.5, and Figure 4.6.

CONF-2 was taken from a 3U CubeSat satellite launched by Astrocast, namely Astrocastp1, which successfully performed SLR measurements with stations of the ILRS network. This configuration places the CCRs in a triangular formation with an inclination of 20° from the nadir vector, with the rear two CCRs rotated by $\pm 30^\circ$ outward compared to the anti-flight direction, forming the FoV shown in Figure 4.1 [49]. Furthermore, this configuration was also used to validate the PoV simulation by implementing real-life laser ranging data from Astrocastp1, as discussed in section 4.2.

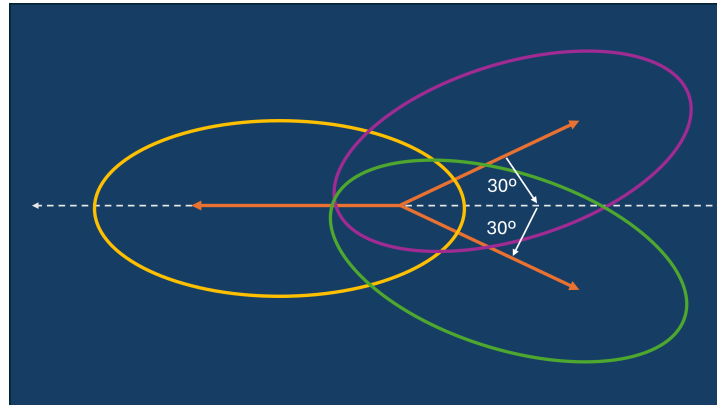


Figure 4.1: Field of view of the retroreflector array on the Astrocast satellite [49].

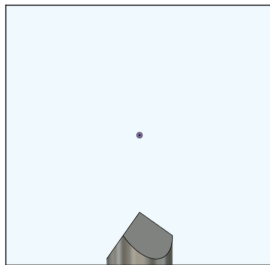


Figure 4.2: Sketch of the top view of CONF-1, 1 face.

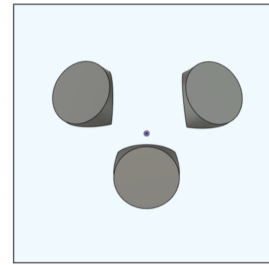


Figure 4.3: Sketch of the bottom view of CONF-2, Astrocast.

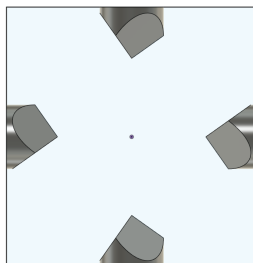


Figure 4.4: Sketch of the top view of CONF-3, 4 faces.

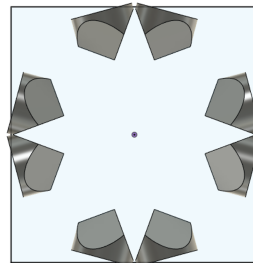


Figure 4.5: Sketch of the top view of CONF-4, 8 faces.

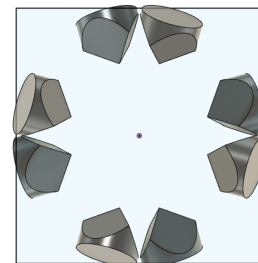


Figure 4.6: Sketch of the top view of CONF-5, 8 faces alt.

4.1.2. Satellite Attitude

The satellite attitudes considered for the tested scenarios are generated based on the expected attitudes of the analyzed satellites. Three attitudes are identified and listed below.

- **ATT-1:** Fixed attitude with the bottom face constantly looking nadir.
- **ATT-2:** Fixed attitude in the pitching and yawing axes with a rolling rate between 5 deg/s and 10 deg/s.
- **ATT-3:** Rolling rate between 5 deg/s and 10 deg/s with an oscillation in pitching and yawing of $\pm 20^\circ$ at a 5 deg/s rate.

The first attitude represents the Da Vinci satellite, the second one represents the ideal scenario for Delfi-Twin, where the fixed axes do not exhibit any oscillations. Lastly, the third attitude represents the actual expected attitude for Delfi-Twin, where oscillations in pitching and yawing are anticipated. To better understand the considered attitude, a sketch of the satellite with the roll, yaw, and pitch moments highlighted is presented in Figure 4.7.

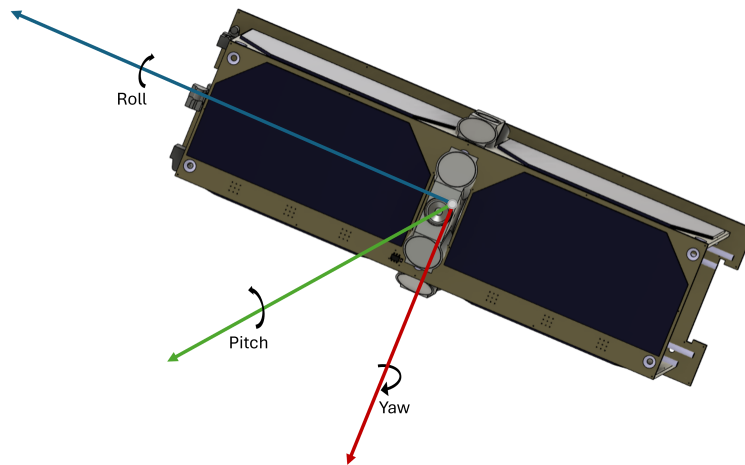


Figure 4.7: Roll, yaw and pitch.

4.2. Validation

To assess the reliability of the simulation outcomes, a validation process was conducted using Astrocasp first satellite, Astrocasp1, with COSPAR ID 1809941, as the validation case. Additionally, the successful sets of SLR measurements performed by the Graz station with the Astrocasp satellite were considered [50]. For each orbital pass, the first and last measurement of the set were verified. Skyfield, a Python library that computes positions of stars, planets, and satellites in orbit around Earth [51], was employed alongside the satellite Two-line elements (TLE) to extract its exact position in terms of elevation and azimuth relative to the station. TLE data provides crucial orbital parameters such as the satellite position, velocity, and other relevant information at a specific epoch. These parameters are generated based on observations from ground-based tracking stations, radar systems, or other tracking methods. By processing these observations, the satellite orbital elements are determined and encoded into the TLE format [52]. Knowing the satellite position relative to the station at the beginning and end of the measurement set, along with its array configuration, allows for verification of the visibility simulation. If the satellite remains within the visible region throughout the entire set of measurements, the simulation is considered verified.

Four orbital passes were measured by the Graz station. Table 4.1, Table 4.2, Table 4.3, and Table 4.4 display the time, distance, elevation, and azimuth of the satellite at the start and end of the measurements with respect to the Graz station. Meanwhile, Figure 4.8, Figure 4.9, Figure 4.10, and Figure 4.11 show the visibility maps generated by the PoV simulation together with the trajectory of the pass. As can be seen, the satellite is always within the visibility window during the first and last measurements, verifying the simulation.

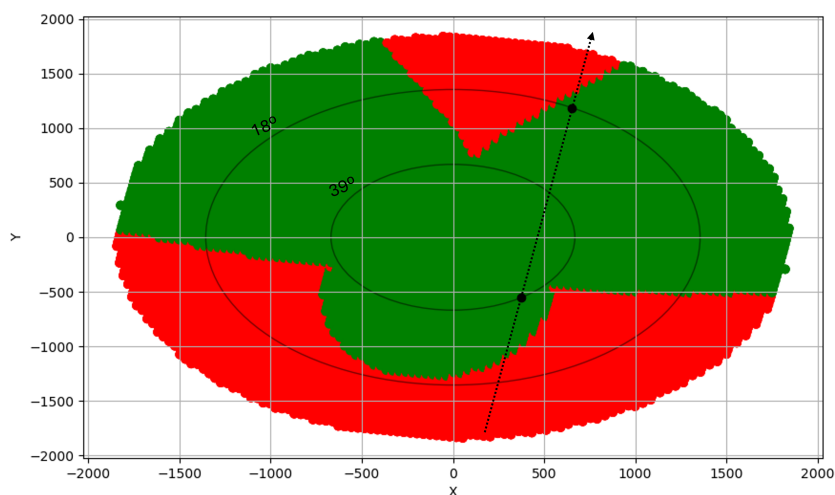


Figure 4.8: Visibility map of Astrocastp1 pass of 2020-07-22.

Table 4.1: Position parameters of Astrocastp1 during first and last measurement of the orbital pass above Graz of 2020-07-22.

Measurement	Seconds of day	Time	Distance [km]	Elevation [deg]	Azimuth [deg]
1 st	76093.35	21:08:13	863.9	39.06	213.80
Last	76326.95	21:12:06	1435.1	18.04	331.22

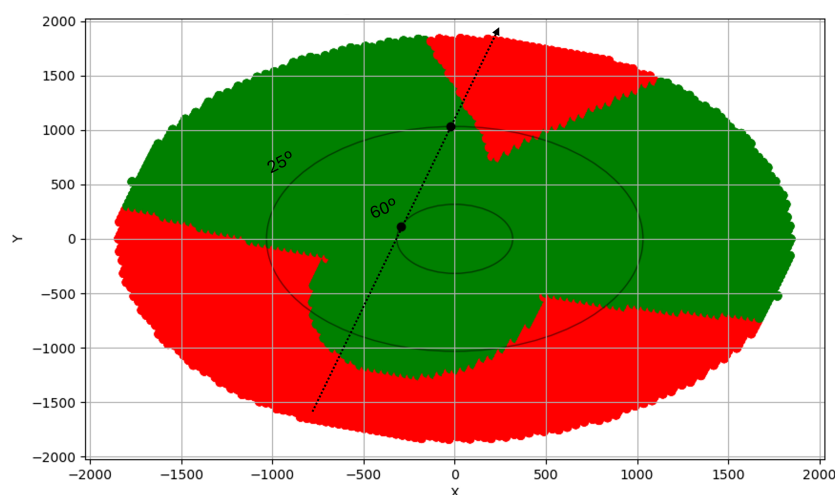


Figure 4.9: Visibility map of Astrocastp1 pass of 2020-07-14.

Table 4.2: Position parameters of Astrocastp1 during first and last measurement of the orbital pass above Graz of 2020-07-14.

Measurement	Seconds of day	Time	Distance [km]	Elevation [deg]	Azimuth [deg]
1 st	73852.78	20:30:52	655.4	60.76	68.16
Last	73978.36	20:32:58	1155.7	25.74	1.34

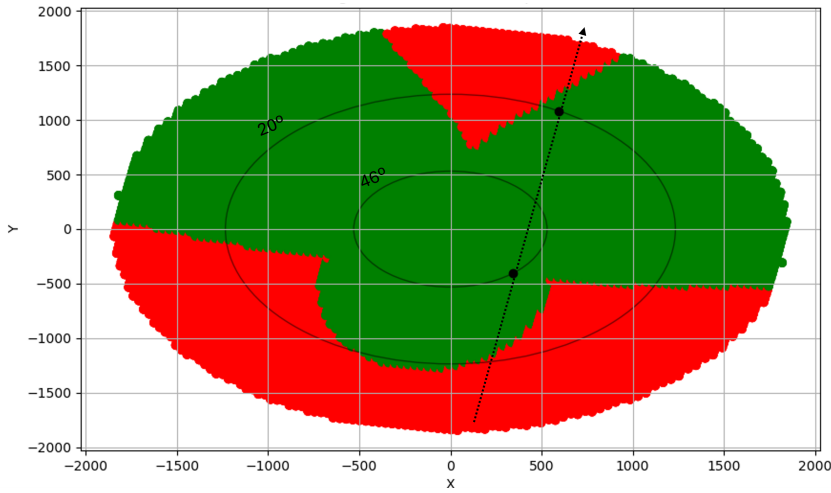


Figure 4.10: Visibility map of Astroctsp1 pass of 2020-06-12.

Table 4.3: Position parameters of Astroctsp1 during first and last measurement of the orbital pass above Graz of 2020-06-12.

Measurement	Seconds of day	Time	Distance [km]	Elevation [deg]	Azimuth [deg]
1 st	75998.56	21:06:38	790.5	46.28	220.12
Last	76202.17	21:10:02	1356.3	20.62	331.25

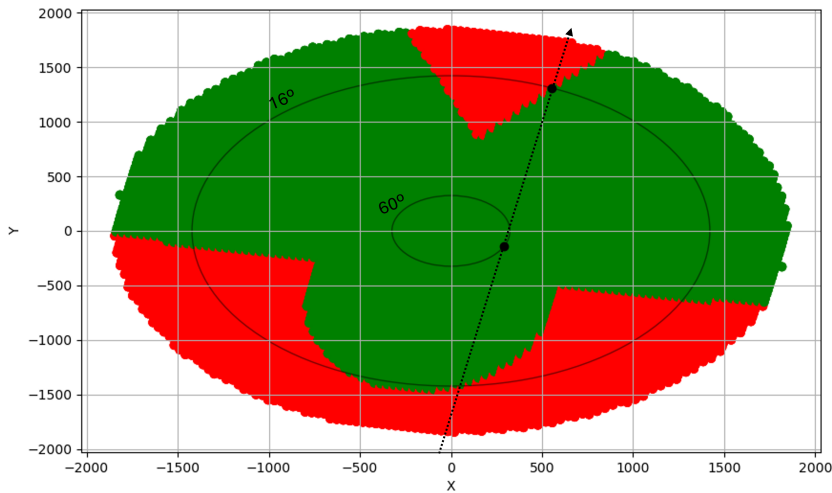


Figure 4.11: Visibility map of Astroctsp1 pass of 2020-06-11.

Table 4.4: Position parameters of Astroctsp1 during first and last measurement of the orbital pass above Graz of 2020-06-11.

Measurement	Seconds of day	Time	Distance [km]	Elevation [deg]	Azimuth [deg]
1 st	75742.67	21:02:22	674.0	60.29	243.59
Last	75942.34	21:05:42	912.9	16.77	337.11

4.3. Results

The PoV simulation has been run for all configurations and satellite attitudes, providing data about the average PoV at all elevation angles for each configuration with different attitudes. The intermediate graphs of the simulation, which display how the attitude has been simulated, the regions of visibility and non-visibility within the FoV of the station, and the average PoV per elevation angle, are gathered in Appendix A. By analyzing the PoV curves per elevation angle for each configuration, it is possible to determine the most suitable configuration for each satellite attitude.

Starting with attitude 1, where the attitude is fixed with the bottom face of the satellite always pointing nadir, a plot showing the average PoV at all elevation angles for the 5 configurations can be generated,

as shown in Figure 4.12. Furthermore, the main variables for comparison are summarized in Table 4.5, which provides the average and standard deviation of the PoV for each configuration. The average represents the mean value across all elevation angles, as well as all considered rolling rates and offsets. The standard deviation shows how the average value across all elevation angles varies with different rolling rates and offsets. A higher standard deviation indicates that the PoV fluctuates more significantly depending on the rolling rate and offset applied, providing insight into the robustness of the implemented configuration for different attitudes. Additionally, the table includes the minimum elevation angle limit, α_{lim} , beyond which the satellite is always 100% visible.

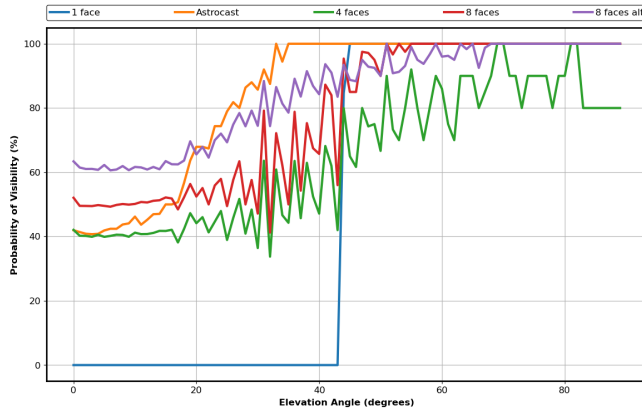


Table 4.5: Average, standard deviation and limit value for each configuration for attitude 1.

	Avg	Std	α_{lim}
1 face	50.94%	-	45°
Astrocast	84.97%	-	35°
4 faces	64.71%	1.90%	N/A
8 faces	78.04%	0.64%	51°
8 faces alt	84.70%	1.11%	68°

Figure 4.12: Combined graph of average PoV per elevation angles of all tested configuration for attitude 1.

Looking at the data, it can be observed that the highest PoV average is obtained by implementing the **Astrocast** configuration. This configuration also presents the lowest minimum elevation angle limit, meaning that the satellite will be 100% visible for a longer arc during a pass, providing more time to collect SLR measurements. It can also be observed that the standard deviation for the **1 face** configuration and the **Astrocast** configuration is null. This is because no offset position in entering the FoV has been considered for these two configurations, as they have retroreflectors on only one face. Therefore, it would not have made logical sense to test orbital passes where the retroreflectors were not on the bottom face. In conclusion, it can be stated that the most suitable configuration for a fixed attitude with the bottom face always pointing nadir is the **Astrocast** configuration, providing 100% coverage at an elevation angle higher than 35°.

The same graph and table were generated for attitude 2, where the attitude is fixed in the pitching and yawing axes but a rolling rate between 5 deg/s and 10 deg/s is considered. Figure 4.13 displays the combined PoV average per elevation angle for the 5 configurations tested for attitude 2, while Table 4.6 lists the main variables for comparison.

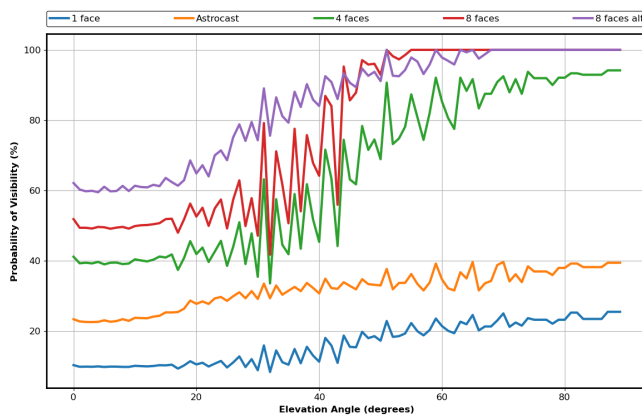


Table 4.6: Average, standard deviation and limit value for each configuration for attitude 2.

	Avg	Std	α_{lim}
1 face	16.47%	3.00%	N/A
Astrocast	31.81%	3.95%	N/A
4 faces	65.42%	0.73%	N/A
8 faces	77.95%	0.23%	55°
8 faces alt	84.69%	0.23%	68°

Figure 4.13: Combined graph of average PoV per elevation angles of all tested configuration for attitude 2.

For attitude 2, the **8 faces** and **8 faces alt** configurations are the only ones to present a minimum elevation angle limit after which the satellite is always visible. Furthermore, they have the highest PoV average. This was expected, as the first two configurations have retroreflectors only on one face, making it unrealistic to cover enough regions while the satellite is rolling. In contrast, the **4 faces** configuration never reaches a limit because the gaps between the visibility of one retroreflector and another are too long. In this case, if measurements are taken from an elevation angle higher than 55° , the **8 faces** configuration is deemed more suitable as it will always provide visibility. However, if the measurements are started from a lower elevation angle, the **8 faces alt** configuration provides a higher probability of visibility, even though it results in a higher limit. Consequently, the most suitable configuration for this case is the **8 faces alt** one.

The same graph and table were generated for attitude 3, where the satellite has a rolling rate between 5 deg/s and 10 deg/s with an oscillation in pitching and yawing of $\pm 20^\circ$ at a 5 deg/s rate. Figure 4.14 displays the combined PoV average per elevation angle for the 5 configurations tested for attitude 3, while Table 4.7 lists the main variables for comparison.

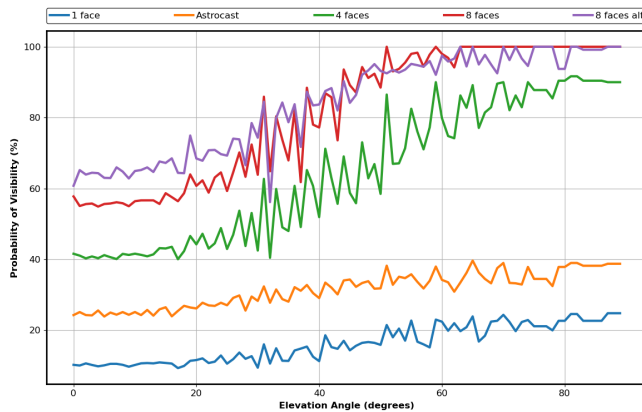


Table 4.7: Average, standard deviation and limit value for each configuration for attitude 3.

	Avg	Std	α_{lim}
1 face	16.23%	2.97%	N/A
Astrocast	31.47%	4.08%	N/A
4 faces	64.53%	2.34%	N/A
8 faces	81.55%	1.12%	65°
8 faces alt	83.96%	0.98%	N/A

Figure 4.14: Combined graph of average PoV per elevation angles of all tested configuration for attitude 3.

For attitude 3, the only configuration that presents a limit is the **8 faces** one. However, the **8 faces alt** configuration has a higher PoV average. The other configurations do not perform as well as these two, as expected. Comparing this case with attitude 2, the disparity in PoV of **8 faces** and **8 faces alt** configurations is tighter. Consequently, the most suitable configuration for this case is the **8 faces** one.

In conclusion, for Delfi-Twin, where attitude 3 is applicable, the most suitable configuration has been determined to be the **8 faces** configuration. This results in an average PoV of 81.55% with a minimum elevation angle limit of 65° . While, for the Da Vinci satellite, where attitude 1 applies, the most suitable configuration is the **Astrocast** configuration, resulting in an average PoV of 84.97% with a minimum elevation angle limit of 35° .

5

Link Budget Analysis

In this chapter, the outcomes of the link budget analysis are discussed. As mentioned in subsection 3.2.2, the goal of this analysis is to select the appropriate retroreflector size for the new TU Delft platforms based on the considered ground stations and their configurations. Furthermore, recommendations for the Delft laser communication station are provided to enable successful laser ranging with the selected array. Finally, a reflectivity margin is established to determine whether the retroreflectors within the acquired batch should be accepted or discarded.

In section 5.1, the considered ground stations are compared to gain insights into how different station parameters affect the OCS response of the retroreflector. Section 5.2 presents the verification and validation process used to assess the trustworthiness of the analysis as well as its correct implementation. In section 5.3, the background noise rate is computed for each station to determine the required mean number of returning photons, thus setting the strength of the returning signal. Consequently, section 5.4 compiles the results of the link budget analysis conducted for each station and discusses the selection of the retroreflector size. In section 5.5, a sensitivity analysis is performed to identify the most critical parameters of the link budget and examine how the returning photon count varies with respect to these parameters. Furthermore, a reflectivity margin constraint is derived. Finally, section 5.6 provides recommendations for Delft laser communication station to enable laser ranging between the station and Delfi-Twin.

5.1. Ground Station Comparison

The implementation of the retroreflector array with different ground stations provides different optimum outcomes per station with respect to the required OCS. In order to understand how station parameters affect the outcome, a ground station comparison is performed. The radar link equation explained in section 2.3 is solved by implementing the different station parameters, a constant assumed value for the required mean number of returning photo-electrons of 10, and clear atmospheric conditions, with the two-way atmospheric and cirrus cloud attenuation factors set to 0.8. Furthermore, the required OCS is computed at different angles of incidence. Consequently, the required retroreflector radius is retrieved assuming an on-axis reflection, without considering the velocity aberration effect. Figure 5.1 and Figure 5.2 display the computed required OCS and required retroreflector radius, respectively, for each station at different laser angles of incidence under the aforementioned conditions.

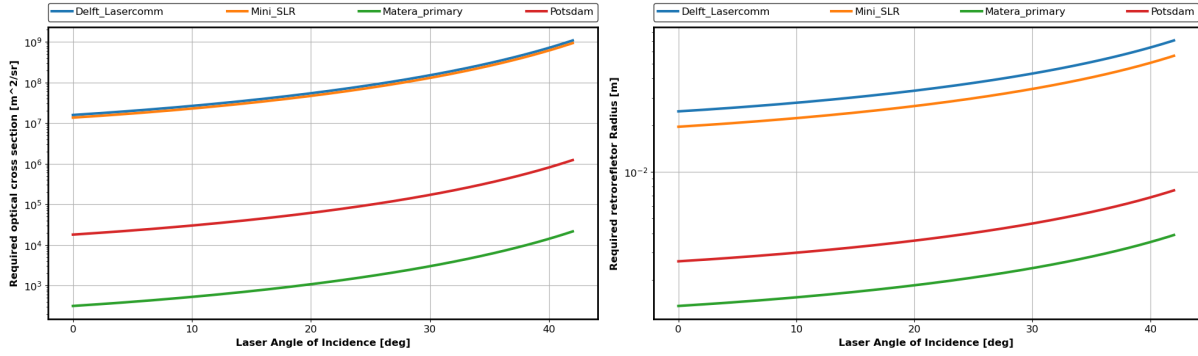


Figure 5.1: Required optical cross section for on-axis reflection w.r.t. AOI of laser beam to reach $n_{pe} = 10$. **Figure 5.2:** Required retroreflector radius for on-axis reflection w.r.t. AOI of laser beam to reach $n_{pe} = 10$.

For the Delft laser communication station, the continuous laser power, P_{laser} , was converted into laser pulse energy, E_p , assuming an OOK modulation setup. OOK modulation involves converting the signal into on and off states, enabling the continuous laser to behave like a pulsed one. To calculate the laser pulse energy, the pulse length, t_s , needs to be determined. For the Delft laser communication station, a pulse length of $33.3 \cdot 10^{-9}$ s was assumed, corresponding to an error of 9.98 meters in determining which photon within the pulse is the actual returning one. This error is within the constraints set by REQ-SYS-5. The selected pulse length is one order of magnitude larger than that of the Mini-SLR station, which has a pulse length of 4 ns, as shown in Table 2.7. Using Equation 5.1, the laser pulse energy for the Delft laser communication station was computed, resulting in $1.665 \cdot 10^{-8}$ J.

$$E_p = P_{laser} \cdot t_s \quad (5.1)$$

As observed from the graphs in Figure 5.1 and Figure 5.2, the ILRS stations outperform both the Mini-SLR and the Delft laser communication station, with the Matera station being the most powerful. This result was expected, as the laser pulse energy of these two stations is 3 to 5 orders of magnitude higher, leading to a required OCS for the ILRS stations that is 4 orders of magnitude smaller. Consequently, a retroreflector radius 2 orders of magnitude smaller is needed.

However, it is noteworthy that the Delft laser communication station, coupled with the assumed modulation scheme, performs relatively close to the Mini-SLR, despite having a lower laser pulse energy. This is due to the fact that the Mini-SLR has lower receiver efficiency, with its transmit and receive apertures being less than half the size of those on the Delft laser communication station.

This ground station comparison highlighted the differences in power between the ILRS station and others, revealing the challenges of converting a laser communication station into a laser ranging station, as well as the miniaturization achieved by the Mini-SLR. Nevertheless, in the following sections, a link budget analysis is conducted for all the considered stations to develop a retroreflector array that is compatible with all of them.

5.2. Verification & Validation

To assess whether the link budget analysis code correctly implements the equations and analyzes the problem properly, a verification procedure is performed. The known OCS response of a predefined retroreflector is compared with the OCS response produced by the link budget analysis. Furthermore, to determine whether the link budget analysis outputs are consistent with real-life applications, a validation procedure is conducted. The parameters of the space and ground segments of Astrocstp1 passes considered in section 4.2 are input into the code to compare the outcomes with actual events.

5.2.1. OCS response verification

Before analyzing the results of the link budget analysis, the equations implemented within the code need to be verified to ensure the trustworthiness of the simulation. A similar analysis was conducted by Meyer, where the OCS response of a retroreflector at different AOI and off-axis angles was evaluated [38]. Table 5.1 lists the variables used by Meyer in his simulation. These same variables were input into

the link budget analysis code to determine if the simulated results align with those obtained by Meyer. Figure 5.3 shows the overlap between Meyer's OCS response and the OCS response generated by the simulation, while Figure 5.4 displays the difference between the generated OCS response and Meyer's, normalized by Meyer's values.

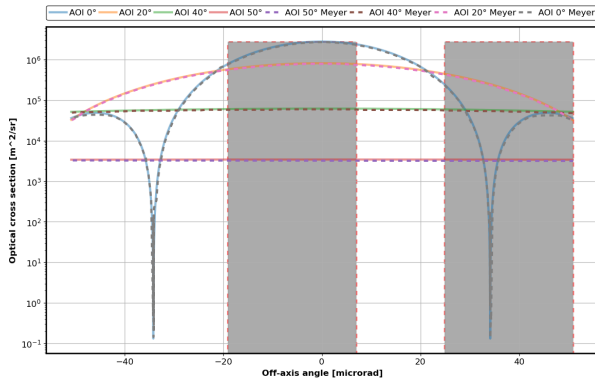


Figure 5.3: OCS w.r.t. off-axis angle for different AOI comparison with Meyer case.

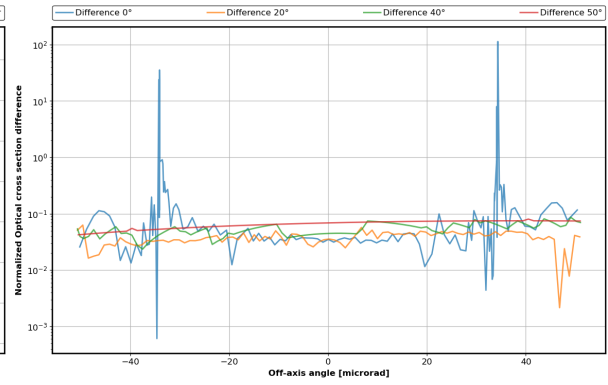


Figure 5.4: Normalized OCS difference w.r.t. off-axis angle for different AOI comparison with Meyer case.

Table 5.1: Meyer case scenario settings [38].

Simulation settings	
Minimum elevation angle	20°
AOI range	0° - 50°
Satellite settings	
Satellite altitude	500 km
Retroreflector settings	
Reflectivity	0.78
Index of refraction	1.461
Retroreflector ratio	$\sqrt{2}$
Retroreflector radius	19 mm
Dihedral angle	3.8''
Station settings	
Laser wavelength	1064 nm

As can be observed from Figure 5.3, the OCS generated by the link budget seems to align with the OCS obtained by Meyer. The two graphs match in reproducing the OCS response behavior under varying AOI values and at different off-axis reflection angles. In terms of amplitude, the difference can be observed in Figure 5.4, with the highest error occurring at the dips of the 0° AOI curve. This discrepancy is attributed to the plot digitization of Meyer's graph, where each point was retrieved using the Web Plot Digitizer by Ankit Rohatgi [53]. As a consequence, the highest error is found at the dips, which were the most difficult to digitize due to the rapid decrease in OCS. Therefore, this difference is not caused by an error in the simulation and can be disregarded in the verification discussion. Furthermore, the velocity aberration ranges for both the spoiled and unspoiled cases are identical, as shown by the two grey shaded areas. This comparison, confirms the correct implementation of the equations used to simulate the OCS response of retroreflectors for both on-axis and off-axis reflections.

5.2.2. Astrocst case validation

To validate the outcomes of the link budget analysis, passes of Astrocstp1, the first Astrocst satellite, were considered. Table 5.2 and Table 5.3 show the ground segment specifications of Graz station and the space segment settings of Astrocst satellite respectively.

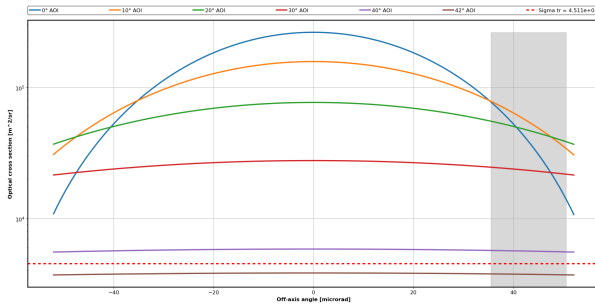
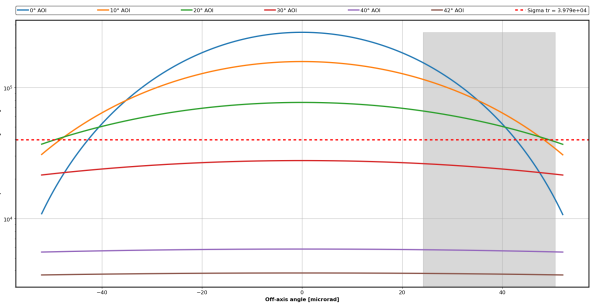
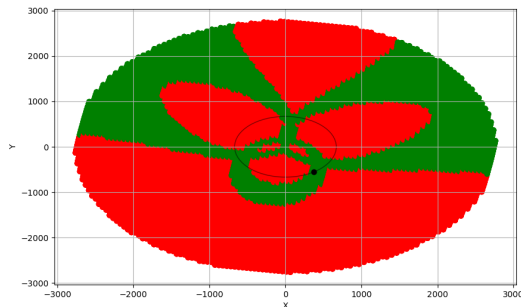
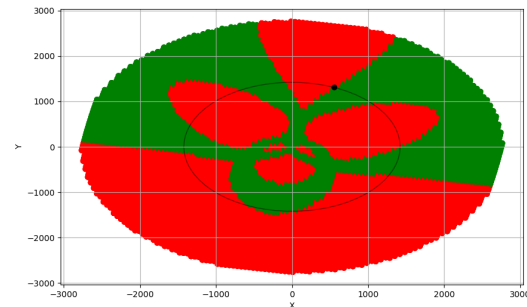
Table 5.2: Main specifications of station 7839 in Graz of the ILRS network [54].

Parameter	Symbol	Value
Transmit aperture	D_t	10 cm
Beam diameter	D_{beam}	6 cm
Receiver aperture	D_r	50 cm
Obscuration	γ	0
Laser pulse energy	E_p	0.4 mJ
Laser repetition rate	f_{laser}	2 kHz
Laser pulse width	t_s	10 ps
Operating wavelength	λ	532 nm
Full-width beam div.	θ_d	25 μ rad
Beam stability	$\Delta\theta_p$	0.41 μ rad
Transmitter efficiency	η_t	0.7
Receiver efficiency	η_r	0.3
Efficiency of detector	η_d	20%

Table 5.3: Astrocst satellite scenario settings [49].

Satellite settings	
Satellite altitude	575 km
Retroreflector settings	
Reflectivity	0.96
Index of refraction	1.461
Retroreflector ratio	$\sqrt{2}$
Retroreflector radius	5 mm
Dihedral angle	0''

Using the following variables, the link budget analysis was performed for the critical starting and ending points of the Astrocst1 passes above Graz station. The critical starting and ending points are identified as those with the lowest elevation angles. Specifically, the critical starting point occurs at an elevation angle of 39.06° , while the critical ending point occurs at 16.77° . Figure 5.5 and Figure 5.6 present the simulated OCS of the Astrocst1 retroreflector coupled with Graz station at these two critical elevation angles. It is important to note that the required mean number of returning photons, n_{pe} , was set to 1, assuming a single-photon counting operational mode, which is achievable with the CSPAD detector mounted at the Graz station [54][55].

**Figure 5.5:** OCS w.r.t. off-axis angle for different AOI with Astrocst scenario settings at 39.06° of elevation.**Figure 5.6:** OCS w.r.t. off-axis angle for different AOI with Astrocst scenario settings at 16.77° of elevation.**Figure 5.7:** Visibility of Astrocst1 pass of 2020-07-22 at an elevation of 39.06° for an AOI range between $30^\circ - 40^\circ$.**Figure 5.8:** Visibility of Astrocst1 pass of 2020-06-11 at an elevation of 16.77° for an AOI range between $30^\circ - 42^\circ$.

To understand if the link budget is closed for the simulated instances, the AOI on the retroreflector at the moment of ranging needs to be computed. Figure 5.7 shows the visibility map for an AOI range of $30^\circ - 40^\circ$ for the Astrocst1 pass of 2020-07-22 where the critical starting point was identified. While Figure 5.8 shows the visibility map for an AOI range of $30^\circ - 42^\circ$ for the Astrocst1 pass of 2020-06-11

where the critical ending point was identified. As observed from the visibility maps, both the critical starting and ending points fall within the visible range indicating that the AOIs at those points during the pass were within the considered AOI ranges.

Observing the OCS response of Astrocstp1 retroreflector at the critical starting point, shown in Figure 5.5, it can be concluded that laser ranging was achievable, as the response up to 40° of AOI is above the threshold imposed by Graz station. However, the OCS response, shown in Figure 5.6, at the critical ending point is not above the defined threshold for the retrieved AOIs. This means that, according to the link budget analysis, laser ranging at that moment was not achievable. This highlights how the tool predictions deviate from reality at low elevation angles.

It is also noteworthy that the actual parameters of Graz station during laser ranging of Astrocstp1 may differ from those retrieved from the ILRS site log. Additionally, Astrocstp1 implemented three retroreflectors on the bottom face. Although interference between retroreflectors in the array was assumed to be negligible in the simulation due to their differing inclinations, this assumption may not always hold in real-life applications. In fact, during laser ranging measurements, it is possible that the actual OCS was influenced by contributions from multiple retroreflectors, thereby increasing the returning laser strength. Moreover, the actual attitude of Astrocstp1 was known to deviate from its nominal attitude by 5° to 10° , resulting in a tilting of the satellite during its passes [56]. This could have reduced the angle of incidence for one or more retroreflectors in the array, ultimately bringing the OCS response above the defined threshold.

5.2.3. V&V Conclusion

In conclusion, the link budget tool was validated for elevation angles of 39° and above. Additionally, the OCS response simulation was verified effectively, showing perfect alignment with a known response from a predefined case. However, several limitations in the simulation were identified and are summarized below.

- Ground station parameters during the pass might differ from those listed in the ILRS catalog site, due to the implementation of multiple laser types and detector settings.
- The interaction between multiple retroreflectors was neglected during the modeling of the OCS.
- The attitude of the satellite was simplified, excluding potential deviations from the nominal attitude.

These limitations suggest that the link budget tool tends to produce conservative estimates, mainly at low elevation angles. As such, any retroreflector radius generated by the tool should be considered a worst-case scenario, providing additional margin for higher PoV and improved ranging opportunities in real-life applications.

5.3. Background Noise Rate

To close the link budget, the required mean number of returning photo-electrons, n_{pe} , must be defined. The procedure outlined in subsection 2.3.2 is used to calculate it for both daylight and nighttime conditions. Due to the use of different wavelengths and detector settings, the required mean number of returning photo-electrons depends on the specific station. For these calculations, the receiver field of view is assumed to be $2.5 \cdot 10^{-9}$ sr, corresponding to a slightly sub-optimal full-angle field of view of $40''$, which is considered a common value across ground stations [28].

First, the background photo-electron rate, Λ , is computed for daylight. Equation 2.27 is used, where the background spectral radiance values, N_l , are calculated using Equation 2.28 by implementing the solar spectral irradiance, I_λ , and atmospheric transmittance values, T_λ , for the specific wavelengths used by the stations. Table 5.4 provides an overview of the background photo-electron rates during daylight for each station, along with the necessary variables for their computation.

Table 5.4: Background photo-electron rate during daytime and its components for each considered station.

Variable	Symbol	Unit	Delft Lasercom	Mini-SLR	Matera	Potsdam
Laser frequency	ν	Hz	$1.922 \cdot 10^{14}$	$2.81 \cdot 10^{14}$	$2.81 \cdot 10^{14}$	$5.63 \cdot 10^{14}$
Receiver area	A_r	cm ²	1038.84	294.52	17671.46	1344.76
Receiver field of view	Ω_r	sr	$2.5 \cdot 10^{-9}$	$2.5 \cdot 10^{-9}$	$2.5 \cdot 10^{-9}$	$2.5 \cdot 10^{-9}$
Receiver optics efficiency	η_r	-	0.7	0.1	0.87	0.4
Detector quantum efficiency	η_d	-	0.8	0.3	0.13	0.08
Solar spectral irradiance	I_λ	W m ⁻² nm ⁻¹	0.26	0.63	0.63	1.6
Atmospheric transmittance	T_λ	-	0.8	0.7	0.7	0.65
Background spectral radiance	N_l	W nm ⁻¹ sr ⁻¹ cm ⁻²	$3.3 \cdot 10^6$	$7.0 \cdot 10^6$	$7.0 \cdot 10^6$	$1.6 \cdot 10^5$
Background photo-electron rate	Λ	s ⁻¹	$37.7 \cdot 10^6$	$82.8 \cdot 10^4$	$18.7 \cdot 10^7$	$46.1 \cdot 10^5$

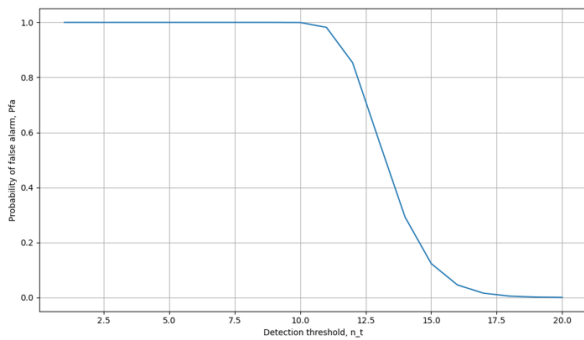
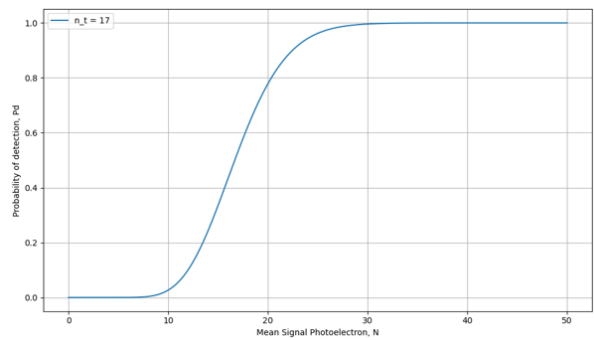
Next, the background photo-electron rate for nighttime is computed using the same equation as for daylight conditions. However, during nighttime, the background spectral radiance, N_l , is obtained from measurements collected by the sky brightness sensor located on top of the Aerospace faculty building at TU Delft, as described in Equation 2.29. This measurement represents a worst-case scenario due to Delft proximity to greenhouses, making it one of the most light-polluted regions in the Netherlands [34]. Consequently, N_l is assumed constant across all stations. Table 5.5 provides an overview of the background photo-electron rates for each station during nighttime, alongside the relevant variables required for their computation.

Table 5.5: Background photo-electron rate during nighttime and its components for each considered station.

Variable	Symbol	Unit	Delft Lasercom	Mini-SLR	Matera	Potsdam
Laser frequency	ν	Hz	$1.922 \cdot 10^{14}$	$2.81 \cdot 10^{14}$	$2.81 \cdot 10^{14}$	$5.63 \cdot 10^{14}$
Receiver area	A_r	cm ²	1038.84	294.52	17671.46	1344.76
Receiver field of view	Ω_r	sr	$2.5 \cdot 10^{-9}$	$2.5 \cdot 10^{-9}$	$2.5 \cdot 10^{-9}$	$2.5 \cdot 10^{-9}$
Receiver optics efficiency	η_r	-	0.7	0.1	0.87	0.4
Detector quantum efficiency	η_d	-	0.8	0.3	0.13	0.08
Background spectral radiance	N_l	W nm ⁻¹ sr ⁻¹ cm ⁻²	$9.44 \cdot 10^{10}$	$9.44 \cdot 10^{10}$	$9.44 \cdot 10^{10}$	$9.44 \cdot 10^{10}$
Background photo-electron rate	Λ	s ⁻¹	10782.77	111.69	25266.45	272

Consequently, the background photon count within the detector during both daylight and nighttime is calculated using Equation 2.30 and Equation 2.31. A range gate window, τ_{rg} , of 1 μ s is implemented, which corresponds to an expected orbit prediction model accuracy of ± 150 m. Additionally, an integration time, τ_i , equal to the pulse length of the station, is used.

Imposing a probability of false alarm, P_{fa} , below 2%, as required by REQ-SYS-3, enables the calculation of the minimum photo-electron threshold, n_t . This threshold is computed using Equation 2.32 and represents the number of detected photons required for a signal to be deemed valid. Figure 5.9 provides insight into the behavior of the probability of false alarm in relation to the minimum photo-electron threshold. As depicted, the probability of false alarm decreases significantly beyond a certain value of n_t , reaching a value below 2% at $n_t = 17$ in this case. However, increasing the threshold beyond this point yields diminishing returns, as the curve flattens and further gains in probability of false alarm reduction become negligible.

**Figure 5.9:** Probability of false alarm as a function of detection threshold.**Figure 5.10:** Probability of detection as a function of the receiving mean signal photo-electron.

Considering that the probability of detection, P_d , must be greater than 99%, as required by REQ-SYS-4, the photon count of the received signal, N , is calculated using Equation 2.34. The receiving signal, N , is considered as the sum of the mean number of returning photo-electrons and the background noise photons. Figure 5.10 shows the behavior of the probability of detection as a function of the mean number of returning photo-electrons. As illustrated, increasing N beyond the point where the probability of detection exceeds 99% offers no significant benefit, again due to the curve flattening.

Lastly, the mean number of returning photo-electrons, n_{pe} , is calculated with Equation 2.33. However, if the integration time is not equal to the pulse length, t_s , the returning signal must be considered as the fraction that enters the integration window, as shown in Equation 5.2. Since, in this case, the integration time is equal to the pulse length, $\tau_i = t_s$.

$$n_{pe} = \begin{cases} (N - N_{b_i}) \cdot \frac{t_s}{\tau_i} & \text{if } \tau_i < t_s \\ (N - N_{b_i}) & \text{if } \tau_i \geq t_s \end{cases} \quad (5.2)$$

This process was repeated for all the stations under consideration. Table 5.6 and Table 5.7 list the required mean number of returning photo-electrons necessary to close the link budget for both daytime and nighttime conditions, respectively. Additionally, the intermediate variables used in the calculations are also included.

Table 5.6: Required mean number of returning photo-electrons during daytime and its components for each considered station.

Variable	Symbol	Unit	Delft Lasercom	Mini-SLR	Matera	Potsdam
Background photo-electron rate	Λ	s^{-1}	$37.7 \cdot 10^6$	$82.8 \cdot 10^4$	$18.7 \cdot 10^7$	$46.1 \cdot 10^5$
Range gate time window	τ_{rg}	s	$1 \cdot 10^{-6}$	$1 \cdot 10^{-6}$	$1 \cdot 10^{-6}$	$1 \cdot 10^{-6}$
Photon count within range gate	$N_{b_{rg}}$	-	37.69	0.83	187.34	4.61
Integration time	τ_i	s	$33.3 \cdot 10^{-9}$	$4 \cdot 10^{-9}$	$50 \cdot 10^{-12}$	$50 \cdot 10^{-12}$
Photon count within integration time	N_{b_i}	-	1.25	0.0033	0.0093	0.00023
Probability of false alarm	P_{fa}	-	1.04%	0.27%	0.81%	0.1%
Optimum detection threshold	n_t	-	8	2	3	2
Probability of detection	P_d	-	99%	99%	99%	99%
Required mean number of returning photo-electrons	n_{pe}	-	14.74	6.69	8.49	6.69

Table 5.7: Required mean number of returning photo-electrons during nighttime and its components for each considered station.

Variable	Symbol	Unit	Delft Lasercom	Mini-SLR	Matera	Potsdam
Background photo-electron rate	Λ	s^{-1}	10782.77	111.69	25266.45	272
Range gate time window	τ_{rg}	s	$1 \cdot 10^{-6}$	$1 \cdot 10^{-6}$	$1 \cdot 10^{-6}$	$1 \cdot 10^{-6}$
Photon count within range gate	$N_{b_{rg}}$	-	0.01	$1.1 \cdot 10^{-4}$	0.025	$2.7 \cdot 10^{-4}$
Integration time	τ_i	s	$33.3 \cdot 10^{-9}$	$4 \cdot 10^{-9}$	$50 \cdot 10^{-12}$	$50 \cdot 10^{-12}$
Photon count within integration time	N_{b_i}	-	$3.59 \cdot 10^{-4}$	$4.46 \cdot 10^{-7}$	$1.26 \cdot 10^{-6}$	$1.36 \cdot 10^{-8}$
Probability of false alarm	P_{fa}	-	1.072%	0.011%	$3.19 \cdot 10^{-6}\%$	0.027%
Optimum detection threshold	n_t	-	1	1	2	1
Probability of detection	P_d	-	99.1%	99.1%	99.05%	99.1%
Required mean number of returning photo-electrons	n_{pe}	-	4.69	4.69	6.69	4.69

As can be seen, during daylight, Delft laser communication station requires the highest mean number of returning photons, n_{pe} , to detect the signal. This is primarily because the assumed detector quantum efficiency, η_d , is the highest among the stations, and the longer assumed integration time, τ_i , leads to the background photo-electron count, N_{b_i} , being 3 to 4 orders of magnitude higher than at the other stations.

During nighttime, however, the required mean number of returning photo-electrons, n_{pe} , is largely stable across the stations. This is due to the fact that the background spectral radiance, N_l , is considered the same for all stations. Nevertheless, the background photo-electron rate, Λ , is two orders of magnitude higher for the Delft and Matera stations. Despite this, the behavior of the probability of false alarm, P_{fa} , results in an optimal detection threshold, n_t , between 1 and 2 for all stations, leading to a similar required mean number of returning photo-electrons across them. However, the probability of false alarm differs significantly between the stations due to shifts in the exponential behavior of the false alarm probability

curve. Specifically, Delft laser communication station has the highest P_{fa} , while Matera has the lowest, with a difference of six orders of magnitude.

With the required mean number of returning photo-electrons determined for each station, the link budget analysis can be performed, as the required strength of the returning signal is set.

5.4. Retroreflector radius

After calculating the required number of returning photons per station during both daylight and nighttime, the link budget analysis can be performed. This analysis follows the approach discussed in subsection 3.2.2, where different retroreflector radii are applied per station, and the OCS response within the velocity aberration constraints is checked to ensure it exceeds the threshold.

5.4.1. Case scenario

To perform the simulation, a case scenario is created. Table 5.8 shows the values of the main variables used to define the case study, which determines the retroreflector radius range for each station.

Table 5.8: Case scenario settings

Simulation settings	
Minimum elevation angle	20°
AOI range	0° - 42°
Satellite settings	
Satellite altitude	525 km
Retroreflector settings	
Reflectivity	0.85
Index of refraction	1.461
Retroreflector ratio	$\sqrt{2}$
Atmospheric condition	
Two-way atmospheric attenuation factor	0.8
Two-way cirrus clouds attenuation factor	0.8

The minimum elevation angle was set based on observations retrieved in chapter 4. It is important to note that ground stations have a defined range of elevation angles they can use for laser ranging, which is constrained by their surroundings, such as mountains, tall buildings, or nearby airports. Therefore, the minimum elevation angle varies depending on the specific ground station. A commonly used value for the minimum elevation angle in literature is 40° [28]. However, during the verification of the PoV simulation, it was observed that Graz station began tracking the satellite launched by Astrocass around 40°, but followed it as low as 16.77° of elevation. Given this observation, it is clear that using a minimum elevation angle of 0° would not make sense, as stations cannot track satellites at the horizon. However, observations may begin at around 20° of elevation. As a result, 20° was selected as the minimum elevation angle. This variable significantly affects the link budget, as lower elevation angles increase the slant range between the satellite and the ground station. Closing the link budget at the minimum elevation angle ensures that the link will also close at higher elevations, as the minimum elevation represents the worst-case scenario in terms of slant range.

The range of AOI is based on the visibility definition generated in subsection 3.2.1. The retroreflector settings are based on the preferred model from Edmund Optics, as listed in Table 2.6. Reflectivity is taken as the average value over the 400-700 nm wavelength range, as specified in the Edmund Optics data sheet [40]. However, this reflectivity must be verified through testing of the purchased retroreflectors. Furthermore, the satellite altitude is taken as the predicted value of Delfi-Twin, and atmospheric conditions are assumed to be clear skies, as laser ranging measurements are ideally conducted under such conditions.

5.4.2. Radius range convergence

Now that the case scenario is generated, the link budget analysis is performed for each station during both daytime and nighttime. Table 5.9 and Table 5.10 show the range of radii where the OCS response exceeds the threshold within the velocity aberration constraints. Additionally, the required mean number of returning photons, the minimum elevation angle considered, and the AOI range are included for reference. The range of retroreflector radii tested in the simulation was from 0.1 to 20 mm.

Table 5.9: Converging retroreflector radius range per station during daylight.

Parameters	Symbol	Delft Lasercom	Mini-SLR	Matera	Potsdam
Required mean number of returning photo-electrons	n_{pe}	14.74	6.69	8.49	6.69
Minimum elevation angle	$\alpha_{e_{min}}$	20°	20°	20°	20°
AOI range	-	0°- 42°	0°- 42°	0°- 42°	0°- 42°
Retroreflector radius range	-	N/A	N/A	6.1 - 12 mm	N/A

Table 5.10: Converging retroreflector radius range per station during nighttime.

Parameters	Symbol	Delft Lasercom	Mini-SLR	Matera	Potsdam
Required mean number of returning photo-electrons	n_{pe}	4.69	4.69	6.69	4.69
Minimum elevation angle	$\alpha_{e_{min}}$	20°	20°	20°	20°
AOI range	-	0°- 42°	0°- 42°	0°- 42°	0°- 42°
Retroreflector radius range	-	N/A	N/A	5.7 - 12 mm	N/A

As can be seen, the Matera station is the only station with a range of retroreflector radii that successfully closes the link budget for both daylight and nighttime conditions. The other stations do not provide sufficient power to close the link budget, thereby failing to maintain the OCS response above the threshold within the velocity aberration range for the implemented AOI values.

This means that coupling the Matera station with a retroreflector array composed of retroreflectors within the derived radius range can close the link budget. This makes it possible to achieve the PoV defined in chapter 4 of 81.55% for attitude 3 when using the 8 retroreflector array configuration. Furthermore, starting the tracking at an elevation of 20° ensures a sufficiently long laser ranging time window, allowing the collection of more observations and thus improving measurement accuracy. For example, a pass of Delfi-Twin at a 90° inclination with respect to the Matera station provides a time window of approximately 309 s.

In Figure 5.11 and Figure 5.12, the OCS responses for retroreflector radii of 6.1 mm and 12 mm are shown for daylight conditions. It can be observed that the OCS responses are above the threshold within the velocity aberration range, represented by the grey shaded area in the graphs.

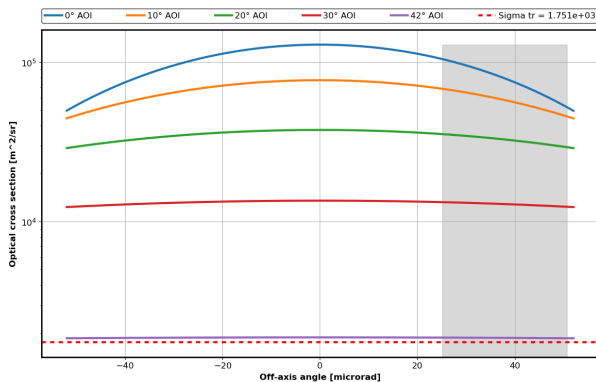


Figure 5.11: OCS w.r.t. off-axis angle for different AOI with radius 6.1 mm at 40° elevation using Matera during daylight.

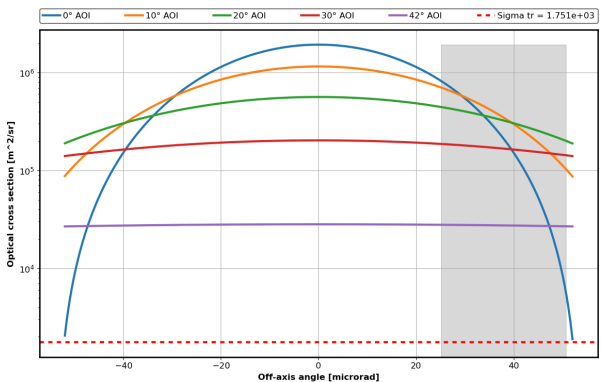


Figure 5.12: OCS w.r.t. off-axis angle for different AOI with radius 12 mm at 40° elevation using Matera during daylight.

While it might seem counterintuitive to have a maximum radius in the effective range, the Bessel behavior of the OCS increases with the retroreflector radius, resulting in multiple dips within the velocity

aberration range. This phenomenon prevents the link budget from being closed effectively. This Bessel behavior is evident in the figures, where the OCS for the 12 mm radius retroreflector shows more pronounced dips compared to the 6.1 mm radius retroreflector.

5.4.3. Radius range convergence with modified AOI

Even though the link budget could not be closed for stations other than the Matera one in the given scenario, it is possible to relax some constraints in the case study. Specifically, the AOI range can be adjusted by increasing the lower limit. As discussed in subsection 2.3.4 and shown in Figure 5.11 and Figure 5.12, targeting the retroreflector at a low AOI increases the overall OCS magnitude for on-axis reflections. However, as the off-axis angle increases, the Bessel behavior becomes more pronounced at these lower AOI values. Therefore, by increasing the lower limit of the AOI range, it is possible to reduce the number of dips within the velocity aberration region.

Nevertheless, this adjustment affects the PoV achieved with the retroreflector array. Specifically, if the definition of visibility is modified to consider a smaller AOI range, the resulting PoV decreases because there are fewer instances where the retroreflector array is visible.

The overall average and standard deviation values of PoV for smaller AOI ranges are provided in Table 5.11, based on attitude 3 with the 8 retroreflector array configuration. Figure 5.13 displays the different PoV curves per elevation angle with a smaller AOI range for the considered case.

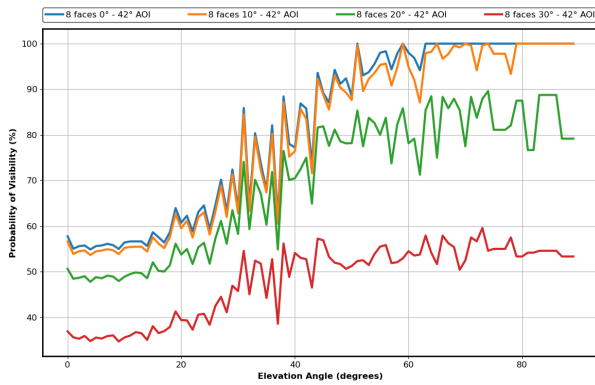


Figure 5.13: PoV curve per elevation angle with decreasing AOI range for attitude 3 with the 8 retroreflector array configuration

Table 5.11: PoV values at different AOI ranges for attitude 3 with the 8 retroreflector array configuration

AOI range	Probability of Visibility	
	Avg	Std
0° - 42°	81.55%	1.12%
10° - 42°	80.11%	0.99%
20° - 42°	69.90%	1.70%
30° - 42°	48.08%	2.01%

As expected, the PoV drastically diminishes when the AOI range is reduced, as fewer instances where the satellite is visible occur. Based on the retrieved data, it was found that increasing the lower end of the AOI range beyond 20° results in an insufficient PoV, falling below 70%, which limits the collection of laser ranging data points. Therefore, the link budget simulation is rerun, increasing the lower end of the AOI range to 20° for each station, in order to determine a retroreflector radius range that closes the link budget. The values for the Matera station were not recomputed, as convergence was already achieved in the original case study. The results are collected in Table 5.12 and Table 5.13 for daylight and nighttime respectively.

Table 5.12: Converging retroreflector radius range per station during daylight with limited AOI.

Parameters	Symbol	Delft Lasercom	Mini-SLR	Matera	Potsdam
Required mean number of returning photo-electrons	n_{pe}	14.74	6.69	8.49	6.69
Minimum elevation angle	$\alpha_{e_{min}}$	20°	20°	20°	20°
AOI range	-	20° - 42°	20° - 42°	0° - 42°	20° - 42°
Retroreflector radius range	-	N/A	N/A	6.1 - 12 mm	N/A

Table 5.13: Converging retroreflector radius range per station during nighttime with limited AOI.

Parameters	Symbol	Delft Lasercom	Mini-SLR	Matera	Potsdam
Required mean number of returning photo-electrons	n_{pe}	4.69	4.69	6.69	4.69
Minimum elevation angle	$\alpha_{e_{min}}$	20°	20°	20°	20°
AOI range	-	20°- 42°	20°- 42°	0°- 42°	20°- 42°
Retroreflector radius range	-	N/A	N/A	5.7 - 12 mm	N/A

As can be observed from the results, reducing the AOI range still did not result in convergence for the other stations. The remaining variable that can be adjusted to attempt closing the link budget is the minimum elevation angle.

5.4.4. Radius range convergence with modified minimum elevation angle

Another constraint that can be relaxed is the minimum elevation angle. This variable significantly affects the link budget, as a lower minimum elevation angle results in a larger slant range. In the case study, 20° was selected due to observations made during the verification of the probability of visibility simulation. If the minimum elevation angle is increased, the time window available for collecting laser ranging measurements decreases, which reduces the number of data points collected per satellite pass within the station FoV, thereby decreasing the accuracy of ranging.

To explore this, the link budget simulation is rerun while keeping the original AOI range, but increasing the minimum elevation angle until convergence is achieved for a range of retroreflector radii. Ideally, the minimum elevation angle should be kept below 40°, as this is considered the standard maximum value for laser ranging measurements. If convergence cannot be achieved below this value, increasing the elevation angle further would limit the time window excessively, making it impossible to collect enough observations per pass. Table 5.14 and Table 5.15 display the results obtained for the link budget simulation with the modified minimum elevation angle during daytime and nighttime respectively.

Table 5.14: Converging retroreflector radius range per station during daylight with limited minimum elevation angle.

Parameters	Symbol	Delft Lasercom	Mini-SLR	Matera	Potsdam
Required mean number of returning photo-electrons	n_{pe}	14.74	6.69	8.49	6.69
Minimum elevation angle	$\alpha_{e_{min}}$	40°	40°	20°	40°
AOI range	-	0°- 42°	0°- 42°	0°- 42°	0°- 42°
Retroreflector radius range	-	N/A	N/A	6.1 - 12 mm	N/A

Table 5.15: Converging retroreflector radius range per station during nighttime with limited AOI and minimum elevation angle.

Parameters	Symbol	Delft Lasercom	Mini-SLR	Matera	Potsdam
Required mean number of returning photo-electrons	n_{pe}	4.69	4.69	6.69	4.69
Minimum elevation angle	$\alpha_{e_{min}}$	40°	40°	20°	40°
AOI range	-	0°- 42°	0°- 42°	0°- 42°	0°- 42°
Retroreflector radius range	-	N/A	N/A	5.7 - 12 mm	N/A

As can be observed from the results, increasing the minimum elevation angle still did not result in convergence for the other stations. A combination of an increase in minimum elevation angle and decrease of the AOI range can still be performed to attempt closing the link budget.

5.4.5. Radius range convergence with combined modifications

To achieve convergence for a range of retroreflector radii for the other stations, the minimum elevation angle is increased together with decreasing the AOI range. Table 5.16 and Table 5.17 display the results obtained for the link budget simulation with the aforementioned modifications during daytime and nighttime respectively.

Table 5.16: Converging retroreflector radius range per station during daylight with limited minimum elevation angle.

Parameters	Symbol	Delft Lasercom	Mini-SLR	Matera	Potsdam
Required mean number of returning photo-electrons	n_{pe}	14.74	6.69	8.49	6.69
Minimum elevation angle	α_{emin}	40°	40°	20°	30°
AOI range	-	20° - 42°	20° - 42°	0° - 42°	20° - 42°
Retroreflector radius range	-	N/A	N/A	6.1 - 12 mm	8.7 - 9.5 mm

Table 5.17: Converging retroreflector radius range per station during nighttime with limited AOI and minimum elevation angle.

Parameters	Symbol	Delft Lasercom	Mini-SLR	Matera	Potsdam
Required mean number of returning photo-electrons	n_{pe}	4.69	4.69	6.69	4.69
Minimum elevation angle	α_{emin}	40°	40°	20°	25°
AOI range	-	20° - 42°	20° - 42°	0° - 42°	20° - 42°
Retroreflector radius range	-	N/A	N/A	5.3 - 12 mm	9.0 - 9.3 mm

As observed, convergence is achieved for the Potsdam station. During daylight, Potsdam can track a retroreflector with a radius between 8.7 mm and 9.5 mm from a minimum elevation angle of 30°, provided that the AOI range is maintained between 20° and 42°. This results in a PoV of 69.9%, as shown in Table 5.11, considering attitude 3 with the 8 retroreflector array configuration for a time window of 258 s if the satellite passes at an inclination angle of 90° with respect to the station.

During nighttime, the Potsdam station can track a retroreflector with a radius between 9 mm and 9.3 mm from a minimum elevation angle of 25°, assuming the AOI range is kept between 20° and 42°. This also results in a PoV of 69.9%, as shown in Table 5.11, for attitude 3 with the 8 retroreflector array configuration, leading to a time window of 217 s for a pass at an inclination angle of 90° with respect to the station.

5.4.6. Radius selection

Considering the preferred choice of retroreflectors from Edmund Optics, the available diameters are 7.16 mm, 12.7 mm, 25.4 mm, and 50.8 mm. The only diameter that fits within the retroreflector radius range converging for the Matera station is the 12.7 mm diameter option. However, this retroreflector is not within the convergence range obtained for the Potsdam station. Nevertheless, the original case study constraints can still be relaxed to achieve a broader range of convergence for Potsdam. Table 5.18 presents the modified converging retroreflector radius range for Potsdam, for which the 12.7 mm diameter retroreflector fits.

Table 5.18: Converging retroreflector radius range increase for Potsdam station during daytime and nighttime.

Parameters	Symbol	Potsdam Day	Potsdam Night
Required mean number of returning photo-electrons	n_{pe}	6.69	4.69
Minimum elevation angle	α_{emin}	50°	40°
AOI range	-	10° - 42°	10° - 40°
Retroreflector radius range	-	6.0 - 7.1 mm	5.8 - 6.9 mm

For daytime conditions, the convergence range is obtained for a minimum elevation angle of 50°, which exceeds the previously set limit of 40°. However, since laser ranging measurements are typically performed during nighttime, the requirement to fit the available diameters within Potsdam's daylight range can be disregarded. During nighttime, the converging retroreflector range that accommodates the available retroreflector diameter is achieved for a minimum elevation angle of 40°, while the AOI range was reduced to 10° and 40°. In this case, the upper limit had to be decreased because the overall OCS response magnitude at higher AOI values was too low to support a minimum elevation angle below 40°.

This adjustment in the AOI range reduces the PoV to 76.88% with a standard deviation of 1.16% for attitude 3 with the 8 retroreflector array configuration, as shown in the PoV curve plotted in Figure 5.14 for the considered AOI range. The achieved PoV is above the previously set limit of 70%.

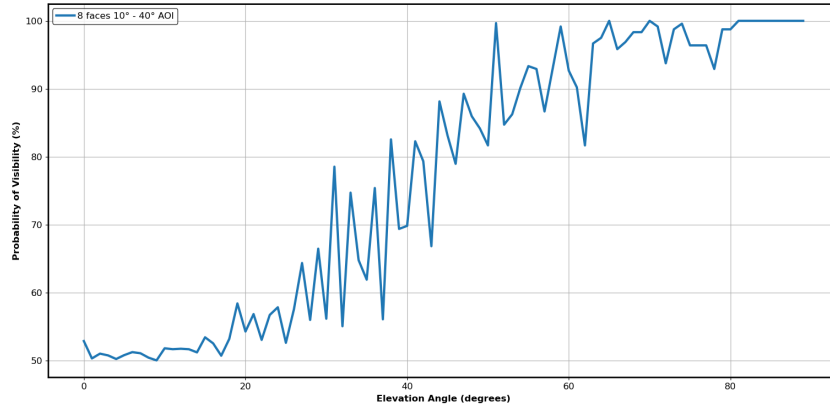


Figure 5.14: PoV curve per elevation angle with AOI range between 10° and 40° for attitude 3 with the 8 retroreflector array configuration

Based on this analysis, the retroreflector from Edmund Optics with a diameter of 12.7 mm is selected as the most suitable option for implementation in the retroreflector array of Delfi-Twin. Figure 5.15 and Figure 5.16 show the OCS response of the selected retroreflector size coupled with Matera and Potsdam respectively during nighttime with the considered relaxed constraints.

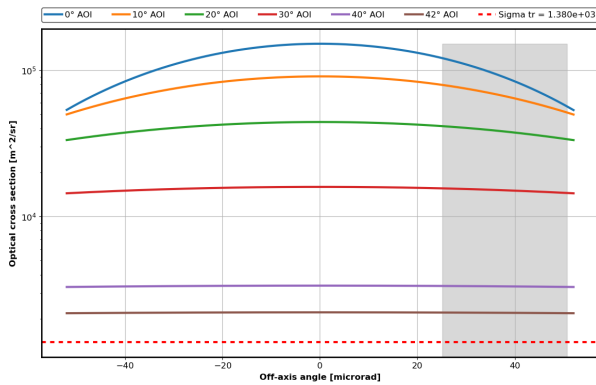


Figure 5.15: OCS w.r.t. off-axis angle for different AOI with diameter 12.7 mm at 20° elevation using Matera during nighttime.

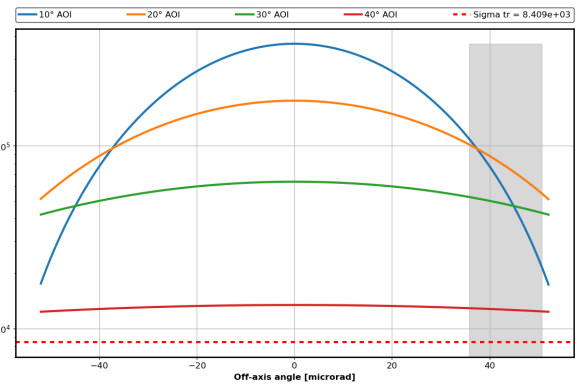


Figure 5.16: OCS w.r.t. off-axis angle for different AOI with diameter 12.7 mm at 40° elevation using Potsdam during nighttime.

5.5. Sensitivity Analysis

To gain insights into how different parameters affect the link budget, a sensitivity analysis is performed. First, the elevation angle at which the link budget is evaluated and the AOI of the laser on the retroreflector are investigated. In Table 5.19, six different cases are presented in which the link budget was performed using the Potsdam station during nighttime. The retroreflector settings and atmospheric conditions remain consistent with the original case study, while the elevation angle is varied from 20° to 60°, and the AOI changes per case. The table shows the generated OCS and the returning photon count. The cells containing the photon count are color-coded: red when the returning photon count is below the threshold of 4.69, as defined in section 5.3, and green when it exceeds the threshold.

Table 5.19: Elevation and angle of incidence variations in returning photon count for Potsdam.

Parameter	Symbol	Unit	Case 1	Case 2	Case 3	Case 4	Case 5	Case 6
Elevation angle	α_e	°	20°	30°	30°	40°	60°	60°
Off-axis angle	θ_r	μrad	40	40	40	40	48	48
Angle of incidence	θ_i	°	30°	30°	40°	40°	40°	20°
Retroreflector radius	r_{cc}	mm	6.35	6.35	6.35	6.35	6.35	6.35
Reflectivity	ρ	-	0.85	0.85	0.85	0.85	0.85	0.85
Two-way atmospheric attenuation factor	T_a^2	-	0.8	0.8	0.8	0.8	0.8	0.8
Two-way cirrus cloud attenuation factor	T_c^2	-	0.8	0.8	0.8	0.8	0.8	0.8
Optical Cross Section	σ	m^2/sr	$5.002 \cdot 10^4$	$5.002 \cdot 10^4$	$1.280 \cdot 10^4$	$1.280 \cdot 10^4$	$1.252 \cdot 10^4$	$6.281 \cdot 10^4$
Returning photon count	n_{pe}	-	4.25	12.4	3.17	7.14	19.79	99.26

As can be observed from the table, increasing the elevation angle results in a higher returning photon count. This is expected, as the slant range decreases with increasing elevation. Additionally, a lower AOI produces a higher OCS response, leading to an increased returning photon count, provided that the Bessel behavior is not predominant within the velocity aberration range. It is noteworthy that case 2 closes the link budget, despite being at a lower elevation angle than the converging condition achieved in subsection 5.4.6. This is expected, as the AOI considered is lower than the desired upper bound. In contrast, case 3, which implements the same 30° elevation but with a higher AOI of 40° , does not close the link. This demonstrates that the link can be closed at lower elevations when the AOI is lower. However, fewer instances where this occurs during a pass are available, reducing the overall PoV below the 70% limit.

Another important parameter to investigate are the atmospheric conditions, specifically the two-way atmospheric and cirrus cloud attenuation factors. In Table 5.20, the same cases as before were considered, but the attenuation factors were both reduced to 0.5, representing non-clear sky conditions.

Table 5.20: Atmospheric conditions variations in returning photon count for Potsdam.

Parameter	Symbol	Unit	Case 1	Case 2	Case 3	Case 4	Case 5	Case 6
Elevation angle	α_e	$^\circ$	20°	30°	30°	40°	60°	60°
Off-axis angle	θ_r	μrad	40	40	40	40	48	48
Angle of incidence	θ_i	$^\circ$	30°	30°	40°	40°	40°	20°
Retroreflector radius	r_{cc}	mm	6.35	6.35	6.35	6.35	6.35	6.35
Reflectivity	ρ	-	0.85	0.85	0.85	0.85	0.85	0.85
Two-way atmospheric attenuation factor	T_a^2	-	0.5	0.5	0.5	0.5	0.5	0.5
Two-way cirrus cloud attenuation factor	T_c^2	-	0.5	0.5	0.5	0.5	0.5	0.5
Optical Cross Section	σ	m^2/sr	$5.002 \cdot 10^4$	$5.002 \cdot 10^4$	$1.280 \cdot 10^4$	$1.280 \cdot 10^4$	$1.252 \cdot 10^4$	$6.281 \cdot 10^4$
Returning photon count	n_{pe}	-	1.66	4.84	1.24	2.79	7.73	38.77

As observed from the table, the returning photon count in each case decreased by more than 50%. This was expected, as worse atmospheric conditions result in greater atmospheric losses and a weaker returning laser pulse. This is why laser ranging measurements are preferably conducted under clear skies to minimize power losses.

Another parameter that was adjusted in the link budget analysis is the altitude of the satellite. Although Delfi-Twin is expected to orbit at 525 km above sea level, inaccuracies during orbit injection could result in a higher altitude. In Table 5.21, an altitude of 600 km was considered.

Table 5.21: Variations in returning photon count for Potsdam with satellite altitude set to 600 km.

Parameter	Symbol	Unit	Case 1	Case 2	Case 3	Case 4	Case 5	Case 6
Elevation angle	α_e	$^\circ$	20°	30°	30°	40°	60°	60°
Off-axis angle	θ_r	μrad	40	40	40	40	48	48
Angle of incidence	θ_i	$^\circ$	30°	30°	40°	40°	40°	20°
Retroreflector radius	r_{cc}	mm	6.35	6.35	6.35	6.35	6.35	6.35
Reflectivity	ρ	-	0.85	0.85	0.85	0.85	0.85	0.85
Two-way atmospheric attenuation factor	T_a^2	-	0.5	0.5	0.5	0.5	0.5	0.5
Two-way cirrus cloud attenuation factor	T_c^2	-	0.5	0.5	0.5	0.5	0.5	0.5
Optical Cross Section	σ	m^2/sr	$5.002 \cdot 10^4$	$5.002 \cdot 10^4$	$1.280 \cdot 10^4$	$1.280 \cdot 10^4$	$1.252 \cdot 10^4$	$6.281 \cdot 10^4$
Returning photon count	n_{pe}	-	2.7	7.6	1.94	4.28	11.67	58.55

As expected, fewer returning photons are calculated for the same case scenarios considered before. It is interesting to note that Case 4, which falls within the convergence boundaries selected for Potsdam in subsection 5.4.6, does not close the link at an altitude of 600 km. This highlights the fact that inaccuracies in orbit injection could result in a lower PoV for the satellite array.

5.5.1. Reflectivity

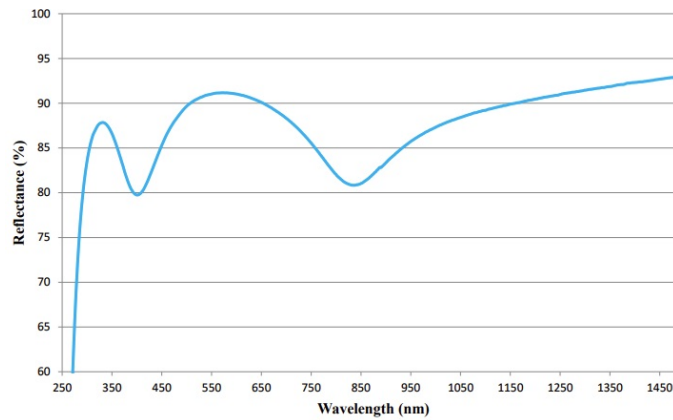
One of the most important parameters in the link budget analysis is the retroreflector reflectivity. Since the batch of retroreflectors to be acquired by the DSE is limited relatively to what suppliers typically provide, these retroreflectors will likely be sourced from available stock in the supplier warehouse. This may result in retroreflectors with reduced performance, particularly lower reflectivity. In Table 5.22, the reflectivity has been adjusted for the previously considered cases. When the link was not closed, the reflectivity was increased. For cases where the link closed, the reflectivity was decreased.

Table 5.22: Reflectivity variations in returning photon count for Potsdam.

Parameter	Symbol	Unit	Case 1	Case 2	Case 3	Case 4	Case 5	Case 6
Elevation angle	α_e	°	20°	30°	30°	40°	60°	60°
Off-axis angle	θ_r	μrad	40	40	40	40	48	48
Angle of incidence	θ_i	°	30°	30°	40°	40°	40°	20°
Retroreflector radius	r_{cc}	mm	6.35	6.35	6.35	6.35	6.35	6.35
Reflectivity	ρ	-	0.95	0.75	0.95	0.75	0.65	0.65
Two-way atmospheric attenuation factor	T_a^2	-	0.8	0.8	0.8	0.8	0.8	0.8
Two-way cirrus cloud attenuation factor	T_c^2	-	0.8	0.8	0.8	0.8	0.8	0.8
Optical Cross Section	σ	m^2/sr	$5.591 \cdot 10^4$	$4.414 \cdot 10^4$	$1.431 \cdot 10^4$	$1.130 \cdot 10^4$	$9.576 \cdot 10^4$	$4.803 \cdot 10^4$
Returning photon count	n_{pe}	-	4.74	10.94	3.54	6.30	15.13	75.90

As can be observed, increasing the reflectivity results in a higher returning photon count, and vice versa. The percentage change in reflectivity is directly proportional to the number of returning photons.

For the link budget analysis, a reflectivity of 0.85 was considered. This value represents the average reflectivity between the 400 nm and 700 nm range for the retroreflector provided by Edmund Optics, as shown in Figure 5.17.

**Figure 5.17:** Aluminum coated typical reflectance performance over wavelength [40].

As observed from the plot in Figure 5.17, for wavelengths greater than 850 nm, the reflectivity tends to increase with wavelength. However, due to the potential risk of lower performance from the acquired retroreflectors, a minimum reflectivity requirement must be defined to select retroreflectors suitable for the Delfi-Twin array. To address this, the link budget analysis was rerun by gradually lowering the reflectivity of the retroreflector until the selected retroreflector radius no longer fell within the converging range of radii for the ground stations. Table 5.23 displays the converging radius range for Matera and Potsdam stations at a retroreflector reflectivity of 57%.

Table 5.23: Converging retroreflector radius range per station during nighttime with limited AOI and minimum elevation angle and reflectivity of 57%.

Parameters	Symbol	Matera	Potsdam
Required mean number of returning photo-electrons	n_{pe}	6.69	4.69
Minimum elevation angle	$\alpha_{e_{min}}$	20°	40°
AOI range	-	0° - 42°	10° - 40°
Retroreflector radius range	-	6.3 - 11.9 mm	6.4 - 6.6 mm

From the table, it can be concluded that Potsdam station will not be able to perform laser ranging measurements with the selected retroreflector radius at a reflectivity of 57%, as the radius is just below the lower bound of the convergence range. While the Matera station is still capable, as the lower bound is 0.5 mm below the selected radius. As a result, 57% reflectivity is considered the lower limit for retroreflector reflectivity.

Since the actual altitude of Delfi-Twin might be higher than assumed in the link budget analysis, and the effective radius of the retroreflector could be slightly reduced due to the overlap of the holder mechanism on the reflective surface, a margin must be applied to the reflectivity limit. A 20% margin is considered acceptable, leading to a reflectivity limit of 68.4%.

The conducted analysis establishes the following requirement for the retroreflectors:

REQ-RT-1: The retroreflector shall have a reflectivity greater than 68.4% for the implemented ground station wavelengths of 532 nm, 1064 nm, and 1560 nm.

5.6. Delft Lasercomm Station Recommendations

As demonstrated in this chapter, the laser pulse power of the communication station on top of the Aerospace building at TU Delft is insufficient to achieve convergence for the selected retroreflector radius, making laser ranging impossible with the current setup.

Nevertheless, the link budget analysis was rerun for the Delft station to assess the laser power required to achieve ranging with the selected array configuration. Table 5.24 lists the converging radii for a pulse laser power of 25 kW in the original scenario and 2.4 kW in the relaxed scenario, where Potsdam achieved convergence. As shown, with this level of laser power, ranging becomes feasible with the selected retroreflector.

Table 5.24: Converging retroreflector radius range for Delft laser communication station during daytime and nighttime for an increased laser power.

Parameters	Symbol	Delft Lasercom $P_{laser} = 25\text{kW}$	Delft Lasercom $P_{laser} = 2.4\text{kW}$
Required mean number of returning photo-electrons	n_{pe}	4.69	4.69
Minimum elevation angle	$\alpha_{e_{min}}$	20°	40°
AOI range	-	0° - 42°	10° - 40°
Retroreflector radius range	-	6.3 - 17.9 mm	6.3 - 20 mm

The considered laser pulse powers, 25 kW and 2.4 kW, coupled with the assumed laser pulse width of $33.3 \cdot 10^{-9}$ s, generated pulse energies of $8.325 \cdot 10^{-4}$ J and $7.99 \cdot 10^{-5}$ J, respectively. If the actual power of the laser at Delft station remains unchanged at 0.5 W, the required pulse energies could be achieved by increasing the laser pulse width, as shown in Equation 5.1. This adjustment results in laser pulse widths of $1.66 \cdot 10^{-3}$ s and $1.59 \cdot 10^{-4}$ s, corresponding to errors of 500 km and 47 km, respectively, in determining which photon within the pulse is the actual returning one, making laser ranging measurements unusable.

In conclusion, the current laser setup at the Delft station is insufficient to achieve effective satellite laser ranging with the selected retroreflector configuration. While adjustments to the pulse width could theoretically achieve the required pulse energy, the significant error in photon timing renders this approach impractical. Therefore, the only viable solution is to replace the existing laser with a more powerful one. Solid-state lasers with neodymium-doped yttrium aluminum garnet (Nd) as the lasing medium, are commonly used by ILRS stations, and could provide a viable option for the Delft station. Nevertheless, a proper trade-off analysis will be necessary to determine the best-fit laser for integration, balancing factors such as power, wavelength, and beam characteristics to ensure the link budget is met and successful laser ranging can be achieved.

6

Testing & Integration

This chapter presents the inspection performed on the ordered retroreflectors and the potential testing required for them. This process is crucial to qualify the retroreflectors for integration into the satellite array. In addition, the first iteration of the holder for integrating the array onto the satellite is also presented.

Section 6.1 discusses the inspection conducted and the defects identified in the retroreflectors. Section 6.2 outlines the tests to be performed to evaluate the retroreflector performance. Finally, section 6.3 presents the design of the holder for the retroreflector array.

6.1. Retroreflector Inspection

Following the analysis performed in the previous chapter, the DSE proceeded with the acquisition of 30 aluminum-coated fused silica corner cube retroreflectors with a 12.7 mm diameter from Edmund Optics [40]. Upon arrival, an inspection and cataloging of the retroreflectors were conducted to verify product quality and prepare for subsequent testing.

The retroreflector inspection took place in an ISO 8, Class 100,000 cleanroom on the 8th floor of the Aerospace Faculty building at TU Delft. Each retroreflector was unboxed and carefully inspected for any damage to the reflective surface or coating. At this stage, the retroreflectors were not thoroughly cleaned, however, tissues soaked in isopropyl alcohol were used to remove some dust particles to better identify potential damage.

The retroreflector catalog, built during the inspection, is presented in Table 6.1. Each retroreflector was assigned an ID starting with "RT-" followed by its specific number, as shown in the table. Furthermore, a retroreflector was considered qualified for the next stages (marked with ✓ in the table) if no damage was found on the reflective surface or coating. On the other hand, retroreflectors with identified damage were marked as not qualified (denoted by × in the table), with notes detailing the observed damage.

Out of the 30 retroreflectors, four were found to be damaged: RT-08, RT-18, RT-21, and RT-25. The damaged retroreflectors are shown in Figure 6.1, Figure 6.2, Figure 6.3, and Figure 6.4, respectively, with the identified damage circled in red. These retroreflectors were deemed not qualified for satellite deployment, even though it was not possible to fully assess how the damage would affect their performance. Instead, these retroreflectors will be retained by the DSE for potential ground testing and integration into other setups until the effects of the damage on their performance are quantified.

It may appear notable that 13.3% of the retroreflectors were damaged. However, this outcome is not entirely unexpected, considering that the ordered batch was relatively limited in size compared to what the suppliers usually provide. The retroreflectors sent were sourced from the available stock in their warehouses. For this reason, prior to integrating the retroreflectors into the satellite array, their performance must be tested, in addition to undergoing standard inspections.

Table 6.1: Retroreflector catalog.

ID	Qualified	Note
RT-01	✓	
RT-02	✓	
RT-03	✓	
RT-04	✓	
RT-05	✓	
RT-06	✓	
RT-07	✓	
RT-08	×	Bubble under the reflective surface
RT-09	✓	
RT-10	✓	
RT-11	✓	
RT-12	✓	
RT-13	✓	
RT-14	✓	
RT-15	✓	
RT-16	✓	
RT-17	✓	
RT-18	×	Crack on reflective surface
RT-19	✓	
RT-20	✓	
RT-21	×	Crack on reflective surface
RT-22	✓	
RT-23	✓	
RT-24	✓	
RT-25	×	Scratches inside the coating layer
RT-26	✓	
RT-27	✓	
RT-28	✓	
RT-29	✓	
RT-30	✓	



Figure 6.1: RT-08.

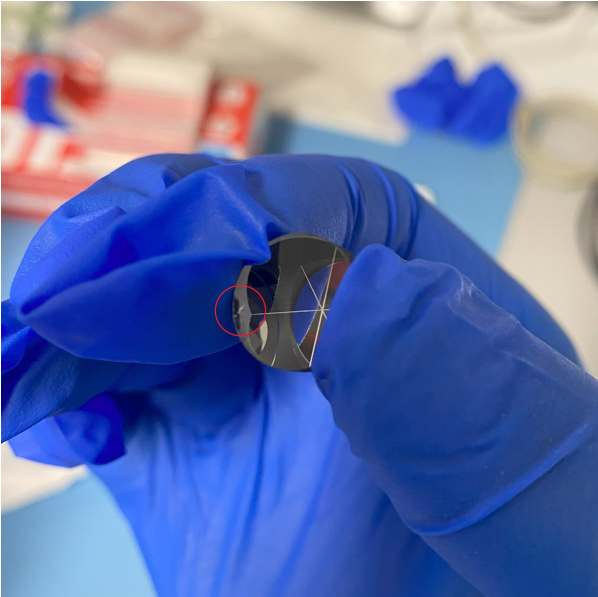


Figure 6.2: RT-18.

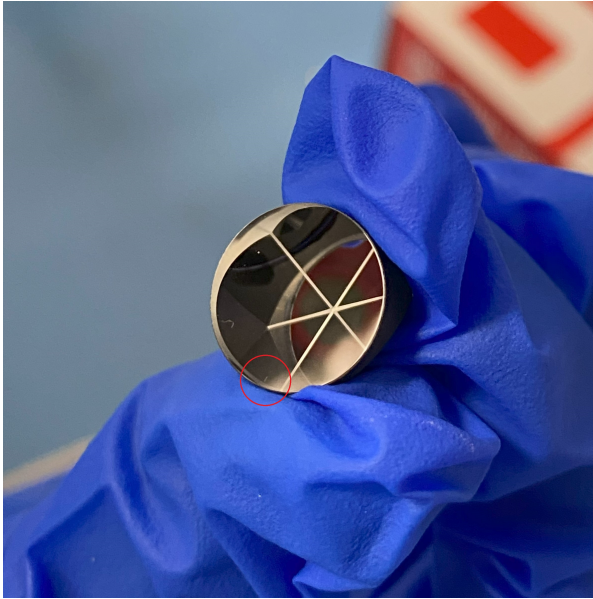


Figure 6.3: RT-21.

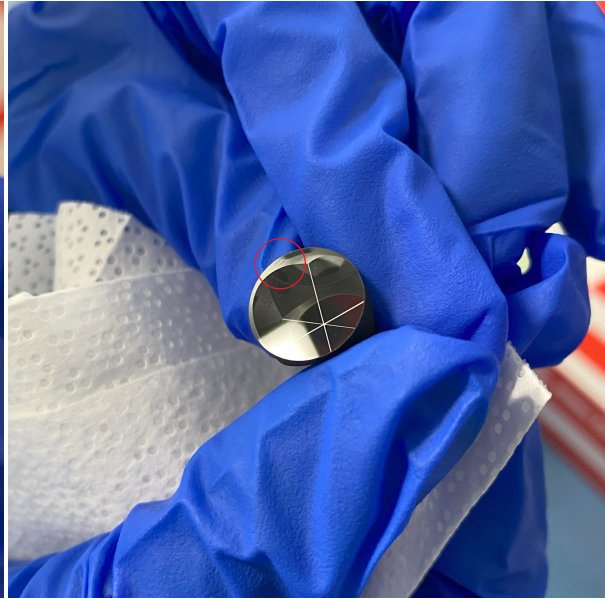


Figure 6.4: RT-25.

After the inspection, each retroreflector was wrapped in optical paper and placed inside a white protective bag, which was sealed in a plastic zip-lock with the respective identifier, as shown in Figure 6.5. Subsequently, the plastic zip-lock was placed inside the original box, as seen in Figure 6.6, ready for shipment to the testing location.

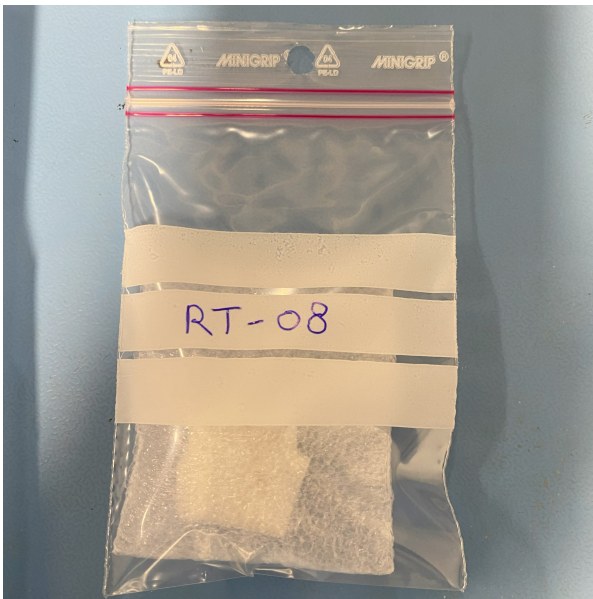


Figure 6.5: RT-08 sealed in a plastic zip-lock with its identifier.



Figure 6.6: Original box from Edmund Optics.

6.2. Retroreflector Testing

The tests to be performed will measure the optical performance of the retroreflectors, primarily focusing on reflectivity and AOI leakage.

As discussed in subsection 5.5.1, the retroreflectors must meet a reflectivity threshold of 68.4% to be qualified for integration into Delfi-Twin. Additionally, the analysis assumed that no leakage of the reflected signal would occur for AOI values below 42° . The testing will verify that these assumptions hold true for the acquired retroreflectors.

Since TU Delft does not currently have the necessary facilities to conduct these qualification tests, the SCF_Lab at INFN–LNF in Frascati, Italy, was contacted. Negotiations are underway to secure a testing window at this facility.

The SCF_Lab, active for about 15 years, specializes in the design, testing, and space qualification of advanced laser retroreflectors and laser-ranging systems. It includes an 85 m² class 10,000 cleanroom (ISO 7) with separate entry areas for operators and equipment [57]. The lab "SCF-Test" procedure is used to characterize and model the thermal behavior and optical performance of GNSS laser retroreflector arrays under space-simulated laboratory conditions [58].

Although this facility can also assess the thermal behavior of the retroreflectors, due to time constraints and limited availability, only optical performance tests will be conducted. Once the results are obtained a final selection will be made from the 26 retroreflectors that passed the inspection based on REQ-RT-1 generated in subsection 5.5.1.

6.3. Retroreflector holder

In this section, a preliminary design of the retroreflector holder for integration within Delfi-Twin is presented. However, before detailing the design, additional considerations need to be addressed. The DSE explored the possibility of installing four bolometers on Delfi-Twin to provide temperature measurements of the surrounding environment. Positioned around the rolling axis, with one on each of the four faces, these bolometers could supply data to assist in determining the satellite attitude. A higher temperature reading would be expected when a bolometer faces Earth compared to when it faces deep space, allowing this system to complement the retroreflector array in attitude determination. For this purpose, the far-infrared thermal sensor array MLX90640 from Melexis, with a FoV of 110°, was selected. These sensors have an operational temperature range of -40°C to 85°C and can measure object temperatures between -40°C and 300°C with an accuracy of $\pm 1^{\circ}\text{C}$ [59][60].

Therefore, the retroreflector array holder is designed to accommodate both the eight retroreflectors, as defined by the most suitable array configuration, and the four bolometers, one on each side. The holder design was created in Fusion 360 [61], incorporating the dimensions of the retroreflectors from Edmund Optics [40] and the bolometers from Melexis [59].

As shown in Figure 6.7, which provides a sketch of the retroreflector array holder with dimensions in mm, the integration of all required elements was successfully achieved, maintaining the array on a single level and within the constraints imposed by Delfi-Twin physical dimensions. Figure 6.8 displays a 3D render of the retroreflector holder design.

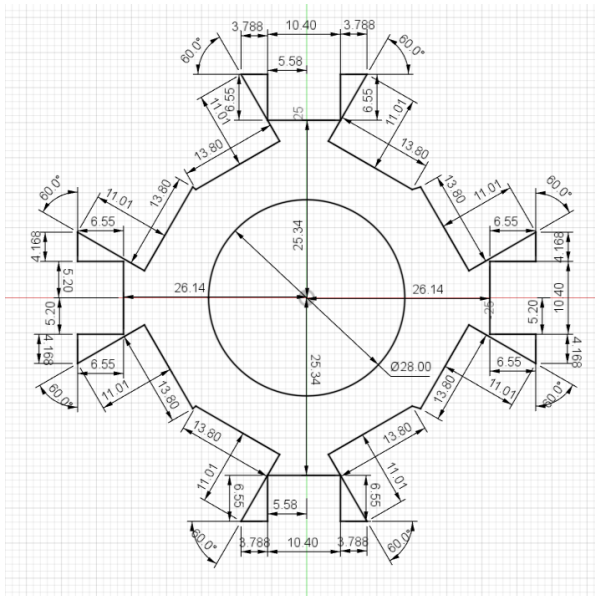


Figure 6.7: Sketch of the retroreflector holder.



Figure 6.8: Render of the retroreflector holder.

As can be observed, the retroreflector holder is not fully symmetric along all axes. One side is compressed relative to the other, and two bolometers are offset from the center. These adjustments were necessary to limit the array protrusion from the satellite body, as constrained by [REQ-SYS-1.1.2](#) and [REQ-SYS-1.1.3](#). As shown in Figure 6.9, the array protrudes 6.99 mm from the satellite panels, staying within the 7 mm limit imposed by the launch case requirements. Additionally, the array protrusion relative to the sliding plane, where the rails are positioned, is 3.64 mm on the Y-axis and 7.68 mm on the X-axis, both within the respective constraints of 3.4 mm and 3 mm set by the launch case.

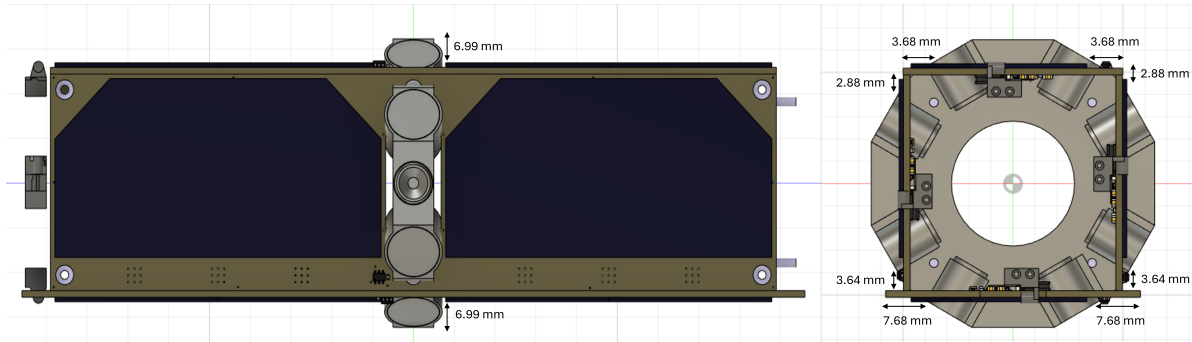


Figure 6.9: Integration of the retroreflector holder with protrusion allowances.

It is important to acknowledge that, to accommodate the required elements in the array while ensuring proper allowances from the satellite body, the angle between the retroreflectors increased to 30° relative to Nadir, compared to the 15° considered in the **8 faces** configuration analyzed in chapter 4. This adjustment led to a new array configuration, denoted as the **8 faces mod** configuration. To evaluate the performance decrease of this configuration relative to the original, the PoV simulation was rerun using Delfi-Twin attitude (attitude 3) for an AOI range between 0° and 42° and between 10° and 40°.

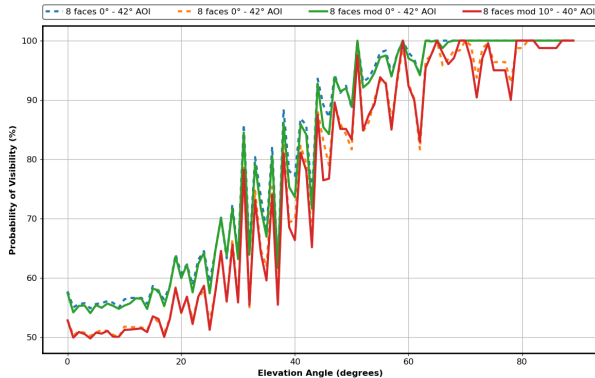


Figure 6.10: PoV curve per elevation angle for attitude 3 with the modified 8 retroreflector array configuration

Table 6.2: PoV values comparison for attitude 3 with the modified 8 retroreflector array configuration

Configuration	AOI range	Probability of Visibility	
		Avg	Std
8 faces	0° - 42°	81.55%	1.12%
8 faces	10° - 40°	76.88%	1.16%
8 faces mod	0° - 42°	80.97%	1.26%
8 faces mod	10° - 40°	76.35%	1.22%

The results of the PoV simulation using the **8 faces mod** configuration are shown in Figure 6.10, alongside the results obtained with the **8 faces** configuration. Additionally, the average PoV and standard deviation for both configurations are displayed in Table 6.2. A decrease in average PoV of 0.58% and an increase in standard deviation of 0.14% were observed for the **8 faces mod** configuration within an AOI range of 0° to 42°. For an AOI range of 10° to 40°, the data shows a reduction in average PoV of 0.53% and an increase in standard deviation of 0.06%. This trend was expected due to a wider spacing between retroreflectors on one side. Nevertheless, the observed reductions in PoV and the slight increase in standard deviation are not significant, deeming the new configuration acceptable for SLR measurements with the Matera and Potsdam stations.

The preliminary design of the holder did not consider some aspects of integration. These considerations were collected and are listed below:

- The design was performed without considering weight constraints,
- A material selection was not conducted,
- The design did not include methods for attaching the retroreflectors and bolometers to the holder structure, no holding plates were designed.
- The holes for the cabling connections of the bolometers were not included,
- The holes required for the satellite structural rods were not included,
- The edges of the holder structure were not optimized to match the edges of the satellite,
- The holder was integrated into the Delfi-PQ CAD model, which shares the same body dimensions as Delfi-Twin. However, the subsystem architecture within the satellite may change. These changes were not considered, as they are still under development,
- The thermal stresses that the retroreflectors and bolometers will need to withstand were not calculated, so the margins added to the diameters of the holder holes should be reconsidered,
- On the sliding plane, the rails extend farther than the perpendicular panels of the satellite, potentially blocking a portion of the FoV of the retroreflectors closest to the sliding plane. The blocked portion was not calculated. However, the rails could be cut at the locations of the retroreflectors to avoid FoV obstruction.

To address these considerations, an optimization of the retroreflector holder design will need to be conducted before integration. Nevertheless, this preliminary design confirms that the selected array configuration fits within Delfi-Twin physical constraints and the protrusion limits imposed by the launch case.

7

Conclusion

The aim of this thesis was to document the research conducted to design an effective and optimized retroreflector array for the new TU Delft platforms, enabling SLR measurements both with ILRS stations and the Delft laser communication terminal. The design outcomes and simulation results are presented in this conclusion.

In the PoV simulation, five array configurations were considered: the 1 face, Astrocast, 4 faces, 8 faces, and 8 faces alt configurations. These configurations were developed based on constraints defined by REQ-SYS-1.1.1, REQ-SYS-1.1.2, REQ-SYS-1.1.3, and REQ-SYS-1.2.1, where the maximum number of retroreflectors is limited to eight, and the protrusion allowances are restricted by the launch case, limiting the inclination at which the retroreflectors can be installed relative to the satellite faces. Each configuration was tested under three different satellite attitudes: fixed attitude with the bottom face consistently facing nadir, fixed attitude in the pitching and yawing axes with a rolling rate between 5 deg/s and 10 deg/s, and an attitude with a rolling rate between 5 deg/s and 10 deg/s coupled with a pitching and yawing oscillation of $\pm 20^\circ$ at a 5 deg/s rate.

For each attitude, the best array configuration was selected based on the highest achievable coverage across all elevation angles. For attitude 1, where the satellite bottom face consistently points nadir, the Astrocast configuration was selected as the most suitable, providing an average PoV of 84.97% across all elevation angles and achieving 100% coverage at angles greater than 35° . As this attitude represents the Da Vinci satellite, the research recommends implementing the Astrocast configuration to aid in the calibration of its GNSS receiver. For attitude 2, where the satellite rolls at a rate between 5 deg/s and 10 deg/s, the 8 faces alt configuration provided the most coverage, with an average PoV of 84.69%, achieving 100% coverage at elevation angles higher than 68° . Lastly, for attitude 3, which involves rolling at a rate between 5 deg/s and 10 deg/s with pitching and yawing oscillations of $\pm 20^\circ$ at a 5 deg/s rate, the 8 faces configuration was deemed the most suitable, offering an average PoV of 81.55% and achieving 100% coverage at elevation angles greater than 65° . Since this attitude corresponds to Delfi-Twin, this research recommends the implementation of the 8 faces configuration to successfully achieve SLR measurements for this platform.

The link budget analysis was conducted for the four selected ground stations: Delft laser communication station, Mini-SLR, Potsdam, and Matera. However, the link budget could not be closed for the Delft laser communication station or the Mini-SLR station, making SLR measurements unfeasible with these stations and the new TU Delft platforms. Nevertheless, a retroreflector radius of 12.7 mm was selected for the array, as it provided convergence for both the Matera and Potsdam stations and falls within the available sizes of fused silica CCR offered by Edmund Optics. For the Matera station, the link budget is closed from an elevation angle of 20° onwards, considering AOI on the array between 0° and 42° during both daytime and nighttime, fully utilizing the coverage of the selected configurations. For the Potsdam station, however, the selected retroreflector radius only closes the link budget at nighttime, from an elevation angle of 40° onwards, with an AOI range between 10° and 40° . This limits the array configuration coverage to an average PoV of 76% for Delfi-Twin, which is still deemed acceptable for

SLR measurements.

An additional analysis was conducted on the Delft laser communication station to determine the power required to achieve SLR with the new TU Delft platforms. The analysis concluded that a laser pulse power of 25 kW would be necessary to fully exploit the array coverage, while limiting the system to the same settings as Potsdam would require a laser pulse power of 2.4 kW. This highlights that the current communication lasers are not powerful enough to function as SLR devices. Furthermore, a sensitivity analysis on the retroreflector reflectivity within the link budget analysis concluded that the retroreflectors integrated into the new TU Delft platforms should exhibit a reflectivity of at least 68.4% at the ground stations' operating wavelengths of 532 nm, 1064 nm, and 1560 nm.

During the development of the thesis, 30 retroreflectors of the selected diameter were acquired by the DSE from Edmund Optics. This acquisition enabled an inspection, which was conducted in the clean room facility at the Aerospace Faculty. Four out of the 30 retroreflectors, specifically RT-08, RT-18, RT-21, and RT-25, were cataloged as damaged. To finalize the assessment and determine if the retroreflectors that passed the inspection are suitable for integration into the satellite arrays, additional tests on their optical performance must be conducted. These tests will evaluate the reflectivity and AOI leakage of the retroreflectors. If these parameters fall within the constraints assumed in this research, the retroreflector arrays can be integrated into the new platforms. Furthermore, a preliminary design of the retroreflector array holder for Delfi-Twin was developed, incorporating four bolometers from Melexis into the array. This led to the creation of a new array configuration that differs from the original 8 faces configuration, with the angle of the retroreflectors relative to nadir increased to 30°. This change did not significantly affect the performance of the array. The retroreflector holder design confirmed that the array fits within Delfi-Twin physical constraints as imposed by the launch case.

With the collected results, the research objective of designing an effective and optimized retroreflector array for the new TU Delft platforms was successfully achieved. Furthermore, the research questions were addressed, concluding that SLR is unfeasible between the Delft laser communication station and the new TU Delft platforms. Table 7.1 presents a compliance matrix where each requirement is listed along with its compliance status and corresponding explanation, while Table 7.2 addresses the compliance of the research questions.

Table 7.1: Compliance matrix for requirements.

ID	Requirement	Status	Explanation
REQ-SYS-1	The retroreflector array shall fit on the new TU Delft platforms	✓ / ?	The array fits on Delfi-Twin as discussed in section 6.3. However, an integration analysis was not performed for the Da Vinci satellite.
REQ-SYS-1.1	The retroreflector array shall fit on Delfi-Twin	✓	The array fits on Delfi-Twin as discussed in section 6.3.
REQ-SYS-1.1.1	The retroreflector array shall consist of a maximum of 8 retroreflectors	✓	Check implemented configurations in subsection 4.1.1.
REQ-SYS-1.1.2	Components and parts may be installed on the +X, -X, +Y, +Z, -Z surfaces of the baseline PocketQube configuration, provided that they do not protrude more than 7 mm from the main body baseline envelope, and are separated more than 3.4 mm from the +Y surface of the sliding plate	✓	The protrusions of the array were kept within the constraints as shown by Figure 6.9.

REQ-SYS-1.1.3	Components and parts may be installed on the -Y surface of the baseline PocketQube configuration, provided that they do not protrude more than 7 mm from the baseline envelope, and are separated more than 3 mm from the +X, -X, +Z, -Z edges of the sliding plate	✓	The protrusions of the array were kept within the constraints as shown by Figure 6.9.
REQ-SYS-1.1.4	The retroreflector array shall accommodate a satellite rolling rate not higher than 10 deg/s	✓	Check implemented attitudes in subsection 4.1.2.
REQ-SYS-1.1.5	The retroreflector array shall accommodate a satellite rolling rate not lower than 5 deg/s	✓	Check implemented attitudes in subsection 4.1.2.
REQ-SYS-1.1.6	The retroreflector array shall accommodate a satellite yawing oscillation of $\pm 20^\circ$	✓	Check implemented attitudes in subsection 4.1.2.
REQ-SYS-1.1.7	The retroreflector array shall accommodate a satellite pitching oscillation of $\pm 20^\circ$	✓	Check implemented attitudes in subsection 4.1.2.
REQ-SYS-1.2	The retroreflector array shall fit on the Da Vinci satellite	?	The integration analysis for the Da Vinci satellite was not performed.
REQ-SYS-1.2.1	Rails shall have a minimum width of 8.5 mm measured from the edge of the rail to the first protrusion on each face	?	The integration analysis for the Da Vinci satellite was not performed.
REQ-SYS-2	The retroreflector array shall achieve an AOI on the retroreflectors lower than 42	✓	Check definition of visibility in subsection 3.2.1.
REQ-SYS-3	The probability of false alarm of the ranging detector shall be lower than 2%	✓	Check calculations of background noise rate in section 5.3.
REQ-SYS-4	The probability of detection of the ranging detector shall be higher than 99%	✓	Check calculations of background noise rate in section 5.3.
REQ-SYS-5	The accuracy of the distance measurements obtained with ranging shall be better than kilometer-level	✓	Check assumed laser pulse length for the Delft laser communication station in section 5.1.

Table 7.2: Compliance matrix for research questions.

ID	Research question	Status	Explanation
RQ-1	Is it technically feasible to obtain SLR measurements using a retroreflector array mounted on the new TU Delft platforms and a laser ranging terminal from the ILRS network?	✓	Yes, check link budget analysis in section 5.4.

RQ-2	Is it technically feasible to obtain SLR measurements using a retroreflector array mounted on the new TU Delft platforms and the laser communication terminal at Delft university?	✓	No, check link budget analysis in section 5.4.
RSQ-1	What is the optimal shape and design of the retroreflector array to maximize coverage while facilitating integration with the new TU Delft platforms?	✓	Check most suitable configurations in section 4.3.
RSQ-2	What is the optimal retroreflector radius, and thus the required OCS, to effectively facilitate SLR operations for both the laser communication terminal and the ILRS terminal?	✓	Check radius range convergence in subsection 5.4.6.
RSQ-3	What are the requirements for the laser communication terminal at Delft University of Technology to establish reliable SLR measurements?	✓	Check discussion in section 5.6.
RSQ-4	How do the AOI of laser beams and environmental radiation affect the strength and reliability of the reflected signals in SLR operations?	✓	Check collected literature in section 2.3 and subsection 2.3.6.

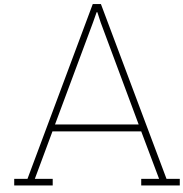
Several recommendations for future work have been identified. Firstly, for the Da Vinci satellite, the retroreflector array was selected from configurations initially designed for Delfi-Twin. This opens the possibility of rerunning the PoV simulation, placing retroreflectors on the front and back faces of the satellite to further enhance coverage. Secondly, the planned tests on the acquired retroreflectors must be completed to ensure they meet the necessary qualifications for integration into the satellite. In terms of simulation, the interference between multiple retroreflectors within the array was not considered in this study. As a result, conducting a FFDP characterization of the array to be integrated on the satellite would be valuable for understanding potential interactions and optimizing performance. Lastly, acquiring a more powerful laser could enable the Delft laser communication station to support SLR measurements independently, eliminating the need to rely on the ILRS network for satellite ranging operations.

References

- [1] ESA. *Ariane 6: post-launch update*. July 2024. URL: https://www.esa.int/Enabling_Support/Space_Transportation/Ariane/Ariane_6_post-launch_update.
- [2] ESA. *Ariane 6 joint update report, 16 September 2024*. Sept. 2024. URL: https://www.esa.int/Enabling_Support/Space_Transportation/Ariane/Ariane_6_joint_update_report_16_September_2024.
- [3] John Degnan. "Satellite Laser Ranging: Current Status and Future Prospects". In: *IEEE Transactions on Geoscience and Remote Sensing* GE-23.4 (July 1985), pp. 398–413. ISSN: 0196-2892. DOI: 10.1109/TGRS.1985.289430.
- [4] M. Pearlman et al. "Laser geodetic satellites: a high-accuracy scientific tool". In: *Journal of Geodesy* 93.11 (Nov. 2019), pp. 2181–2194. ISSN: 0949-7714. DOI: 10.1007/s00190-019-01228-y.
- [5] Michael R. Pearlman et al. "The ILRS: approaching 20 years and planning for the future". In: *Journal of Geodesy* 93.11 (Nov. 2019), pp. 2161–2180. ISSN: 0949-7714. DOI: 10.1007/s00190-019-01241-1.
- [6] P. L. Bender et al. "The Lunar Laser Ranging Experiment". In: *Science* 182.4109 (Oct. 1973), pp. 229–238. ISSN: 0036-8075. DOI: 10.1126/science.182.4109.229.
- [7] Dominic Dirkx et al. "Laser and radio tracking for planetary science missions—a comparison". In: *Journal of Geodesy* 93.11 (Nov. 2019), pp. 2405–2420. ISSN: 0949-7714. DOI: 10.1007/s00190-018-1171-x.
- [8] Michael E. Hough. "Precise orbit determination using satellite radar ranging". In: *Journal of Guidance, Control, and Dynamics* 35.4 (2012), pp. 1048–1058. ISSN: 15333884. DOI: 10.2514/1.56873.
- [9] NASA Crustal Dynamics Data Information System (CDDIS). *SLRF2020 product*. DOI: 10.5067/SLR/slrf2020_001. URL: https://cddis.nasa.gov/Data_and_Derived_Products/SLR/slrf_2020.html.
- [10] Nasa. *SATELLITE LASER RANGING AND EARTH SCIENCE NASA SPACE GEODESY PROGRAM*. Tech. rep.
- [11] E. Cordelli, A. Vananti, and T. Schildknecht. "Analysis of laser ranges and angular measurements data fusion for space debris orbit determination". In: *Advances in Space Research* 65.1 (2020), pp. 419–434. DOI: 10.1016/j.asr.2019.11.009.
- [12] Michael Lösler et al. "ILRS Reference Point Determination Using Close Range Photogrammetry". In: *Applied Sciences* 11.6 (Mar. 2021), p. 2785. ISSN: 2076-3417. DOI: 10.3390/app11062785.
- [13] Daniel Hampf et al. "The miniSLR: A low-budget, high-performance satellite laser ranging ground station". In: (June 2023). DOI: 10.1007/s00190-023-01814-1.
- [14] Thorlabs. *Specular Retroreflector Prisms*. URL: https://www.thorlabs.com/newgrouppage9.cfm?objectgroup_id=13580.
- [15] S. Dell'Agnello et al. "INRRI-EDM/2016: the first laser retroreflector on the surface of Mars". In: *Advances in Space Research* 59.2 (Jan. 2017), pp. 645–655. ISSN: 02731177. DOI: 10.1016/j.asr.2016.10.011.
- [16] D. Dequal et al. "100 kHz satellite laser ranging demonstration at Matera Laser Ranging Observatory". In: *Journal of Geodesy* 95.2 (2021). DOI: 10.1007/s00190-020-01469-2.
- [17] Ludwig Combrinck. "Satellite Laser Ranging". In: *Sciences of Geodesy - I*. Berlin, Heidelberg: Springer Berlin Heidelberg, 2010, pp. 301–338. DOI: 10.1007/978-3-642-11741-1_9. URL: http://link.springer.com/10.1007/978-3-642-11741-1_9.

- [18] John W. Marini. "Correction of Satellite Tracking Data for an Arbitrary Tropospheric Profile". In: *Radio Science* 7.2 (Feb. 1972), pp. 223–231. ISSN: 0048-6604. DOI: 10.1029/RS007i002p00223.
- [19] V. B. Mendes et al. "Improved mapping functions for atmospheric refraction correction in SLR". In: *Geophysical Research Letters* 29.10 (May 2002), pp. 53–1. ISSN: 1944-8007. DOI: 10.1029/2001GL014394.
- [20] V. B. Mendes and E. C. Pavlis. "High-accuracy zenith delay prediction at optical wavelengths". In: *Geophysical Research Letters* 31.14 (July 2004). ISSN: 0094-8276. DOI: 10.1029/2004GL020308.
- [21] Mateusz Drożdżewski and Krzysztof Sośnica. "Troposphere delay modeling in SLR based on PMF, VMF3o, and meteorological data". In: *Progress in Earth and Planetary Science* 11.1 (Dec. 2024). ISSN: 21974284. DOI: 10.1186/s40645-024-00613-2.
- [22] Toshimichi Otsubo and Graham M. Appleby. "System-dependent center-of-mass correction for spherical geodetic satellites". In: *Journal of Geophysical Research: Solid Earth* 108.B4 (Apr. 2003). ISSN: 0148-0227. DOI: 10.1029/2002JB002209.
- [23] José C. Rodríguez. *Satellite Orientation effects on Centre of Mass Corrections*. Nov. 2022. URL: <https://youtu.be/TAK0JoTssoo?si=b922A1jluKnPShj1>.
- [24] Dennis D. McCarthy et al. *IERS Conventions (2003)*. ISBN: 3898888843.
- [25] ILRS. *ILRS Normal Point Algorithm*. 2012. URL: https://ilrs.gsfc.nasa.gov/data_and_products/data/npt/npt_algorithm.html.
- [26] ILRS. *First One-day Introductory and Refresher Course on Satellite and Lunar Laser Ranging*. Stuttgart, Oct. 2019. URL: https://ilrs.gsfc.nasa.gov/2019_Technical_Workshop/SLR_School/index.html.
- [27] John J. Degnan. "An Introduction to Satellite Laser Ranging Technology and its Applications". In: Stuttgart, Oct. 2019.
- [28] John J. Degnan. "Millimeter accuracy satellite laser ranging: A review". In: 1993, pp. 133–162. DOI: 10.1029/GD025p0133.
- [29] Hall et al. "Cirrus Cloud Model, Atmospheric Transmittance-Radiance". In: *Air Force Geophysics Laboratory* (1983), pp. 58–67.
- [30] Columbia University Press. *Chapter 2. SOLAR RADIATION 2.1 Solar radiation*. Tech. rep. 1994. URL: https://ocw.tudelft.nl/wp-content/uploads/Solar-Cells-R2-CH2_Solar_radiation.pdf.
- [31] ASTM International. *Standard Tables for Reference Solar Spectral Irradiances: Direct Normal and Hemispherical on 37° Tilted Surface 1*. Tech. rep. DOI: 10.1520/G0173-03R20.
- [32] Avionics Department. *Electronic Warfare and Radar Systems Engineering Handbook 2013 NAWCWD TP 8347 Fourth Edition*. Tech. rep. Point Mugu, California: Naval Air Warfare Center Weapons Division.
- [33] De Donkerte van de Waddengebied. *Was it dark?* URL: <https://washetdonker.nl/>.
- [34] F. Falchi et al. "Light pollution in USA and Europe: The good, the bad and the ugly". In: *Journal of Environmental Management* 248 (Oct. 2019). ISSN: 10958630. DOI: 10.1016/j.jenvman.2019.06.128.
- [35] Unihedron. *Sky Quality Meter*. URL: <http://www.unihedron.com/projects/darksky/magconv.php?ACTION=SOLVE&txtMAGSQA=18>.
- [36] *UnitConverters*. URL: <https://www.unitconverters.net/luminance/candela-square-meter-to-watt-sq-cm-steradian-at-555-nm.htm>.
- [37] John J. Degnan. "A Tutorial on Retroreflectors and Arrays for SLR". In: Frascati, Italy, Nov. 2012.
- [38] Tristan Meyer. "Analysis of the performance parameters of Satellite Laser Ranging (SLR) systems based on the link budget under exemplary inclusion of the miniSLR system". PhD thesis. Stuttgart: University of Stuttgart, 2022.

- [39] Philip C L Stephenson. *Satellite Laser Ranging Photon-Budget Calculations for a Single Satellite Cornercube Retroreflector: Attitude Control Tolerance*. Tech. rep. National Security and ISR Division, Oct. 2015.
- [40] Edmund Optics. *Aluminum Coated, Fused Silica Corner Cube*. URL: <https://www.edmundoptics.com/p/127mm-aluminum-coated-fused-silica-corner-cube/9367/>.
- [41] T.L. Griffiths et al. "A study of the effects of gamma radiation on optical components used in specially constructed hot cell laser-induced breakdown spectroscopy (LIBS) instruments". In: *Spectrochimica Acta Part B: Atomic Spectroscopy* 180 (June 2021), p. 106205. ISSN: 05848547. DOI: 10.1016/j.sab.2021.106205.
- [42] Royal Belgian Institute for Space Aeronomy. *SPENVIS*. URL: <https://spenvis.oma.be/>.
- [43] ILRS. *Potsdam: Site Log*. URL: https://ilrs.gsfc.nasa.gov/network/stations/active/POT3_sitelog.html.
- [44] ILRS. *Matera: Site Log*. URL: https://ilrs.gsfc.nasa.gov/network/stations/active/MATM_station_info.html?log#top.
- [45] Hemani Kaushal, V.K. Jain, and Subrat Kar. *Free Space Optical Communication*. New Delhi: Springer India, 2017. ISBN: 978-81-322-3689-4. DOI: 10.1007/978-81-322-3691-7.
- [46] ESA. *FLY YOUR SATELLITE! DESIGN SPECIFICATION FOR POCKETQUBES*. Tech. rep. 2023.
- [47] ESA. *ENGINEERING GUIDELINES FOR ESA IOD CUBESAT PROJECTS*. Tech. rep. Feb. 2024.
- [48] M. Petrassi. *Satellite/lunar/GNSS laser ranging Characterization Facilities Laboratory*. URL: <https://www.lnf.infn.it/esperimenti/etrusco/index.html>.
- [49] Astrocass. *ILRS SLR MISSION SUPPORT REQUEST FORM*. Tech. rep. URL: http://ilrs.gsfc.nasa.gov/missions/satellite_missions/current_missions/index.html.
- [50] Deutsches Geodätisches Forschungsinstitut and Technische Universität München. *EUROLAS Data Center (EDC)*. URL: <https://edc.dgfi.tum.de/en/>.
- [51] Brandon Rhodes. *Skyfield: High precision research-grade positions for planets and Earth satellites generator*. July 2019.
- [52] Paul Cefola, David A Vallado, and Paul J Cefola. *Two-line element sets-Practice and use*. Tech. rep. 2012. URL: <https://www.researchgate.net/publication/289774073>.
- [53] Ankit Rohatgi. *WebPlotDigitizer*. URL: <https://apps.automeris.io/wpd4/>.
- [54] ILRS. *Graz: Site Log*. URL: https://ilrs.gsfc.nasa.gov/network/stations/active/GRZL_sitelog.html.
- [55] Philip Gibbs and Roger Wood. *The C-SPAD as a single-photon detector*. Tech. rep.
- [56] Lukas Müller et al. "Real-time navigation solutions of low-cost off-the-shelf GNSS receivers on board the Astrocass constellation satellites". In: *Advances in Space Research* 73.1 (Jan. 2024), pp. 2–19. ISSN: 02731177. DOI: 10.1016/j.asr.2023.10.001.
- [57] Luca Porcelli et al. *Optical-Performance Testing of the Laser RetroReflector for InSight*. Jan. 2019. DOI: 10.1007/s11214-018-0569-3.
- [58] Dell' Agnello et al. *ETRUSCO-2: AN ASI-INFN PROJECT OF TECHNOLOGICAL DEVELOPMENT AND "SCF-TEST" OF GNSS LASER RETROREFLECTOR ARRAYS*. Tech. rep. Sept. 2011.
- [59] Melexis. *Far infrared thermal sensor array*. URL: <https://www.melexis.com/en/product/MLX90640/Far-Infrared-Thermal-Sensor-Array>.
- [60] Melexis. *MLX90640 32x24 IR array*. Tech. rep.
- [61] Autodesk. *Fusion 360*. URL: www.autodesk.com/products/fusion-360.



PoV Graphs

In this appendix, the resulting graphs from the PoV simulation are presented for each configuration. The first set of graphs shows an orbital pass over the station, illustrating how each attitude is simulated per configuration. The second set of graphs displays the regions where the satellite is visible and where it is not, based on the definition of visibility discussed in subsection 3.2.1. The final set of graphs shows the average PoV per elevation angle, including the maximum and minimum variations for all tested attitudes.

A.1. Configuration 1

In this section, the supporting graphs obtained from the PoV simulation for the **1 face** configuration are presented. Figure A.1, Figure A.2, and Figure A.3 depict the simulated satellite attitude over the station. Figure A.4, Figure A.5, and Figure A.6 display the visibility maps for 0 rolling rate, a rolling rate of 5 deg/s, and a rolling rate of 5 deg/s combined with an oscillation in both pitch and yaw of $\pm 20^\circ$ at a 5 deg/s rate. Finally, Figure A.7, Figure A.8, and Figure A.9 show the average PoV per elevation angle for configuration 1, with each graph corresponding to one of the three considered attitudes.

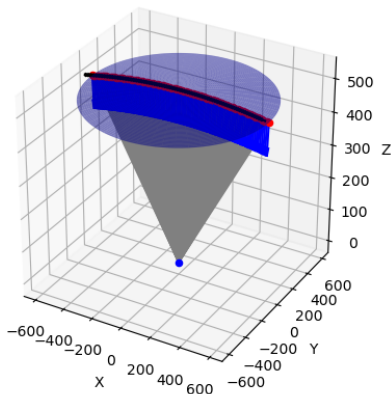


Figure A.1: Zenith pass of configuration 1 with attitude 1.

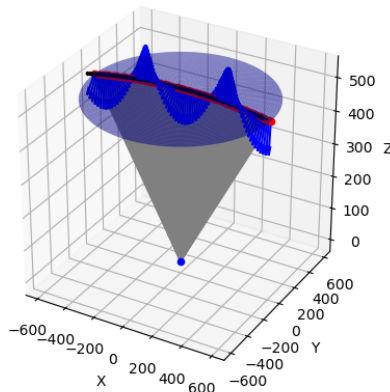


Figure A.2: Zenith pass of configuration 1 with attitude 2.

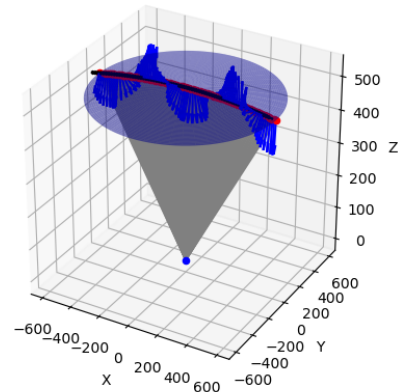


Figure A.3: Zenith pass of configuration 1 with attitude 3.

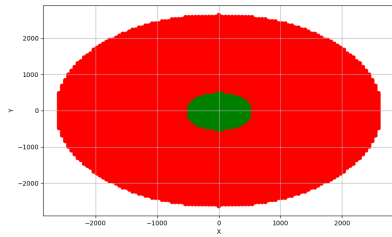


Figure A.4: Visibility map of configuration 1 with attitude 1.

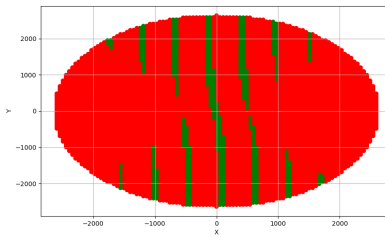


Figure A.5: Visibility map of configuration 1 with attitude 2.

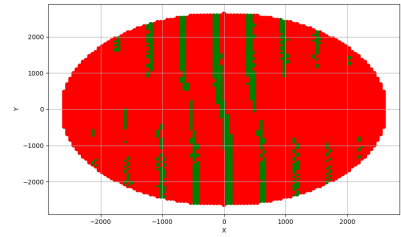


Figure A.6: Visibility map of configuration 1 with attitude 3.

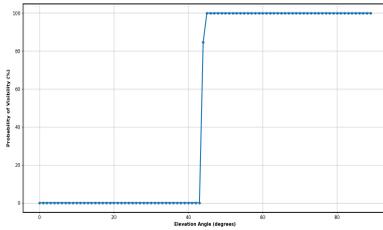


Figure A.7: Average PoV per elevation angle of configuration 1 with attitude 1.

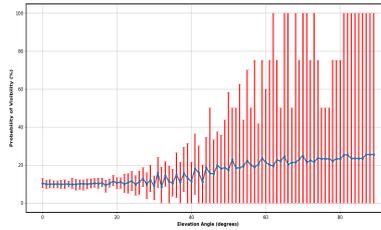


Figure A.8: Average PoV per elevation angle of configuration 1 with attitude 2.

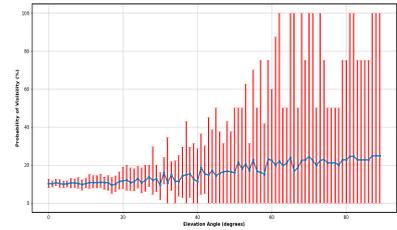


Figure A.9: Average PoV per elevation angle of configuration 1 with attitude 3.

A.2. Configuration 2

In this section, the supporting graphs obtained from the PoV simulation for the **Astrocast** configuration are presented. Figure A.10, Figure A.11, and Figure A.12 depict the simulated satellite attitude over the station. Figure A.13, Figure A.14, and Figure A.15 display the visibility maps for 0 rolling rate, a rolling rate of 5 deg/s, and a rolling rate of 5 deg/s combined with an oscillation in both pitch and yaw of $\pm 20^\circ$ at a 5 deg/s rate. Finally, Figure A.16, Figure A.17, and Figure A.18 show the average PoV per elevation angle for configuration 2, with each graph corresponding to one of the three considered attitudes.

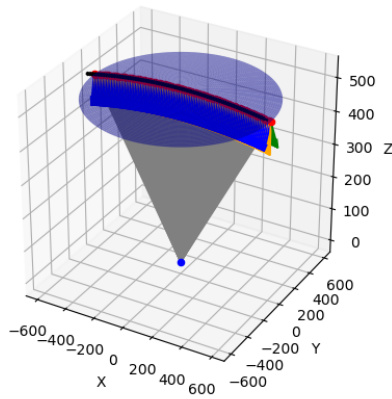


Figure A.10: Zenith pass of configuration 2 with attitude 1.

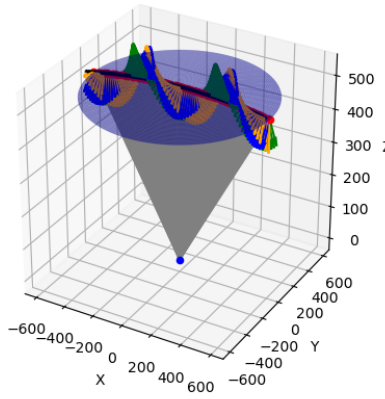


Figure A.11: Zenith pass of configuration 2 with attitude 2.

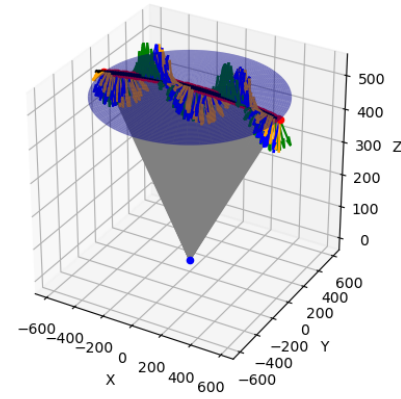


Figure A.12: Zenith pass of configuration 2 with attitude 3.

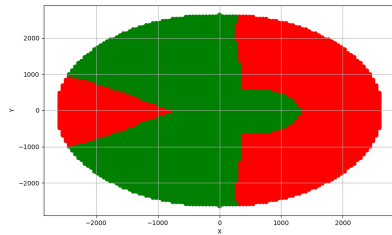


Figure A.13: Visibility map of configuration 2 with attitude 1.

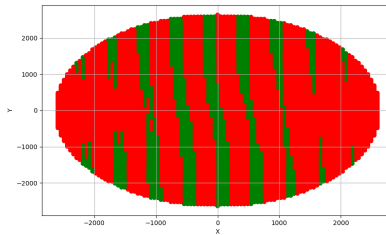


Figure A.14: Visibility map of configuration 2 with attitude 2.

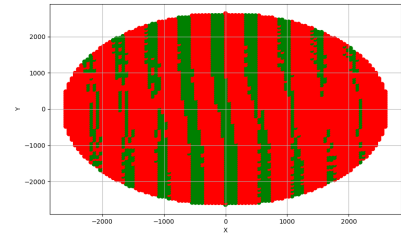


Figure A.15: Visibility map of configuration 2 with attitude 3.

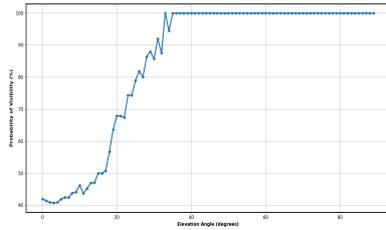


Figure A.16: Average PoV per elevation angle of configuration 2 with attitude 1.

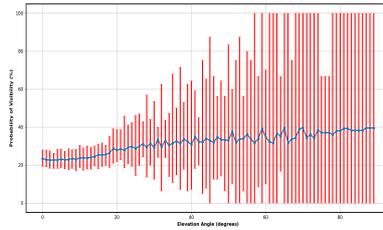


Figure A.17: Average PoV per elevation angle of configuration 2 with attitude 2.

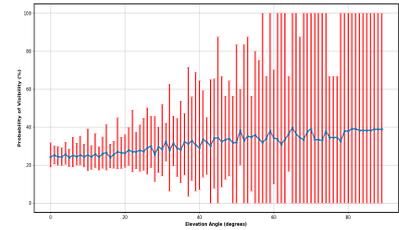


Figure A.18: Average PoV per elevation angle of configuration 2 with attitude 3.

A.3. Configuration 3

In this section, the supporting graphs obtained from the PoV simulation for the **4 faces** configuration are presented. Figure A.19, Figure A.20, and Figure A.21 depict the simulated satellite attitude over the station. Figure A.22, Figure A.23, and Figure A.24 display the visibility maps for 0 rolling rate, a rolling rate of 5 deg/s, and a rolling rate of 5 deg/s combined with an oscillation in both pitch and yaw of $\pm 20^\circ$ at a 5 deg/s rate. Finally, Figure A.25, Figure A.26, and Figure A.27 show the average PoV per elevation angle for configuration 3, with each graph corresponding to one of the three considered attitudes.

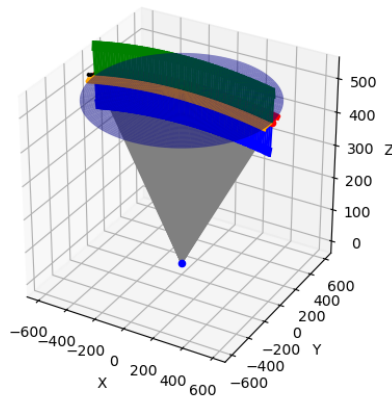


Figure A.19: Zenith pass of configuration 3 with attitude 1.

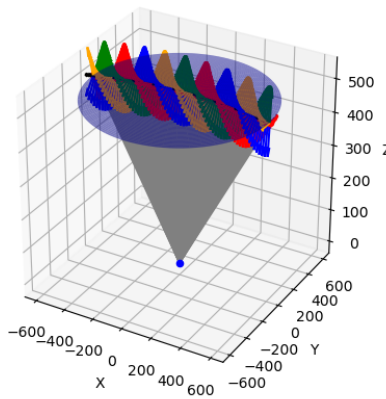


Figure A.20: Zenith pass of configuration 3 with attitude 2.

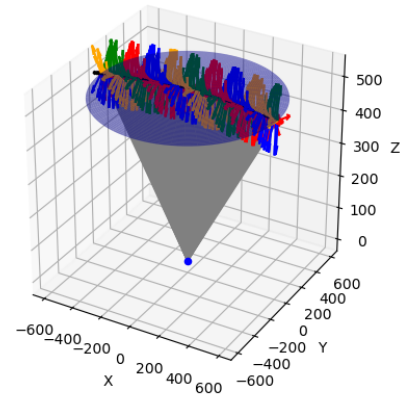


Figure A.21: Zenith pass of configuration 3 with attitude 3.

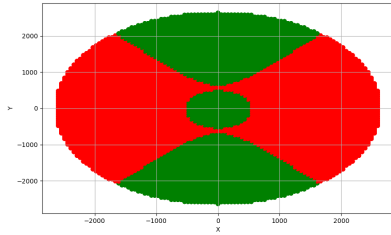


Figure A.22: Visibility map of configuration 3 with attitude 1.

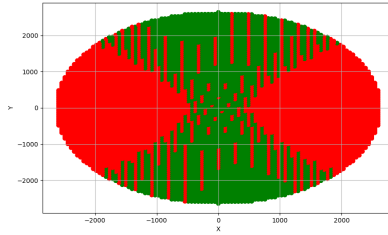


Figure A.23: Visibility map of configuration 3 with attitude 2.

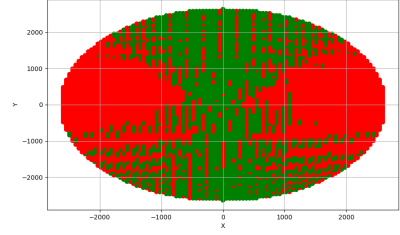


Figure A.24: Visibility map of configuration 3 with attitude 3.

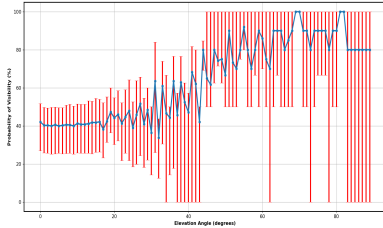


Figure A.25: Average PoV per elevation angle of configuration 3 with attitude 1.

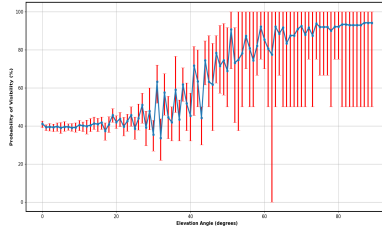


Figure A.26: Average PoV per elevation angle of configuration 3 with attitude 2.

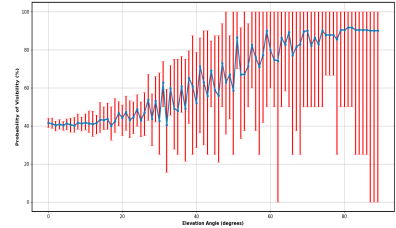


Figure A.27: Average PoV per elevation angle of configuration 3 with attitude 3.

A.4. Configuration 4

In this section, the supporting graphs obtained from the PoV simulation for the **8 faces** configuration are presented. Figure A.28, Figure A.29, and Figure A.30 depict the simulated satellite attitude over the station. Figure A.31, Figure A.32, and Figure A.33 display the visibility maps for 0 rolling rate, a rolling rate of 5 deg/s, and a rolling rate of 5 deg/s combined with an oscillation in both pitch and yaw of $\pm 20^\circ$ at a 5 deg/s rate. Finally, Figure A.34, Figure A.35, and Figure A.36 show the average PoV per elevation angle for configuration 4, with each graph corresponding to one of the three considered attitudes.

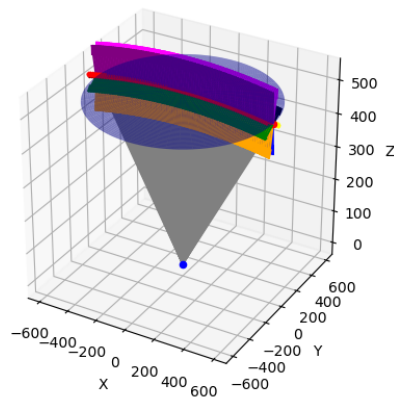


Figure A.28: Zenith pass of configuration 4 with attitude 1.

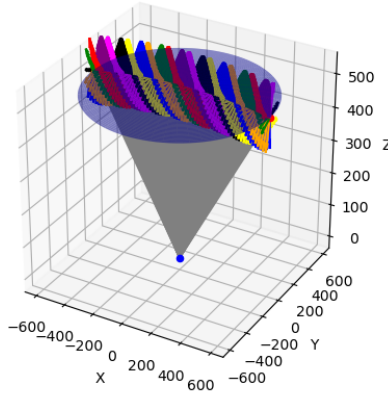


Figure A.29: Zenith pass of configuration 4 with attitude 2.

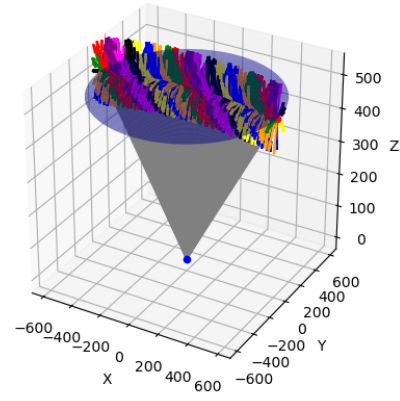


Figure A.30: Zenith pass of configuration 4 with attitude 3.

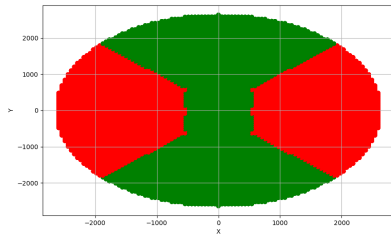


Figure A.31: Visibility map of configuration 4 with attitude 1.

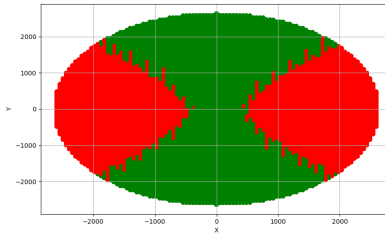


Figure A.32: Visibility map of configuration 4 with attitude 2.

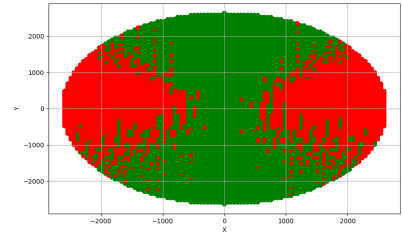


Figure A.33: Visibility map of configuration 4 with attitude 3.

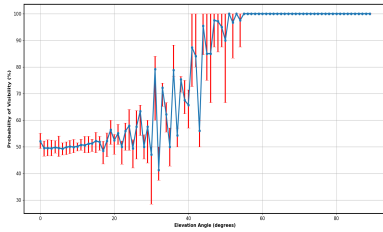


Figure A.34: Average PoV per elevation angle of configuration 4 with attitude 1.

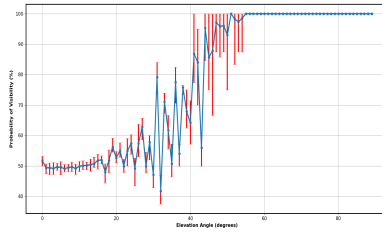


Figure A.35: Average PoV per elevation angle of configuration 4 with attitude 2.

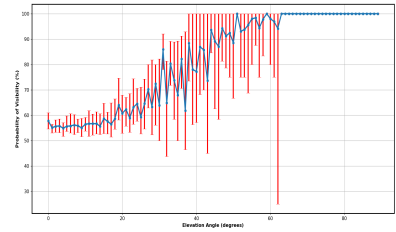


Figure A.36: Average PoV per elevation angle of configuration 4 with attitude 3.

A.5. Configuration 5

In this section, the supporting graphs obtained from the PoV simulation for the **8 faces alt** configuration are presented. Figure A.37, Figure A.38, and Figure A.39 depict the simulated satellite attitude over the station. Figure A.39, Figure A.40, and Figure A.41 display the visibility maps for 0 rolling rate, a rolling rate of 5 deg/s, and a rolling rate of 5 deg/s combined with an oscillation in both pitch and yaw of $\pm 20^\circ$ at a 5 deg/s rate. Finally, Figure A.42, Figure A.43, and Figure A.44 show the average PoV per elevation angle for configuration 5, with each graph corresponding to one of the three considered attitudes.

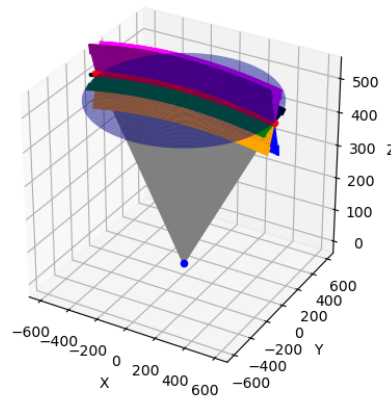


Figure A.37: Zenith pass of configuration 5 with attitude 1.

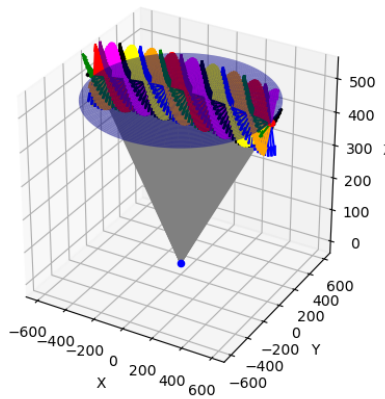


Figure A.38: Zenith pass of configuration 5 with attitude 2.

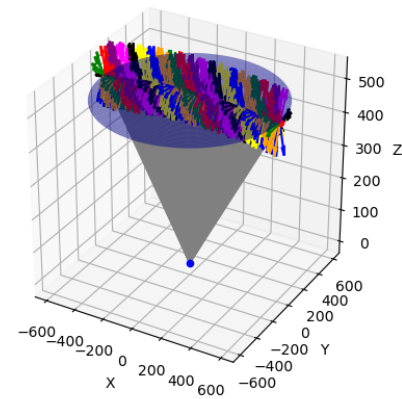


Figure A.39: Zenith pass of configuration 5 with attitude 3.

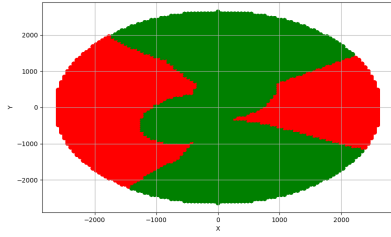


Figure A.40: Visibility map of configuration 5 with attitude 1.

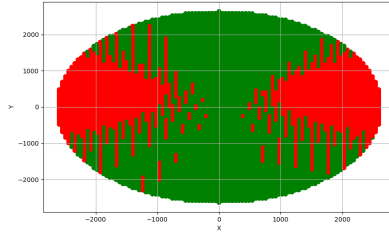


Figure A.41: Visibility map of configuration 5 with attitude 2.

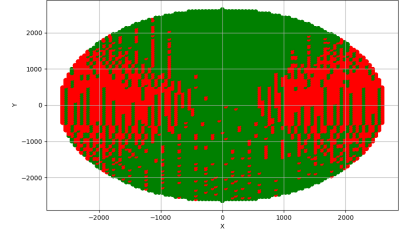


Figure A.42: Visibility map of configuration 5 with attitude 3.

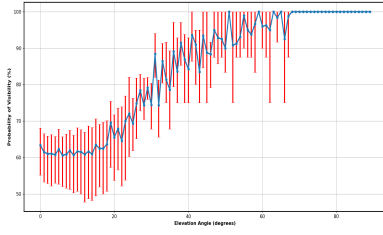


Figure A.43: Average PoV per elevation angle of configuration 5 with attitude 1.

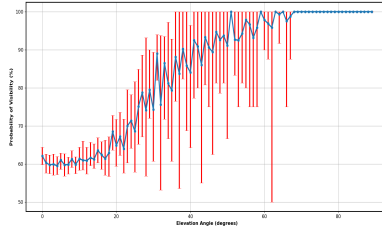


Figure A.44: Average PoV per elevation angle of configuration 5 with attitude 2.

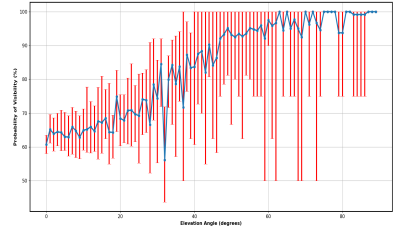


Figure A.45: Average PoV per elevation angle of configuration 5 with attitude 3.